



# Towards a Triangular Lattice Quantum Gas Microscope

(Raman-Sideband Cooling in a Triangular Optical Lattice)

vorgelegt von  
David C. Nak  
geboren am  
08. April 1996  
in Hamburg

Masterarbeit im Studiengang Physik  
Universität Hamburg  
RIKEN Center for Emergent Matter Science

2019

1. Gutachter: Herr Prof. Dr. Klaus Sengstock
2. Gutachter: Herr Dr. Takeshi Fukuhara



Hiermit bestätige ich, dass die vorliegende Arbeit von mir selbstständig verfasst wurde und ich keine anderen als die angegebenen Hilfsmittel – insbesondere keine im Quellenverzeichnis nicht benannten Internetquellen – verwendet habe und die Arbeit von mir nicht vorher in einem anderen Prüfungsverfahren eingereicht wurde. Die eingereichte schriftliche Form entspricht der auf dem elektronischen Speichermedium. Ich bin damit einverstanden, dass die Masterarbeit veröffentlicht wird.

Hamburg, den 07. Oktober 2019



## Zusammenfassung

Ultrakalte Quantengase werden in einer Vielzahl von Experimenten zur Simulation verschiedenster Modellsysteme genutzt, da sie einen vergleichsweise einfachen Messzugang bieten und sich aufgrund der einfachen und präzisen Kontrolle über die mit ihnen erstellten Systeme besonders gut dazu eignen. Insbesondere in Bezug auf die Simulation von Festkörpern sind sie bestens geeignet. Denn mit optischen Potentialen lassen sich für die Quantengase defektfreie Gitter verschiedenster Geometrien erstellen. Sie bilden eine ideale Basis zur Untersuchung von neuen Quantenphasen, wie beispielsweise Quantenspinflüssigkeiten oder Zustände frustrierter magnetischer Systeme.

Diese Arbeit berichtet von der Entwicklung eines kontinuierlichen Raman-Seitenbandkühlschemas sowie der Realisierung des dazu notwendigen experimentellen Aufbaus für den zukünftigen Einsatz in einem Quantengasmikroskop zur Bildgebung durch Fluoreszenz. Mithilfe einer Simulation, basierend auf der numerischen Berechnung der Zeitentwicklung mithilfe einer Quantenmastergleichung, konnten für das entwickelte Abbildungsverfahren eine Reduzierung des mittleren Vibrationszustands auf 0.04 bestimmt werden, wobei der Kühlprozess mit einer Zeitkonstante von 266  $\mu$ s beschrieben werden kann. Die benötigte Belichtungszeit zur einzelgitterplatzaufgelösten Abbildung beträgt 600 ms mit einem einhergehendem Teilchenverlust von 3.3 %.

Momentan kann die Raman-Seitenbandkühlung mit einer Projektion des Impulses auf das vertikale als auch das horizontale Dreiecksgitter gleichzeitig sowie auch nur auf das Dreiecksgitter betrieben werden. Noch unbeseitigte Probleme verhinderten die Anwendung im dreidimensionalen Gitter bisher. Nur im zweidimensionalen Dreiecksgitter war die Anwendung bisher erfolgreich. Spektren, welche die erwarteten Seitenbänder auflösen, konnten aufgenommen werden und der mittlere Vibrationszustand konnte verringert werden, was sich im Schmälern des entsprechenden Seitenbandsignals manifestiert. Der mittlere Vibrationszustand konnte von  $1.11 \pm 0.08$  auf  $0.28 \pm 0.02$  reduziert werden und die ermittelte Zeitkonstante beträgt 537 ms, was in der selben Größenordnung wie die der numerisch ermittelten ist.

Mit der zukünftigen Beseitigung der experimentellen Hindernisse sollte die Anwendung der Raman-Seitenbandkühlung im dreidimensionalen Gitter ermöglicht werden.



## Abstract

Ultracold quantum gas experiments are widely used in order to simulate a variety of model systems as they are easily accessible and provide a comparably easy and precise control over the system parameters. Especially for the investigation of solid states they are convenient as defect free lattices of various geometries can be constructed by using optical lattices. They may provide an ideal playground for the investigation of new quantum phases emerging in these geometries such as frustrated magnetic states or quantum spin liquids. This thesis reports about the development of a continuous Raman sideband cooling scheme as well as the realization of the required experimental setup for the future use in a quantum gas microscope setup for the purpose of fluorescence imaging. A simulation based on a numerical evaluation of a quantum master equation estimates cooling down to a mean vibrational level of 0.04 with a time constant of 266  $\mu$ s. The estimated duration necessary for single site resolved imaging amounts to 600 ms accompanied by a atom loss of 3.3 %. Currently the Raman sideband cooling can be applied with a momentum projection for both, the triangular lattice and the vertical lattice, as well as only for the triangular lattice. Unresolved experimental difficulties prohibited the application in the three dimensional lattice so far.

Only in the two dimensional triangular lattice the application was successful. Spectra resolving the expected sidebands were taken and the mean vibrational level was lowered, manifesting as a decreased signal of the corresponding sideband in the spectrum. The mean vibrational number was lowered from  $1.11 \pm 0.08$  to  $0.28 \pm 0.02$  and a time constant, in the same order as the numerically evaluated one, of 537 ms was determined.

With improvements to come, eliminating the issues that hinder the application in the three dimensional lattice, the Raman setup should become suitable for single site resolved imaging.





# Contents

<b>1</b>	<b>Introduction</b>	<b>1</b>
<b>2</b>	<b>Atom-Light Interaction</b>	<b>5</b>
2.1	The Two-Level Atom . . . . .	5
2.1.1	General Schrödinger equation . . . . .	5
2.1.2	The Rabi-Problem . . . . .	6
2.2	Multilevel Atoms . . . . .	8
2.2.1	Energy Scheme . . . . .	8
2.2.2	Dipole Coupling . . . . .	10
2.2.3	Spontaneous Decay . . . . .	12
2.3	Three-Level Transitions . . . . .	12
2.3.1	Interaction Hamiltonian . . . . .	12
2.3.2	Raman Transition . . . . .	13
2.3.3	Coherent Population Trapping . . . . .	17
2.4	Conclusion . . . . .	18
<b>3</b>	<b>Optical Lattice</b>	<b>19</b>
3.1	Triangular Lattice . . . . .	19
3.2	Band Structure and Wannier Functions . . . . .	22
3.3	Coupling between Sidebands . . . . .	25
3.4	Conclusion . . . . .	28
<b>4</b>	<b>Raman-Sideband Cooling</b>	<b>29</b>
4.1	Transition Scheme . . . . .	29
4.2	Lindblad Equation . . . . .	33
4.3	Simulated Population Evolution . . . . .	35
4.4	Experimental Setup . . . . .	38
4.4.1	Laser Setup . . . . .	38
4.4.2	Offset-Lock . . . . .	40
4.4.3	Raman Transition Experiment . . . . .	44
4.4.4	Repump lasers . . . . .	46
4.4.5	Quantum Gas Microscope Setup . . . . .	48

4.5	Sideband cooling and Rabi Frequency Measurement . . . . .	54
4.5.1	Application of continuous Raman Sideband cooling . . . . .	54
4.5.2	Unsymmetric Sidebands . . . . .	55
4.5.3	Raman Rabi Frequency Measurement . . . . .	56
4.5.4	Raman Sideband Cooling Time Constant . . . . .	59
4.6	Conclusion . . . . .	60
<b>5</b>	<b>Conclusion and Outlook</b>	<b>63</b>
<b>A</b>	<b>An Atom in an Electromagnetic Field</b>	<b>67</b>
A.1	Classical Lorentz-Force Hamiltonian . . . . .	67
A.2	The free Hydrogen Atom . . . . .	68
A.3	Center-of-Mass System . . . . .	69
A.4	Dipole Approximation . . . . .	70
A.5	Local Transformation . . . . .	71
<b>B</b>	<b><math>^{87}\text{Rb}</math> Hyperfine Energy Scheme</b>	<b>73</b>
	<b>Acknowledgments</b>	<b>75</b>
	<b>Bibliography</b>	<b>82</b>

# List of Figures

2.1	Three level time evolution demonstrating Raman transition . . . . .	15
2.2	Three level time evolution demonstrating coherent population trapping	17
3.1	Triangular lattice potential . . . . .	21
3.2	Calculated band structure for a triangular lattice . . . . .	24
3.3	Wannier functions of a triangular lattice . . . . .	25
3.4	Vibrational level coupling . . . . .	27
4.1	Simplified vibrational transition scheme for continuous Raman side- band cooling . . . . .	30
4.2	Internal transition scheme for continuous Raman sideband cooling . .	32
4.3	Transition scheme time evolution . . . . .	37
4.4	Simplified Raman laser setup scheme . . . . .	39
4.5	Offset-lock setup scheme . . . . .	41
4.6	Offset-lock spectrum and long time stability . . . . .	43
4.7	Beam alignment for Raman transition . . . . .	44
4.8	Observed Rabi oscillation by a Raman transition . . . . .	45
4.9	Raman repumper output setup . . . . .	47
4.10	Beam alignment for Raman sideband coupling . . . . .	49
4.11	Sideband spectrum in the 3D lattice using Raman 1 Vertical . . . . .	50
4.12	Sideband spectrum in the 3D lattice using Raman 1 Vertical and high Raman powers . . . . .	51
4.13	Sideband spectrum using a microwave transition . . . . .	51
4.14	Sideband spectrum using Raman 1 Vertical without the vertical lattice	52
4.15	Sideband spectrum using Raman 1 Horizontal in the 3D lattice . . . .	53
4.16	Sideband spectrum after Raman sideband cooling . . . . .	55
4.17	Example for a unsymmetric sideband . . . . .	57
4.18	Raman Rabi frequency measurement . . . . .	58
4.19	Raman Rabi frequency measurement for a carrier and a sideband transition . . . . .	59
4.20	Raman sideband cooling time constant measurement . . . . .	60
B.1	Hyperfine Energy Scheme of $^{87}\text{Rb}$ for the $D_1$ transition. . . . .	73

B.2	Hyperfine Energy Scheme of $^{87}\text{Rb}$ for the $D_2$ transition. . . . .	74
-----	---	----

# Chapter 1

## Introduction

The upcoming of quantum mechanics about 100 years ago was not only a drastic event for physics as it challenged the former understanding of nature in an unprecedented scale with concepts like wave-particle duality or quantum entanglement, but ultimately was reason for dramatic change in technology and thus society. It has been fundamental for so many things, such as computers, imaging technology or just light sources.

Elementary for this development was the study of quantum mechanical systems in order to exploit the new emerging phenomena. While in comparison simple systems such as the harmonic oscillator or the hydrogen atom can be solved analytically and without too much time effort, the situation changes for more complex systems as many-body systems. Conventional computers may mitigate this problem, but they also have their limitations.

As a possibility to confront these restrictions Richard P. Feynman proposed the utilization of quantum mechanical systems in order to simulate them [1]. A basis for such quantum simulators can be provided by Bose-Einstein condensates (BEC). They were predicted theoretically in 1924 and 1925 by S. N. Bose and A. Einstein [2, 3], but it took additional 70 years until the experimental challenges were overcome for their realization. Important steps towards BECs were the realization of the laser and the subsequent breakthroughs in laser cooling of atoms, such as the application of magneto optical traps [4] or the discovery of polarization gradient cooling [5, 6]. For the time being the only possibility to fall below the critical temperature was evaporative cooling [7, 8]. Finally in 1995 the first BECs were created [9, 10]. BECs are macroscopic quantum states. First experiments focused on probing fundamental quantum mechanics such as the observation of collective excitations [11, 12] or interference [13]. The appearance of vortices in rotating systems [14] or solitons [15] were observed as well. Soon after, the opportunities provided by BECs with respect to quantum simulation, especially relating many-body dynamics, were recognized [16–18]. One of the first examples for such simulations

was the phase transition from a superfluid to a Mott insulator [19]. Besides Bosons also Fermions were used to create a degenerate state, the degenerate Fermi gas [20], and used for many-body simulation [21, 22].

One of many directions for the quantum simulation with degenerate Bose gases is the investigation of magnetism. Frustrated classical magnetism was investigated in the group of Prof. Sengstock [23]. Not all lattice geometries allow for the investigation of such frustrated systems. The simplest one allowing it is the triangular lattice [24]. A triangular lattice is also suited for the investigation of so called quantum spin liquids [25]. These kind of systems are of interest as they might allow for a better understanding of high temperature superconductivity. But quantum spin liquids do not have any long range ordering and thereby cannot be investigated by means of conventional time-of-flight measurements. Here quantum gas microscopes are of help [26, 27]. They allow for single-site resolved imaging of an optical lattice. This way local correlations as they are expected for quantum spin liquids could be observed.

The Quantum Many-Body-Dynamics Research Unit at the RIKEN Center for Emergent Matter Science aims for the investigation of these frustrated systems. They are currently setting up a quantum gas microscope experiment using  $^{87}\text{Rb}$  in a triangular lattice. Quantum gas microscopes freeze the dynamics of the investigated system by rapidly increasing the trapping potential. With an appropriate objective single occupied lattice sites can then be imaged by fluorescence. But as fluorescence is associated with heating and thereby atom loss, the imaging scheme has to be coupled with a cooling mechanism. Methods currently used for this purpose are molasses cooling [26, 27], electromagnetically induced transparency cooling [28, 29], resolved sideband cooling [30] and Raman-sideband cooling [31, 32]. Due to the limited optical access a Raman sideband cooling system was implemented. Raman-sideband cooling builds on Raman transitions which is a well-established method to drive two photon transitions. Recently, Raman transitions were used to cool atoms into quantum degeneracy solely by means of laser cooling [33, 34].

This thesis will present the development of a Raman-sideband cooling scheme and the setup of the laser system required. It will begin with introducing optical transitions with atoms in order to explain the physical mechanism describing Raman transitions. It will continue with the coupling between vibrational states as these are necessary to lower the vibrational level. Subsequently the transition scheme will be presented as well as a numerical calculation simulating its time evolution. Finally the setup will be used for spectroscopy of the sidebands and Raman-sideband cooling. The structure of this thesis is as described in the following.

**Chapter 2** introduces optical transitions starting at the two-level atom to continue with the multilevel atom and finally arrive at three level transitions. At last

---

Raman transitions will be presented. They occur as two photon processes in three level systems.

**Chapter 3** starts with introducing the triangular lattice generated by a planar three beam interference. It proceeds with the calculation of the Bloch bands and introduces the coupling between vibrational levels. Finally, the Lamb-Dicke approximation for the coupling in a deep trap will be presented and compared to the numerical computed coupling parameter for the triangular lattice.

**Chapter 4** begins with the introduction of the planned scheme for fluorescence imaging using Raman sideband cooling. It will continue with the introduction of the Lindblad equation in order to numerically calculate the the time evolution of the fluorescence scheme. The simulation will be used to obtain estimations for the performance of the scheme. In a next step, the laser setup will be presented as well as the offset-lock system used for stabilizing the relative frequency of the used lasers. After showing the results of a Rabi oscillation measurement and explaining the setup at the atom position finally, Raman sideband cooling will be demonstrated.

**Chapter 5** concludes the results of this work and gives an outlook for possible next steps in the near future.





# Chapter 2

## Atom-Light Interaction

Large parts of the work in this thesis are about or build upon optical transitions of atoms. As it is such an integral part and for many parts it is required to understand the underlying mechanism, this chapter will begin at the textbook example of the two-level atom. Building on this, the multilevel atom and three-level transitions will be introduced. The focus of the three-level transitions will be on Raman transitions.

### 2.1 The Two-Level Atom

More elaborate systems of atoms interacting with light can be well constructed from the simple model of the two-level atom in a radiation field. The following section will discuss just that based on [35, 36].

#### 2.1.1 General Schrödinger equation

The general Hamiltonian describing a hydrogen atom in an electromagnetic field consists of a part which describes the free hydrogen and a part describing the coupling between atom and field. Therefore, it can make sense to write the Hamiltonian as

$$\mathcal{H} = \mathcal{H}_0 + \mathcal{H}', \text{ with} \quad (2.1a)$$

$$\mathcal{H}_0 = \frac{\hat{\mathbf{p}}^2}{2\mu} - \frac{1}{4\pi\epsilon_0} \frac{e^2}{|\hat{\mathbf{r}}|} \quad \text{and} \quad (2.1b)$$

$$\mathcal{H}' = -e\hat{\mathbf{r}}\hat{\mathbf{E}}_{EM}(t). \quad (2.1c)$$

A semi classical derivation of this Hamiltonian is given in Appendix A. The solutions to  $\mathcal{H}_0$  are the well known hydrogen electron orbitals, which can be analytically calculated as for example done detailed in [37]. For the generalized wavefunctions

$$|\psi(\mathbf{r}, t)\rangle = \sum_l c_l(t) |\phi_l(\mathbf{r})\rangle e^{-\frac{i}{\hbar} E_l t}, \quad (2.2)$$

composed of the eigenfunctions  $|\phi_l(\mathbf{r})\rangle e^{-\frac{i}{\hbar}E_l t}$  and the corresponding eigenenergies  $E_l$  of  $\mathcal{H}_0$ , the Schrödinger equation becomes

$$\sum_l (E_l c_l(t) + i\hbar \dot{c}_l(t)) |\phi_l(\mathbf{r})\rangle e^{-\frac{i}{\hbar}E_l t} = \sum_l (\mathcal{H}_0 + \mathcal{H}') c_l(t) |\phi_l(\mathbf{r})\rangle e^{-\frac{i}{\hbar}E_l t}. \quad (2.3)$$

By multiplication of  $\langle \phi_k(\mathbf{r})|$  from the left, and solving for  $\dot{c}_k(t)$ , the equation

$$i\hbar \dot{c}_k(t) = \sum_l c_l(t) \langle \phi_k(\mathbf{r})| \mathcal{H}' |\phi_l(\mathbf{r})\rangle e^{\frac{i}{\hbar}(E_k - E_l)t} \quad (2.4)$$

arises. In general this is not solvable analytically. In these cases time-dependent perturbation theories, as in [38, 39], can be applied.

### 2.1.2 The Rabi-Problem

If, however, the atom is reduced to a two-level atom, the problem can be solved analytically. By doing so, the system of differential equations reduces to the two equations

$$i\hbar \dot{c}_g(t) = -c_e(t) e E_0 \boldsymbol{\varepsilon}(t) \cos(\omega t - kz + \phi) \langle g | \hat{\mathbf{r}} | e \rangle e^{-i\omega_{eg}t} \quad \text{and} \quad (2.5a)$$

$$i\hbar \dot{c}_e(t) = -c_g(t) e E_0 \boldsymbol{\varepsilon}(t) \cos(\omega t - kz + \phi) \langle e | \hat{\mathbf{r}} | g \rangle e^{i\omega_{eg}t}, \quad (2.5b)$$

where  $g$  and  $e$  denote the ground and excited state, and  $\omega_{ge} = (E_g - E_e)/\hbar$ . Furthermore, the electromagnetic field was expressed as  $\hat{\mathbf{E}}_{EM}(t) = E_0 \boldsymbol{\varepsilon}(t) \cos(\omega t - kz)$ , where  $E_0$ ,  $\boldsymbol{\varepsilon}(t)$ ,  $\phi$  and  $\omega$  are the electric field amplitude, the polarization unit vector, a phase constant and the frequency of the electromagnetic field respectively. If the cosines are written in exponential form the exponential terms become  $e^{-i(\omega_{eg} + \omega)t} + e^{-i(\omega_{eg} - \omega)t}$  and  $e^{i(\omega_{eg} + \omega)t} + e^{i(\omega_{eg} - \omega)t}$ . Near the two-level resonance the approximation  $\omega + \omega_{ge} = 2\omega_{ge}$  can be made. Additionally the frequency difference will be expressed as

$$\omega - \omega_{eg} = \delta. \quad (2.6)$$

Since in this case  $2\omega_{eg} \gg \delta$ , the exponential terms oscillating with  $2\omega_{eg}$  will quickly average out on timescales relevant for the transition and will mainly be determined by the slow  $\delta$  oscillations. This gives reason for what is called the rotating wave approximation, which disregards of the fast  $2\omega_{eg}$  oscillations. By further setting the position and phase to zero and using the definition of the Rabi frequency,

$$\Omega \stackrel{\text{def}}{=} -\frac{eE_0}{\hbar} \langle e | \hat{\mathbf{r}} | g \rangle, \quad (2.7)$$

the Hamiltonian in matrix notation can be written as

$$\mathcal{H}' = \frac{\hbar}{2} \begin{pmatrix} 0 & \Omega e^{i\delta t} \\ \Omega^* e^{-i\delta t} & 0 \end{pmatrix}. \quad (2.8)$$

In this treatment the polarization of the electromagnetic field is neglected. Using the Hamiltonian in the rotating wave approximation, one can find the two differential equations

$$\ddot{c}_g - i\delta\dot{c}_g + \frac{|\Omega|^2}{4}c_g = 0 \quad (2.9a)$$

$$\ddot{c}_e + i\delta\dot{c}_e + \frac{|\Omega|^2}{4}c_e = 0. \quad (2.9b)$$

For the initial conditions  $c_g(t=0) = 1$ ,  $c_e(t=0) = 0$  and the normalization condition the solutions are

$$c_g = \left( \cos\left(\frac{\Omega'}{2}t\right) - i\frac{\delta}{\Omega'} \sin\left(\frac{\Omega'}{2}t\right) \right) e^{i\delta t/2} \quad (2.10a)$$

$$c_e = -i\frac{\Omega}{\Omega'} \sin\left(\frac{\Omega'}{2}t\right) e^{-i\delta t/2}. \quad (2.10b)$$

$\Omega'$  denotes the effective Rabi frequency

$$\Omega' = \sqrt{\Omega^2 + \delta^2}. \quad (2.11)$$

Therefore, the amplitude of the transition is given by

$$a = \frac{\Omega}{\Omega'} = \frac{\Omega}{\sqrt{\Omega^2 + \delta^2}} \quad (2.12)$$

and thus the maximum probability to find the atom in the excited state is

$$\max(c_e^* c_e) = a^2 = \frac{\Omega^2}{\Omega'^2} = \frac{\Omega^2}{\Omega^2 + \delta^2}. \quad (2.13)$$

In order to get rid of the time dependence in Eq. 2.8, the rotating frame transformation,  $|\psi\rangle \rightarrow \hat{T}|\psi\rangle$ , can be applied. The transformation operation can be expressed as

$$\hat{T}(t) = \begin{pmatrix} e^{-i\delta t/2} & 0 \\ 0 & e^{i\delta t/2} \end{pmatrix}. \quad (2.14)$$

Since this transformation is time dependent the Hamiltonian has to be extended to satisfy the Schrödinger equation as shown with Eq. A.34. The Hamiltonian in the

rotating frame is then

$$\mathcal{H}'_R = \hat{T} \left( \mathcal{H}' - i\hbar \frac{\partial}{\partial t} \right) \hat{T}^\dagger = \frac{\hbar}{2} \begin{pmatrix} \delta & \Omega \\ \Omega^* & -\delta \end{pmatrix}. \quad (2.15)$$

The eigenstates of Eq. 2.15 are in general not the ground and excited states  $|g\rangle$  and  $|e\rangle$  anymore. The eigenvalues can be calculated and, in second order series expansion for  $\Omega$ , approximated to be

$$E_{\pm} = \pm \frac{\hbar}{2} \sqrt{|\Omega|^2 + \delta^2} \approx \pm \frac{\hbar}{2} \left( \delta + \frac{|\Omega|^2}{2\delta} \right). \quad (2.16)$$

However, in the case of  $|\delta| \gg |\Omega|$  the eigenstates can be approximated by  $|g\rangle$  and  $|e\rangle$ . In this case the energies are shifted by

$$\Delta E_{g/e} = \mp \frac{\hbar |\Omega|^2}{4\delta}. \quad (2.17)$$

Since the Rabi frequency is proportional to the electric field and thereby to the square root of the light fields intensity, by applying a field with an intensity gradient, the atoms can feel a local potential and is the cause of the dipole potential.

## 2.2 Multilevel Atoms

As mentioned in 2.1.1 the electronic wave functions for hydrogen can be found by deriving the eigenfunctions of Eq. 2.1b. This Hamiltonian can be expanded by adding the Coulomb interaction terms for all additional electrons with the atomic core and between each other to describe the system of atoms with more than one electron. This has the disadvantage that this problem cannot be solved analytically anymore and has to be solved numerically. As more detailed explained in [37] the central-field approximation can be used to simplify this problem for alkali atoms by approximating the Coulomb interaction between electrons with a central-field which only depends on the relative position between the electrons and the nucleus. This allows to separate the problem and write the atomic wave function as a product of single electron wave functions. Subsequently the Hartree-Fock method can be used to iteratively improve the initial guess for a central-field potential and thus the atomic wave function.

### 2.2.1 Energy Scheme

The wavefunctions of the electrons can be separated into an radial and a angular part and can be completely described by the quantum numbers  $n$ ,  $l$  and  $m_l$ , denoting

the principal, orbital and magnetic quantum numbers. These quantum numbers are integer values and are restricted to  $0 \leq l < n$  and  $|m| \leq l$ . In the case of the hydrogen atom, without any additional interactions than the Coulomb interaction, the states with the same principal quantum number are degenerate. However, if the spin of the electron  $\mathbf{s}$  is considered, there will be an interaction between the spin and the magnetic field generated by the moving electron. The interaction is proportional to  $\hat{l} \cdot \hat{s}$ , where  $\hat{l}$  is the orbital momentum operator and  $\hat{s}$  is the spin operator. This spin-orbit coupling causes a energy shift for the  $l \neq 0$  cases depending on the orientation of the spin relative to the magnetic field caused by the electron orbit. For this reason an additional quantum number, the total electronic angular momentum  $\mathbf{j} = \mathbf{l} + \mathbf{s}$  is introduced. Together with relativistic corrections the new energy scheme is called the fine structure. For other atomic species, depending on the spin-orbit coupling strength, the total electronic angular momentum is either given by  $\mathbf{J} = \sum_i \mathbf{j}_i$  for bigger atoms or by  $\mathbf{J} = \mathbf{L} + \mathbf{S}$  for smaller atoms, where  $\mathbf{L} = \sum_i \mathbf{l}_i$  is the total orbital momentum and  $\mathbf{S} = \sum_i \mathbf{s}_i$  is the total spin angular momentum. The corresponding quantum number  $J$  can take the values  $|L - S|, |L - S + 1|, \dots, |L + S - 1|, L + S$ . The new magnetic quantum number  $m_J$  can take the values  $-J, -J + 1, \dots, J - 1, J$ . Another correction has to be made when the nuclear spin  $I$  is taken into account. Its coupling with the total electronic angular momentum, which is proportional to  $\hat{I} \cdot \hat{J}$ , gives rise for a total angular momentum  $\mathbf{F} = \mathbf{I} + \mathbf{J}$ . Similar to  $J$  the corresponding quantum number  $F$  can take the values  $|J - I|, |J - I + 1|, \dots, |J + I - 1|, J + I$ . The modified energy structure is called hyperfine structure. The related magnetic quantum number  $m_F$  can take the values  $-F, -F + 1, \dots, F - 1, F$ , which gives a total of  $2F + 1$  magnetic sublevels. According to the Zeeman effect, these magnetic or Zeeman sublevels are not degenerate when an external magnetic field is applied. The energy shift by an external magnetic field  $B$  is given by

$$\Delta E_{Zeeman} = g_F \mu_B m_F B \quad (2.18)$$

with the Landé g-factors

$$g_F = g_J \cdot \frac{F(F + 1) + J(J + 1) - I(I + 1)}{2F(F + 1)}, \quad (2.19a)$$

$$g_J = 1 + \frac{J(J + 1) + S(S + 1) - L(L + 1)}{2J(J + 1)} \quad (2.19b)$$

and the Bohr magneton  $\mu_B = e\hbar/2m_e c$ . The so far introduced quantum numbers are sufficient to fully describe the internal atomic state of an atom. The internal state is denoted as

$$n^{2S+1} L_J(F, m_F). \quad (2.20)$$

In this notation  $L$  is not written as its integer value but as the corresponding orbital letter  $S, P, D, F, \dots$ .

Alkali atoms have a very convenient internal structure. They consist of the closed structure of the previous noble gas plus an additional valence electron in the next  $S$ -orbital, so that  $L = l$  and  $S = s$  for the quantum numbers of the valence electron. The hyperfine energy scheme for  $^{87}\text{Rb}$  is shown in Appendix B.

## 2.2.2 Dipole Coupling

In order to calculate the coupling between two hyperfine states for a optical transition it is necessary to calculate the overlap integral for the Rabi frequency

$$\Omega = -\frac{eE_0}{\hbar} \langle \alpha', F', m'_F | \mathbf{r} \boldsymbol{\varepsilon} | \alpha, F, m_F \rangle. \quad (2.21)$$

For this purpose it is practical to switch into the spherical basis defined by the basis set

$$\hat{e}_{\pm 1} = \mp \frac{1}{\sqrt{2}} (\hat{e}_x \pm i\hat{e}_y) = -\hat{e}_{\mp 1}^*, \quad (2.22)$$

$$\hat{e}_0 = \hat{e}_z = \hat{e}_0^*. \quad (2.23)$$

Written in the new basis components  $r_q = \mathbf{r} \hat{e}_q$ ,  $\mathbf{r}$  becomes

$$\mathbf{r} = \sum_q (-1)^q r_q \hat{e}_{-q} = \sum_q r_q \hat{e}_q^*. \quad (2.24)$$

This way the Rabi frequency can be written as

$$\Omega = -\frac{eE_0}{\hbar} \sum_q \varepsilon_q^* \langle \alpha', F', m'_F | r_q | \alpha, F, m_F \rangle. \quad (2.25)$$

$\varepsilon_q$  is the projection of the polarization unit vector on the spherical basis and the dipole component index  $q = 0, \pm 1$  specifies the polarization type with respect to the quantization axis  $\hat{e}_z$ . As shown for example in [38] the Wigner-Eckart theorem can be applied for the overlap integral, such that

$$\langle \alpha', F', m'_F | r_q | \alpha, F, m_F \rangle = \langle F', m'_F | F, 1, m_F, q \rangle \langle \alpha', F' || \mathbf{r} || \alpha, F \rangle. \quad (2.26)$$

The first term in Eq. 2.26 is a Clebsch-Gordan coefficient, which is proportional to the Wigner 3-j symbol and can be expressed as

$$\langle F', m'_F | F, 1, m_F, q \rangle = (-1)^{F'-1+m_F} \sqrt{2F+1} \begin{pmatrix} F' & 1 & F \\ m'_F & q & -m_F \end{pmatrix}. \quad (2.27)$$

The second term in Eq. 2.26 is a reduced matrix element which itself is proportional to a further reduced matrix element and the Wigner 6-j symbol by

$$\begin{aligned} \langle \alpha', F' || \mathbf{r} || \alpha, F \rangle &= \langle \alpha', J' || \mathbf{r} || \alpha, J \rangle (-1)^{F'+J+1+I} \\ &\cdot \sqrt{(2F'+1)(2J+1)} \left\{ \begin{matrix} J & J' & 1 \\ F' & F & I \end{matrix} \right\}. \end{aligned} \quad (2.28)$$

The second reduced matrix element can be reduced even further, but also can be determined empirically. Over the equation

$$\frac{1}{\tau} = \frac{\omega_0^3 e^2}{3\pi\epsilon_0 \hbar c^3} \frac{2J+1}{2J'+1} |\langle \alpha', J' || \mathbf{r} || \alpha, J \rangle|^2 \quad (2.29)$$

it is connected to the decay time of the respective  $J' \rightarrow J$  decay. The empirical determined value for  $^{87}\text{Rb}$  can be found in [40]. This way the Rabi frequency is given by

$$\Omega = -\frac{eE_0}{\hbar} \langle \alpha', J' || \mathbf{r} || \alpha, J \rangle \sum_q \varepsilon_q^* G(F', F, J', J, m'_F, m_F, I, q) \quad (2.30)$$

with the geometrical factor

$$\begin{aligned} G(F', F, J', J, m'_F, m_F, I, q) &= (-1)^{2F'+J+I+m_F} \sqrt{(2F'+1)(2F+1)(2J+1)} \\ &\cdot \begin{pmatrix} F' & 1 & F \\ m'_F & q & -m_F \end{pmatrix} \left\{ \begin{matrix} J & J' & 1 \\ F' & F & I \end{matrix} \right\}. \end{aligned} \quad (2.31)$$

From the Wigner 3-j and 6-j symbols the selection rules for optical transitions can be extracted, since both only are not zero when the conditions

1.  $\Delta J = J' - J = 0, \pm 1$ , except for  $J = 0 \rightarrow J' = 0$ ,
2.  $\Delta F = F' - F = 0, \pm 1$ , except for  $F = 0 \rightarrow F' = 0$ ,
3.  $\Delta m_F = m'_F - m_F = -q$

are met. As described in [41] and summarized in Tab. 2.1, if the EM-field is such that the polarization  $\varepsilon$  is parallel to the quantization axis  $\hat{e}_z$  the interaction drives a  $\pi_0$  transition with  $\Delta m_F = 0$ . For the case of an EM-field which is moving in the direction of the quantization axis and has a clockwise rotating or right-circular polarization (RCP) it drives a  $\sigma^-$  transition with  $\Delta m_F = -1$ . This case is equivalent to an EM-field with left-circular polarization (LCP) which is moving contra-directional to the quantization axis, since relative to the quantization axis the polarization is rotating in the same direction for both cases. In the case of a LCP EM-field which moves in the direction of  $\hat{e}_z$  a  $\sigma^+$  transition is driven. Analog to the  $\sigma^-$  the  $\sigma^+$  transition is also driven for propagation contra-directional to  $\hat{e}_z$  with RCP. Linear polarization along  $\hat{e}_{x/y}$  drive the transitions  $\pi^\pm = (\sigma^+ \pm \sigma^-)/\sqrt{2}$ .

Polarization	Transition	$\Delta m_F$
RCP $\mathbf{k} \parallel \hat{e}_z$ , LCP $\mathbf{k} \perp \hat{e}_z$	$\sigma^-$	$-1$
LCP $\mathbf{k} \parallel \hat{e}_z$ , RCP $\mathbf{k} \perp \hat{e}_z$	$\sigma^+$	$+1$
$\varepsilon \parallel \hat{e}_z$	$\pi^0$	$0$
$\varepsilon \parallel \hat{e}_x$	$\pi^+ = (\sigma^+ + \sigma^-)/\sqrt{2}$	$\pm 1$
$\varepsilon \parallel \hat{e}_y$	$\pi^- = (\sigma^+ - \sigma^-)/\sqrt{2}$	$\pm 1$

**Tab. 2.1:** Correspondence between polarization, transition type and change of the magnetic quantum number.  $\mathbf{k}$  describes the wave vector of the EM-field. From [41].

### 2.2.3 Spontaneous Decay

The previously derived geometrical factor  $G$  in Eq. 2.31 shows a symmetry given by

$$\sum_{q,F} |G(F', F, J', J, m'_F, m'_F + q, I, q)|^2 = \frac{2J+1}{2J'+1}. \quad (2.32)$$

The same factor appears in Eq. 2.29 for calculating the decay rate of a fine structure state. According to [40] this can be interpreted as that every magnetic hyperfine level of the same fine structure state decays with the same rate but branches into different ground states with different decay rates. This relation can thus be used to calculate the decay rate for a specific decay path with

$$\Gamma_{F,m_F,F',m'_F} = \frac{1}{\tau} \frac{2J'+1}{2J+1} G(F', F, J', J, m'_F, m_F, I, m_F - m'_F). \quad (2.33)$$

## 2.3 Three-Level Transitions

This section will mainly address the phenomenon of Raman transitions, which occur in the three level model. A brief note will be given about coherent population trapping (CPT), as it might cause slowing or a total freezing of transitions if not considered. The three level model offers a couple more interesting phenomena beyond these two, such as electromagnetically induced transparency [42] or stimulated rapid adiabatic passage [43]. These and other three-level problems are introduced in [36], which, together with [41], also serves as a basis for this section.

### 2.3.1 Interaction Hamiltonian

As explained in [41] the Hamiltonian for a three level system with two different EM-fields coupling them can be described with

$$\mathcal{H} = \frac{\hbar}{2} \begin{pmatrix} 2\omega_1 & 0 & \Omega_{11}e^{i\omega_{L1}t} \\ 0 & 2\omega_2 & \Omega_{22}e^{i\omega_{L2}t} \\ \Omega_{11}^*e^{-i\omega_{L1}t} & \Omega_{22}^*e^{-i\omega_{L2}t} & 2\omega_3 \end{pmatrix} \quad (2.34)$$



where the position and the constant phase term in the argument of the oscillatory term  $\cos(\omega t - \mathbf{k}\mathbf{r} + \phi)$  were set to zero and the rotating wave approximation was already made. The Hamiltonian is the combination of two two-level couplings with both couplings sharing the same excited state. By using the transformation

$$\hat{T} = e^{iH_0 t/\hbar}, \text{ with} \quad (2.35)$$

$$H_0 = \hbar \begin{pmatrix} \omega_1 & 0 & 0 \\ 0 & \omega_2 & 0 \\ 0 & 0 & \omega_3 \end{pmatrix}, \quad (2.36)$$

the Hamiltonian can be written as

$$\mathcal{H} = \frac{\hbar}{2} \begin{pmatrix} 0 & 0 & \Omega_{11}e^{-i\Delta_{11}t} \\ 0 & 0 & \Omega_{22}e^{-i\Delta_{22}t} \\ \Omega_{11}^*e^{i\Delta_{11}t} & \Omega_{22}^*e^{i\Delta_{22}t} & 0 \end{pmatrix}, \quad (2.37)$$

where  $\Delta_{nm} = \omega_3 - \omega_n - \omega_{Lm}$ .

### 2.3.2 Raman Transition

Technically, in Eq. 2.34 the off-diagonal non zero elements are missing an additional term, but after some further rewriting these terms will only contribute on the diagonal elements. They will be accounted for later. In Eq. 2.37 the  $\Delta_{22}$  detuning can be expressed as

$$\Delta_{22} = \Delta + \delta, \text{ with} \quad (2.38)$$

$$\delta = \omega_{L1} - \omega_{L2} + \omega_1 - \omega_2 \text{ and} \quad (2.39)$$

$$\Delta = \Delta_{11}, \quad (2.40)$$

such that

$$\mathcal{H} = \frac{\hbar}{2} \begin{pmatrix} 0 & 0 & \Omega_{11}e^{-i\Delta t} \\ 0 & 0 & \Omega_{22}e^{-i(\Delta+\delta)t} \\ \Omega_{11}^*e^{i\Delta t} & \Omega_{22}^*e^{i(\Delta+\delta)t} & 0 \end{pmatrix}. \quad (2.41)$$

With this Hamiltonian the differential equations

$$i\dot{c}_1(t) = \frac{\Omega_{11}}{2}e^{-i\Delta t}c_3(t) \quad (2.42a)$$

$$i\dot{c}_2(t) = \frac{\Omega_{22}}{2}e^{-i(\Delta+\delta)t}c_3(t) \quad (2.42b)$$

$$i\dot{c}_3(t) = \frac{\Omega_{11}^*}{2}e^{i\Delta t}c_1(t) + \frac{\Omega_{22}^*}{2}e^{i(\Delta+\delta)t}c_2(t) \quad (2.42c)$$

can be obtained. With some assumptions this three-level problem can be reduced to an effective two-level problem. The first assumption is to drive a far detuned Raman transition, which can be expressed as  $\Delta \gg |\Omega_{11}|, |\Omega_{22}|, |\delta|$ . In this case, considering  $|3\rangle$  an excited state, which decays spontaneously, the population of  $|3\rangle$  can be neglected. Secondly it is assumed that the oscillation of  $\dot{c}_1$  and  $\dot{c}_2$  is much slower than the oscillation of  $\dot{c}_3$ . In this assumption  $c_1$  and  $c_2$  can be seen as constant on the relevant timescales for  $\dot{c}_3$ . With constant coefficients  $c_3$  can be evaluated by integrating  $\dot{c}_3$ , which gives

$$\int_{t_0}^{t_0+t} \dot{c}_3(t) dt = [c_3(t_0+t) - c_3(t_0)] = - \left[ \frac{\Omega_{11}^*}{2\Delta} e^{i\Delta t} c_1(t) + \frac{\Omega_{22}^*}{2\Delta} e^{i\Delta_{11}t} c_1(t) \right]. \quad (2.43)$$

It was also used that  $\Delta_{11} \gg \delta$ . With this relation the differential equations can be written as

$$i\dot{c}_1(t) = -\frac{|\Omega_{11}|^2}{4\Delta_{11}} c_1(t) - \frac{\Omega_{11}\Omega_{22}^*}{4\Delta_{11}} e^{i\delta t} c_2(t) \quad (2.44a)$$

$$i\dot{c}_2(t) = -\frac{\Omega_{22}\Omega_{11}^*}{4\Delta_{11}} e^{-i\delta t} c_1(t) - \frac{|\Omega_{22}|^2}{4\Delta_{11}} c_2(t) \quad (2.44b)$$

$$i\dot{c}_3(t) = \frac{\Omega_{11}^*}{2} e^{i\Delta_{11}t} c_1(t) + \frac{\Omega_{22}^*}{2} e^{i(\Delta_{11}+\delta)t} c_2(t). \quad (2.44c)$$

The fast  $\Delta_{11}$  oscillations for  $\dot{c}_3$  quickly average out. Therefore,  $\dot{c}_3$  can be disregarded and the problem reduces to an effective two-level problem, which is described by the Hamiltonian

$$\mathcal{H} = -\hbar \begin{pmatrix} \Omega_1^{\text{AC}} & \Omega_R e^{i\delta t}/2 \\ \Omega_R^* e^{-i\delta t}/2 & \Omega_2^{\text{AC}} \end{pmatrix}. \quad (2.45)$$

The Raman-Rabi frequency is given by

$$\Omega_R = \frac{\Omega_{11}\Omega_{22}^*}{2\Delta} \quad (2.46)$$

and the light shift is given by

$$\Omega_n^{\text{AC}} = \sum_a \frac{|\Omega_{na}|^2}{4\Delta_{na}}. \quad (2.47)$$

Here  $n$  indicates the internal state on which the respective EM-field, indicated by  $a$ , acts on. The transition amplitude can be calculated in a similar manner as done in 2.1.2. As derived in [44], the amplitude is then given by

$$a = \frac{\Omega_R}{\tilde{\Omega}_R} = \frac{\Omega_R}{\sqrt{\Omega_R^2 + (\delta_{AC} - \delta)^2}}, \quad (2.48)$$

where

$$\tilde{\Omega}_R = \sqrt{\Omega_R^2 + (\delta_{AC} - \delta)^2} \quad (2.49)$$

is the effective Rabi frequency and

$$\delta_{AC} = \Omega_1^{\text{AC}} - \Omega_2^{\text{AC}} \quad (2.50)$$

is the differential light shift.

The two Hamiltonians Eq. 2.41 and Eq. 2.45 are simulated for comparison in Fig. 2.1. It can be observed, that even though simulated with two different Hamiltonians, but the same parameters, the oscillation frequency and amplitude between the two ground states is nearly the same. And in the case of the three level system the population in the excited state is negligible.

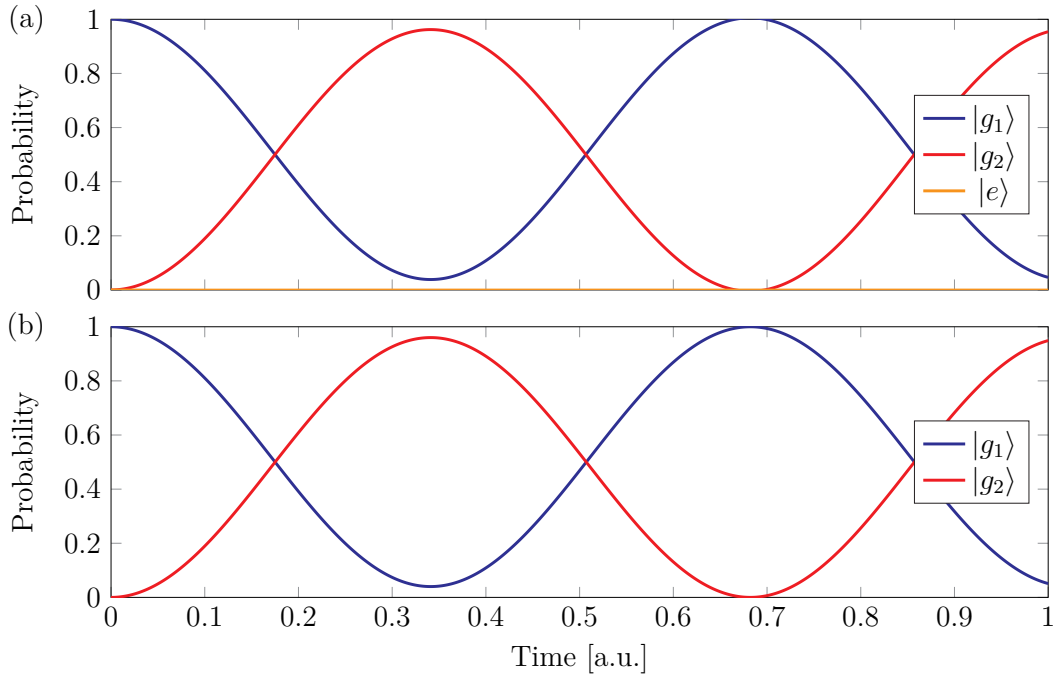


**Fig. 2.1:** Numerical calculation of a closed three level systems time evolution demonstrating Raman transitions. The states  $|g_1\rangle$  and  $|g_2\rangle$  are coupled to  $|e\rangle$  by  $-50$  GHz detuned lasers. In (a) the time evolution is explicitly simulated with the three level system. (b) shows the time evolution of the effective two level system. It can be seen that for the same parameters the two different simulations have nearly the same oscillation frequency and amplitude.

With a multilevel atom the Raman transition can go over multiple routes as the EM-field couples the ground states to multiple excited hyperfine states. In this case a vector notation for the Rabi frequency can be used. For the single EM-field Rabi

frequency this looks like

$$\mathbf{\Omega}_F = \sum_{F'} \Omega_{|F, m_F\rangle |F', m'_F\rangle} \hat{\mathbf{e}}_i, \quad (2.51a)$$

$$\mathbf{\Omega}_F = -\frac{eE_0}{\hbar} \langle \alpha', J' || \mathbf{r} || \alpha, J \rangle \sum_{F'} G(F', F, J', J, m'_F, m_F, I, q) \hat{\mathbf{e}}_i \quad (2.51b)$$

$$= -\frac{eE_0}{\hbar} \langle \alpha', J' || \mathbf{r} || \alpha, J \rangle \mathbf{G}_F. \quad (2.51c)$$

$F$  denotes the hyperfine ground state under investigation and  $F'$  indicates the hyperfine states of the considered excitation path. Eq. 2.51b and Eq. 2.51c only apply for pure polarization  $q$ . In the limit where the Raman detuning from the excited state is large compared to the hyperfine splitting of the excitation line,  $\Delta_R \gg \Delta_{HF}$ , the detuning to all excited hyperfine states can be considered the same and the Raman Rabi frequency can be written as

$$\Omega_R = \frac{\mathbf{\Omega}_{F1} \cdot \mathbf{\Omega}_{F2}^*}{2\Delta} \quad (2.52a)$$

$$= -\frac{e^2 E_1 E_2^*}{2\Delta \hbar^2} |\langle \alpha', J' || \mathbf{r} || \alpha, J \rangle|^2 |\mathbf{G}_{F1} \cdot \mathbf{G}_{F2}|. \quad (2.52b)$$

A few statements about the Raman transition path can be made by investigating the term  $|\mathbf{G}_{F1} \cdot \mathbf{G}_{F2}|$ . First of all, for a transition to work, the two coupled magnetic ground states have to be coupled by matching  $q$ . Since  $q = 0, \pm 1$  a theoretical maximum of  $|\Delta m_F| = 2$  is possible. Also, since for one photon transitions the  $F$  quantum number can only change by one, the maximum  $|\Delta F| = 2$ .  $^{87}\text{Rb}$  only has two hyperfine ground states, so the maximum  $|\Delta F| = 1$ .

By calculating  $|\mathbf{G}_{F1} \cdot \mathbf{G}_{F2}|$  for the respective transitions, it can be seen that it gets

Transition	Coupled ground states	via
$\sigma^- - \sigma^-$	$ F1, m_F\rangle \leftrightarrow  F2, m_F\rangle$	$ F', m_F - 1\rangle$
$\sigma^+ - \sigma^+$	$ F1, m_F\rangle \leftrightarrow  F2, m_F\rangle$	$ F', m_F + 1\rangle$
$\pi^0 - \sigma^-$	$ F1, m_F\rangle \leftrightarrow  F2, m_F + 1\rangle$	$ F', m_F\rangle$
$\pi^0 - \sigma^+$	$ F1, m_F\rangle \leftrightarrow  F2, m_F - 1\rangle$	$ F', m_F\rangle$
$\pi^0 - \pi^\mp$	$ F1, m_F\rangle \leftrightarrow  F2, m_F + 1\rangle$ $ F1, m_F\rangle \leftrightarrow  F2, m_F - 1\rangle$	$ F', m_F\rangle$
$\pi^\pm - \pi^\mp$	$ F1, m_F\rangle \leftrightarrow  F2, m_F\rangle$	$ F', m_F - 1\rangle$ $ F', m_F + 1\rangle$

**Tab. 2.2:** Raman transition paths.  $F'$  denotes all excited hyper fine levels that are couple to both  $F1$  and  $F2$  by the transition under investigation. From [41].

zero for transitions with  $|\Delta m_F| = 2$ . For the exact calculation with the specific detunings for the respective excited hyperfine levels this transition will still be possible but depending on the detuning strongly suppressed. Expressed in the symbols from Tab. 2.1 these transitions are labeled  $\sigma^\pm - \sigma^\mp$  and  $\pi^\pm - \pi^\pm$ , where each symbol

describes the transition type of the respective EM-field. This is also the case for  $\pi^0 - \pi^0$  transitions, which would drive  $\Delta m_F = 0$  transitions.

Possible transition paths are those denoted by  $\sigma^\pm - \sigma^\pm$  and  $\pi^\pm - \pi^\mp$ , which drive  $\Delta m_F = 0$  transitions, and  $\pi^0 - \sigma^\pm$  and  $\pi^0 - \pi^\pm$ , which drive  $\Delta m_F = \pm 1$  transitions. The not suppressed transitions are summarized in Tab. 2.2.

### 2.3.3 Coherent Population Trapping

As coherent population trapping is not of primary interest for the goal of developing a Raman sideband cooling scheme, but holds the potential to strongly influence it if not considered, it is just mentioned here that in the case of a resonant coupling of two states with a third state, a time independent eigenstate exists. Even if initially not starting in this eigenstate, spontaneous emission may drive the system into said state eventually. This can be avoided by driving one of the transitions slightly

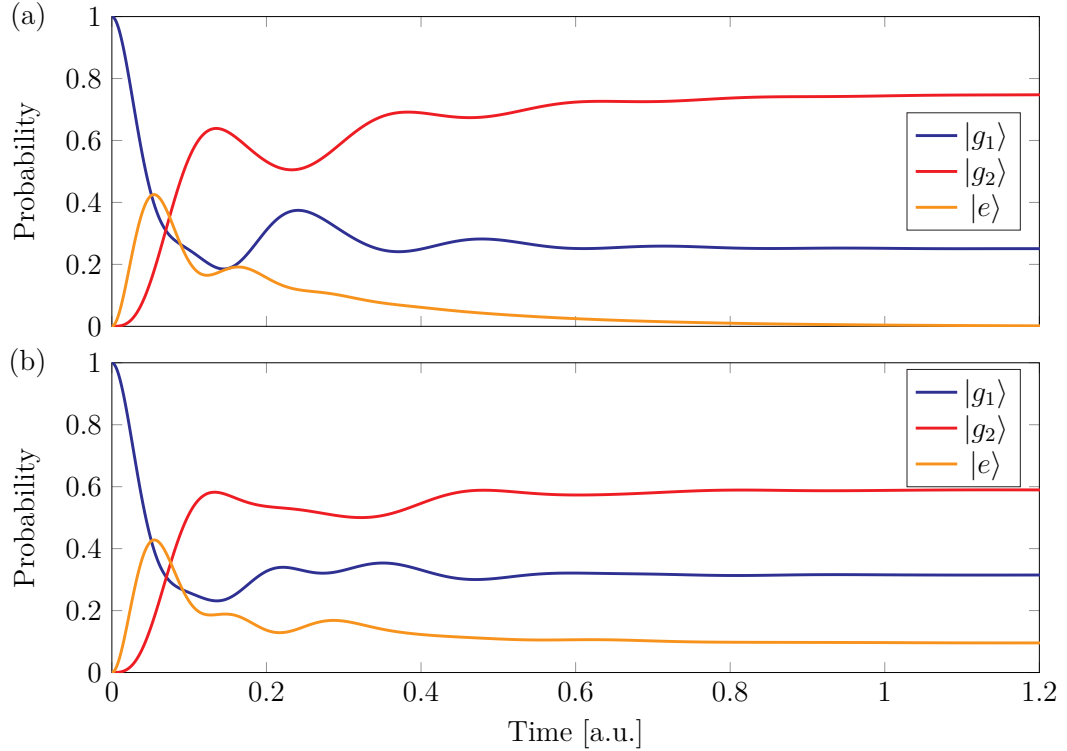


**Fig. 2.2:** Numerical calculation of a closed three level systems time evolution demonstrating coherent population trapping. The states  $|g_1\rangle$  and  $|g_2\rangle$  are coupled to  $|e\rangle$  by resonant lasers. In (a) coherent population trapping due to spontaneous emission can be observed. After a certain period of time the spontaneous emission leads the atom to occupy an eigenstate of the three level system. In this eigenstate no excitation can be observed. The ratio of the occupation probabilities of the eigenstate is determined by the ratio of the Rabi frequencies driving the transitions. In (b) a sufficiently high detuning to one of the lasers is introduced. All other parameters are equal to (a). The system still goes into a stable state due to decoherence from the spontaneous emission, such that after a while no change of the probability is observable but it can be seen that there still is a probability to find an excited atom.

detuned in the order of half the excited state linewidth. In Fig. 2.2 a three-level

system with both beams in resonance and with one beam off resonance is shown to visualize how over time the system is either driven in the trapped eigenstate or still exhibits excitation probability.

## 2.4 Conclusion

This chapter covered the optical transitions that will be of importance later on. Beginning with the two-level textbook example, the Rabi frequency is defined and the dynamics of the system are investigated. Proceeding, the picture was extended to that of a multilevel atom. With the help of convenient geometrical relations the Rabi frequencies between specific magnetic hyperfine states can be calculated. Furthermore, the branching ratios of the excited states were derived. In the last section Raman transitions were discussed, especially for the far detuned regime, where the Rabi frequencies can be written as vectors for the corresponding paths. A short note on coherent population trapping was given to avoid possible problems with more elaborate transition schemes.

# Chapter 3

## Optical Lattice

If in addition to the internal transitions also transitions between quantized motional state are supposed to take place, it is necessary to know the eigenfunctions of the system to calculate the expected coupling. As the quantum gas microscope experiment under construction will work with a optical lattice as a basis for the physical experiment and with the same lattice as a pinning lattice for single site resolved fluorescence imaging. The eigenfunctions of a periodic system, as lattices are, are described by the delocalized Bloch functions. The Bloch functions can be used to obtain the localized Wannier functions. The coupling between different motional states in the lattice is then given by the overlap integral of the respective Wannier functions.

As it is the geometry implemented at this experimental setup in the following the triangular lattice will be introduced and the Bloch theorem will be applied to calculate its band structure.

The corresponding Bloch functions are delocalized wave functions. However, the wave functions of strongly confined particles are better expressed with localized wave functions. Therefore the Wannier functions for the first two bands will be calculated and used to determine the expected coupling between neighboring vibrational levels. This numerical evaluation will be compared to the estimation in the Lamb-Dicke regime, which is often used for similar purposes in potentials deep enough, that they can be approximated by a harmonic trap.

### 3.1 Triangular Lattice

Before any calculations about the coupling can be made it is necessary to calculate the the trapping potential. As explained in [45], the dipole potential for far-off-resonant light is given by

$$U_{dip} = \frac{3\pi c^2}{2\omega_0^3} \frac{\Gamma}{\Delta} I = \alpha I, \quad (3.1)$$

where  $\omega_0$  is the resonance frequency and  $\Gamma$  the decay rate for the considered transition.  $\Delta = \omega - \omega_0$  is the detuning from the resonance frequency.  $I$  describes the intensity of the used electromagnetic field. For simplicity in the following discussion the considered light fields are treated as plane waves. In general the transversal intensity distribution is spatially dependent, which would make the potential spatially dependent as well.

In [24] the first realization of a triangular lattice is demonstrated by using three laser beams angled  $120^\circ$  to each other in the same plane. The superposition of the electric fields can then be given by

$$E(\mathbf{r}, t) = \sum_i^3 E_{0,i} \exp(-i(\omega t - \mathbf{k}_i \mathbf{r} - \phi_i)). \quad (3.2)$$

The intensity is proportional to the absolute square of the electric field and can be written as

$$I(\mathbf{r}) = \frac{1}{2} \epsilon_0 c |E(\mathbf{r}, t)|^2 = \sum_i \sum_j \sqrt{I_{0,i} I_{0,j}} \cos(\Delta \mathbf{k}_{i,j} \mathbf{r} + \Delta \phi_{i,j}). \quad (3.3)$$

The  $\Delta \mathbf{k}_{i,j}$  and  $\Delta \phi_{i,j}$  are the relative momenta and constant phase offsets respectively. As the phase offsets just shift the lattice, they can be set to zero as it does neither influences the eigenstates except for a spatial displacement. As the wave vectors are rotated by  $120^\circ$  relative to each other, they can be represented as

$$\mathbf{k}_1 = k_L \mathbf{e}_y, \quad (3.4a)$$

$$\mathbf{k}_2 = k_L \left( \frac{\sqrt{3}}{2} \mathbf{e}_x - \frac{1}{2} \mathbf{e}_y \right) \quad \text{and} \quad (3.4b)$$

$$\mathbf{k}_3 = k_L \left( -\frac{\sqrt{3}}{2} \mathbf{e}_x - \frac{1}{2} \mathbf{e}_y \right), \quad (3.4c)$$

where  $k_L$  is absolute of the laser wave vector. These wave vectors can then be used to calculate the primitive reciprocal lattice vectors

$$\mathbf{G}_1 = \mathbf{k}_1 - \mathbf{k}_2 = G \left( -\frac{1}{2} \mathbf{e}_x + \frac{\sqrt{3}}{2} \mathbf{e}_y \right), \quad (3.5a)$$

$$\mathbf{G}_2 = \mathbf{k}_3 - \mathbf{k}_1 = G \left( -\frac{1}{2} \mathbf{e}_x - \frac{\sqrt{3}}{2} \mathbf{e}_y \right) \quad \text{and} \quad (3.5b)$$

$$\mathbf{G}_3 = -(\mathbf{G}_1 + \mathbf{G}_2) = \mathbf{k}_2 - \mathbf{k}_3 = G \mathbf{e}_x, \quad (3.5c)$$



with  $G = \sqrt{3}k_L$ . Using the equations Eq. 3.1, Eq. 3.3 and Eq. 3.5 and assuming equal intensities for all three beams the potential can be expressed as

$$\begin{aligned} \frac{U(\mathbf{r})}{\alpha I_0} &= 3 + 2 \sum_i^3 \cos(\mathbf{G}_i \mathbf{r}) \\ &= 3 + 2 \left[ \cos \left( G \left( -\frac{1}{2}x + \frac{\sqrt{3}}{2}y \right) \right) + \cos(Gx) \right. \\ &\quad \left. + \cos \left( G \left( -\frac{1}{2}x - \frac{\sqrt{3}}{2}y \right) \right) \right] \\ &= 3 + 2 \left[ \cos(Gx) + 2 \cos \left( \frac{1}{2}Gx \right) \cos \left( \frac{\sqrt{3}}{2}Gy \right) \right]. \end{aligned} \quad (3.6)$$

As it is more convenient for the calculation of the Bloch functions to write the potential in units of the recoil energy

$$E_R = \frac{\hbar^2 k_L^2}{2m} \quad (3.7)$$

the normalized potential is given by

$$\frac{U(\mathbf{r})}{U_0} = \frac{1}{3} + \frac{2}{9} \left[ \cos(Gx) + 2 \cos \left( \frac{1}{2}Gx \right) \cos \left( \frac{\sqrt{3}}{2}Gy \right) \right], \quad (3.8)$$

with  $U_0 = \text{sgn}(\Delta)sE_R$ . In Fig. 3.1 the potential of a triangular lattice is shown.

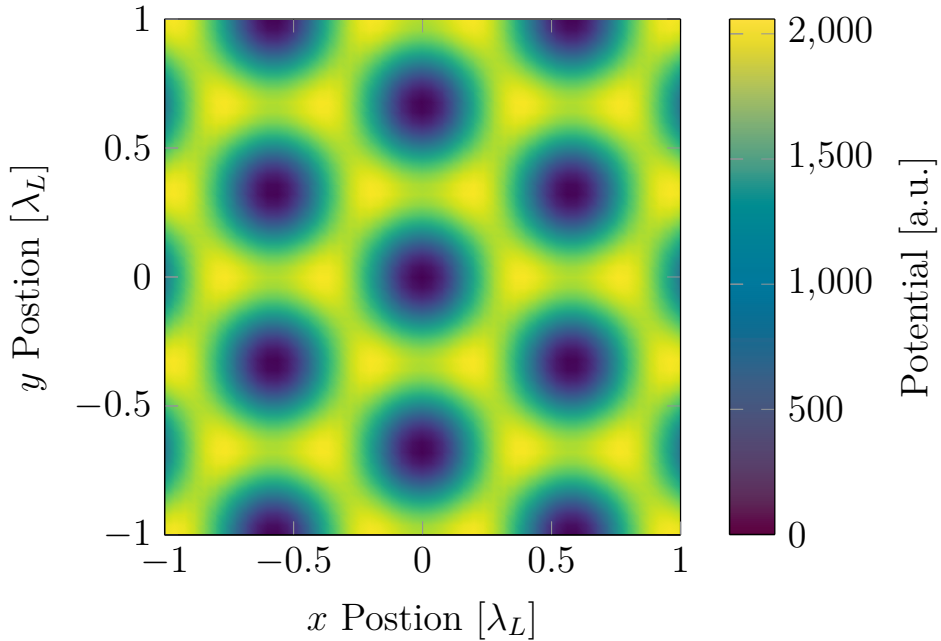


**Fig. 3.1:** Triangular lattice potential. The shown potential corresponds to the potential given by a red detuned three beam interference where the beams lie in the same plane with angles of  $120^\circ$  between the wave vectors. The position is given in units of the laser wavelength.

By a series expansion at the origin a harmonic approximation can be obtained with

$$\begin{aligned}\frac{U_{HO}(r)}{U_0} &= 1 - \frac{1}{6}G^2(x^2 + y^2) \\ &= 1 - \frac{1}{2}k_L^2(x^2 + y^2).\end{aligned}\tag{3.9}$$

In the case of red detuned beams, the signs would be inverted. If this approximation is compared to the potential of the harmonic oscillator

$$\frac{1}{2}m\omega^2(x^2 + y^2) = \frac{1}{2}sk_L^2E_R(x^2 + y^2),\tag{3.10}$$

the relation

$$\frac{\hbar^2\omega^2}{2E_R^2} = s\tag{3.11}$$

can be obtained.

For the triangular lattice implemented at the experiment a trap frequency for the triangular lattice of about 130 kHz was measured by modulation spectroscopy. This corresponds to a trap depth of  $2059E_R$ .

## 3.2 Band Structure and Wannier Functions

In such a periodic lattice the eigenfunctions of a particle can be described by the Bloch functions [46, 47]. The Bloch theorem can be used to find the eigenfunctions for systems described by a Hamiltonian

$$\mathcal{H}_0 = \frac{\mathbf{p}^2}{2m} + U(\mathbf{r}) = \frac{\hbar^2\nabla^2}{2m} + U(\mathbf{r}), \text{ with}\tag{3.12a}$$

$$U(\mathbf{r}) = U(\mathbf{r} + \mathbf{T}).\tag{3.12b}$$

$\mathbf{T}$  is a translation vector given by  $\mathbf{T} = \sum_i n_i \mathbf{a}_i$ . The  $\mathbf{a}_i$  describe the basis vectors of the lattice which can be easily found over the relation  $\mathbf{G}_i \mathbf{a}_j = 2\pi\delta_{i,j}$  to be

$$\mathbf{a}_1 = a \left( \frac{\sqrt{3}}{2} \mathbf{e}_x + \frac{1}{2} \mathbf{e}_y \right) \quad \text{and}\tag{3.13a}$$

$$\mathbf{a}_2 = a \left( -\frac{\sqrt{3}}{2} \mathbf{e}_x + \frac{1}{2} \mathbf{e}_y \right),\tag{3.13b}$$

where  $a = \frac{2}{3}\lambda_L$ . For such a system the eigenfunctions are then given by

$$\psi_{n,\mathbf{q}}(\mathbf{r}) = u_{n,\mathbf{q}}(\mathbf{r}) \exp(i\mathbf{q}\mathbf{r}).\tag{3.14}$$

As the potential the  $u_{n,\mathbf{q}}(\mathbf{r})$  obey the translation symmetry  $u_{n,\mathbf{q}}(\mathbf{r}) = u_{n,\mathbf{q}}(\mathbf{r} + \mathbf{T})$ .  $n$  denotes the band index and  $\mathbf{q}$  is the quasi-momentum. As done in [48], by using

a linear combination of plane waves as a ansatz the  $u_{n,\mathbf{q}}(r)$  can be written as

$$u_{n,\mathbf{q}}(r) = \frac{1}{\sqrt{N}} \sum_{\mathbf{K}} c_{\mathbf{K}}^{(n,\mathbf{q})} \exp(-i\mathbf{K}\mathbf{r}) \quad (3.15)$$

and the potential as

$$U(\mathbf{r}) = \sum_{\mathbf{K}} U_{\mathbf{K}} \exp(-i\mathbf{K}\mathbf{r}). \quad (3.16)$$

The sum over  $\mathbf{K} = \sum_i^N n_i \mathbf{G}_i$  is a sum over the total number of occupied lattice sites  $N$ . The  $U_{\mathbf{K}}$  are the Fourier components of the lattice potential and as elaborated in [48] they are

$$U_{\mathbf{0}} = -\frac{1}{3}V_0 \quad \text{and} \quad (3.17a)$$

$$U_{\pm G_1, \pm G_2, \pm G_3} = -\frac{1}{9}V_0. \quad (3.17b)$$

As further explained by using Eq. 3.12a, Eq. 3.14, Eq. 3.15, Eq. 3.16 and a clever substitution with  $\tilde{\mathbf{q}} = \mathbf{q}/|\mathbf{b}|$ ,  $\tilde{\mathbf{K}} = \mathbf{K}/|\mathbf{b}|$ ,  $\tilde{E}^{(n,\mathbf{q})} = (\hbar\omega^{(n,\mathbf{q})} + 1/3V_0)/E_R$  and  $\tilde{V}_0 = V_0/E_R$  the problem becomes

$$\begin{aligned} & \left( 3 (\tilde{\mathbf{q}} - \tilde{\mathbf{K}}_{n,m})^2 - \tilde{E}^{(n,\tilde{\mathbf{q}})} \right) c_{n,m}^{(n,\tilde{\mathbf{q}})} \\ & - \frac{1}{9} \tilde{V}_0 \sum_{n',m'} \left( \delta_{n,n'} \delta_{|m-m'|,1} + \delta_{m,m'} \delta_{|n-n'|,1} + \delta_{|n+m|,|n'+m'|} \delta_{|m-m'|,1} \right) c_{n',m'}^{(n,\tilde{\mathbf{q}})} \\ & = 0. \end{aligned} \quad (3.18)$$

$\hbar\omega^{n,\mathbf{q}}$  are the eigenenergies of the corresponding band and quasi-momentum. The reciprocal lattice vectors are expressed as  $\mathbf{K} = n\mathbf{G}_1 + m\mathbf{G}_2$ . In this form it is easy to calculate the eigenenergies numerically and thereby the band structure of the lattice. The band structure of a shallow and a deep lattice is depicted in Fig. 3.2. For a deep lattice the band structure becomes similar to the energy spectrum of a harmonic oscillator with its equidistant energy bands. In the triangular lattice these almost equidistant bundles of energybands are not fully degenerate as in the harmonic oscillator.

The next step towards calculating the coupling between these bundles are to obtain the Wannier functions. Therefore first the Bloch functions have to be calculated. This is also relatively easy done by calculating the eigenstates  $c_{\mathbf{K}}^{(n,\mathbf{q})}$  to the corresponding eigenvalues and inserting them in Eq. 3.15. The Wannier functions can be computed from these as

$$w_n(\mathbf{r} - \mathbf{R}) = \frac{1}{\sqrt{N}} \sum_{\mathbf{q}} u_{n,\mathbf{q}}(\mathbf{r}) \exp(i\mathbf{k}(\mathbf{r} - \mathbf{R})). \quad (3.19)$$

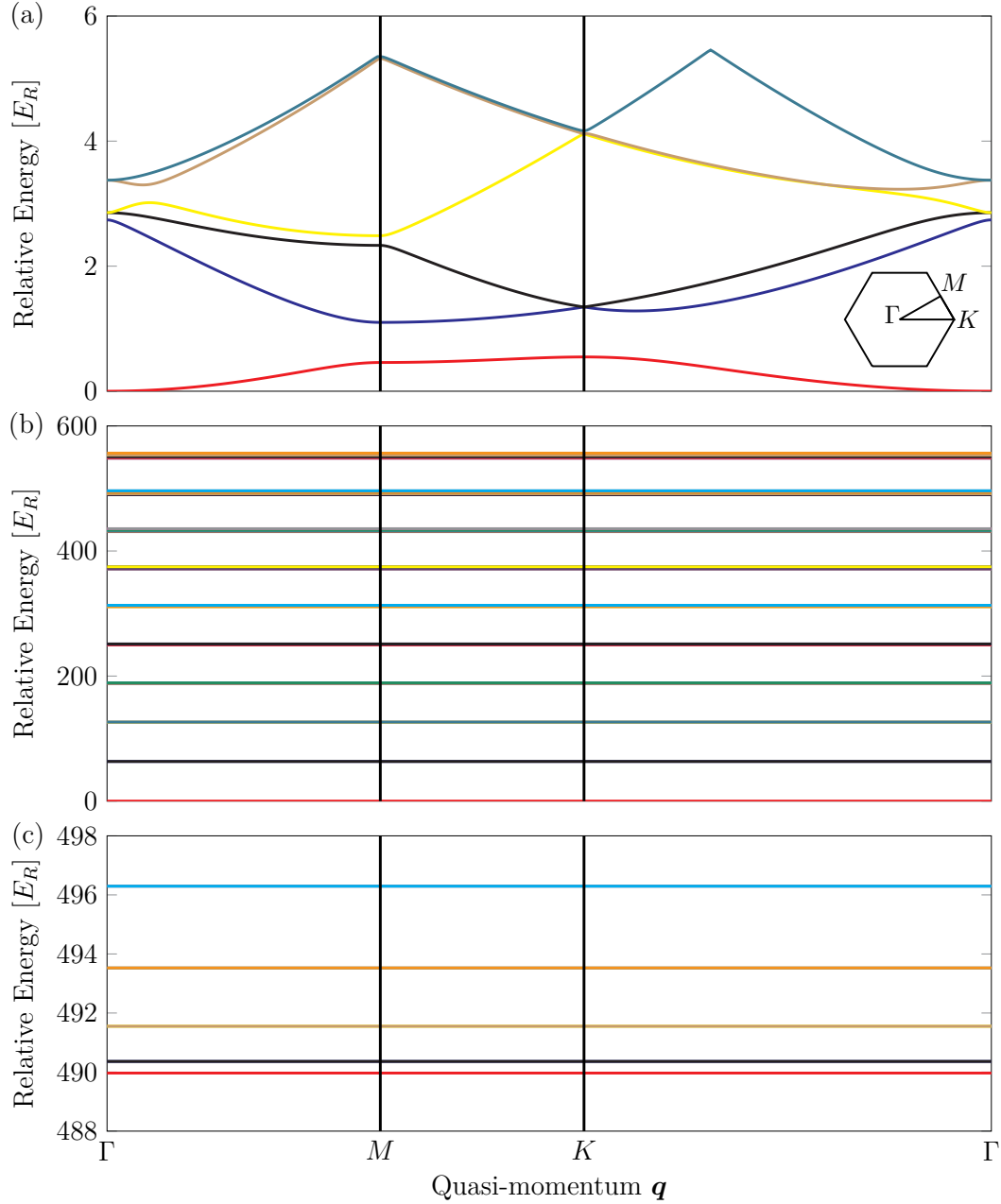


**Fig. 3.2:** Calculated band structure for a triangular lattice. In (a) the band structure of the first 6 bands for a shallow lattice with a trap depth of  $1E_R$  is shown. (b) and (c) both show the band structure for a lattice with a potential of  $2059E_R$ . (b) shows the lowest 55 bands which seem bundled to 10 bands with approximately equidistant energy gaps between them. (c) is a magnified view on the ninth bundle from the bottom in (b). It seems as if the bundle consists of five bands, but they are nine in total as the lower four lines consist of two overlapped bands each. For higher bundles the energy gap slowly decreases. The gap between the lowest and the next highest bundle is  $63.4E_R$ . For the gap between the ninth and tenth bundle it decreased to  $58.5E_R$ . The  $\Gamma$ ,  $M$  and  $K$  point positions in the first Brillouin zone are illustrated in (a).

However, the Bloch functions are only determined up to a global phase. While the choice of the phase is irrelevant for the Bloch state and its properties, the choice of the phases does strongly effect the Wannier functions. For a inconvenient choice of phases the Wannier function does not become localized. The desired kind of

Wannier functions is the so called maximally-localized. Until now it could only be proven that there is exactly one Wannier function that is maximally-localized [49] in one dimensional lattices. But there are various efforts to numerically calculate maximally-localized Wannier functions [50–53]. As this goes far beyond what is required, this will not be further discussed. In order to continue, the Wannier functions were calculated by using a MATLAB code presented in [54]. The obtained Wannier functions for the first and second band are shown in Fig. 3.3. The MATLAB program used to calculate the Wannier functions tries to obtain the maximally-localized Wannier function by minimizing its spread. During this process it can happen that the algorithm gets stuck in a local minimum. As the authors of the program state they had more success to avoid landing in a local minimum with degenerate bands by randomly picking a the Bloch state of one of the degenerate band as they are equally valid solutions. Due to this process the Wannier functions may be rotated arbitrary.

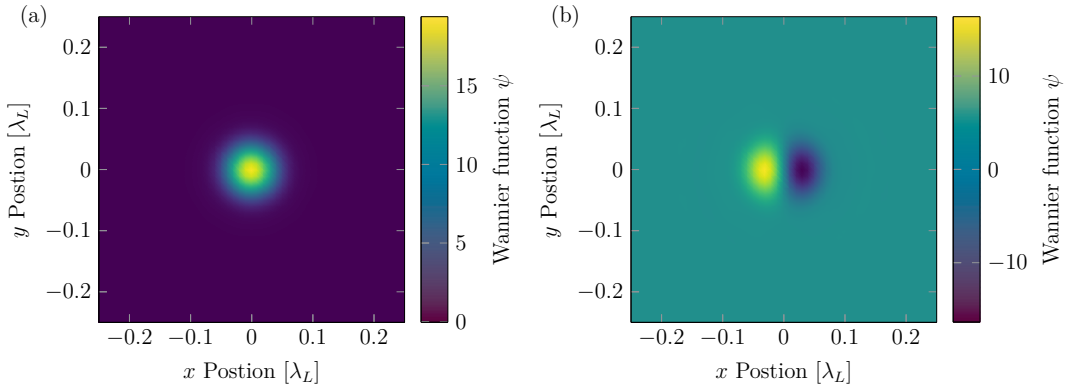


**Fig. 3.3:** Wannier functions of a triangular lattice with a trap depth of  $2059E_R$ . A total of  $41 \times 41$  lattice sites were considered. (a) and (b) show the first and second bands Wannier functions of a triangular lattice respectively. The wave function of the second band had to be rotated in order to set the parity axis along the  $y$ -axis. The position is given in units of the laser wavelength.

### 3.3 Coupling between Sidebands

With obtaining the Wannier functions, the coupling between the first and second band can be calculated. According to [55] the coupling term for two bands with indices  $n$  and  $m$  is given by

$$M = \langle n | \exp(i\mathbf{k}\mathbf{r}) | m \rangle. \quad (3.20)$$

In the case of the harmonic oscillator, for neighboring bands the coupling becomes zero with  $|\mathbf{k}| = 0$  as one of the wave functions has a positive and the other a negative parity with respect to the parity axis. The coupling becomes also zero if

the projected momentum is aligned along the parity axis. In the case of the Wannier functions in Fig. 3.3 the  $\mathbf{y}$ -axis is the parity axis. The wave function of the second band has negative parity as it is antisymmetric with respect to reflection at the parity axis. But with a momentum perpendicular to the parity axis, along  $\mathbf{x}$ , the parity is broken and the coupling becomes nonzero. In the so called Lamb-Dicke regime this coupling can be approximated. Since only the momentum component parallel to the parity axis is of relevance, the coupling can be written as

$$M = \langle n | \exp(ik_x x) | m \rangle. \quad (3.21)$$

For a harmonic oscillator the position operator can be expressed in terms of the ladder operators as

$$x = x_0(\hat{a} + \hat{a}^\dagger). \quad (3.22)$$

$x_0$  is the spread of the harmonic oscillator ground state

$$x_0 = \sqrt{\frac{\hbar}{2m\omega_x}}, \quad (3.23)$$

with  $\omega_x$  the trap frequency along the  $\mathbf{x}$ -axis. The Lamb-Dicke parameter is now defined as

$$\eta = k_x x_0 \quad (3.24)$$

and a system is considered in the Lamb-Dicke regime if  $\eta^2 \ll 1$ . As elaborated in [55, 56] the resulting coupling using Eq. 3.22 and Eq. 3.24 can be given by

$$M = \exp\left(-\frac{\eta^2}{2}\right) \sqrt{\frac{n!}{m!}} \eta^{m-n} L_n^{m-n}(\eta^2), \quad (3.25)$$

for the case of  $m$  being larger than  $n$ .  $L_n(x)$  are the Laguerre polynomials. In the Lamb-Dicke regime the higher order terms,  $m - n \geq 2$ , become sufficiently small and can be neglected and the coupling can be approximated by

$$M = \eta\sqrt{n} \quad \text{for } n \rightarrow n - 1, \quad (3.26a)$$

$$M = 1 - \frac{2n+1}{2}\eta^2 \quad \text{for } n \rightarrow n \text{ and} \quad (3.26b)$$

$$M = \eta\sqrt{n+1} \quad \text{for } n \rightarrow n + 1. \quad (3.26c)$$

In the case of optical transitions the momentum projection is given by the photon recoil momentum and therefore the Lamb-Dicke parameter can also be described by  $\eta = \sqrt{\frac{E_R}{\hbar\omega_x}}$ , using the recoil energy  $E_R$ . The total coupling for optical transitions incorporating sidebands is given by the product of the coupling between vibrational

states and the optical coupling. This can be expressed as the effective Rabi frequency

$$\Omega_{eff} = M\Omega_0. \quad (3.27)$$

As the vibrational states differ by a certain frequency, transitions changing the vibrational level appear as sidebands in a spectrum. Only considering the vibrational levels a reduction of the sideband is associated with the loss of energy and thereby can be quantified by a negative frequency. Therefore it can be called the red sideband. However, depending on the internal transition accompanying the sideband transition the vibrational level lowering transition can be the one with the larger frequency compared to the bare internal transition and would therefore be called the blue sideband. Since Raman-sideband cooling exploits these sideband transitions in order to cool and to avoid possible confusion vibrational level lowering transitions associated with the cooling sideband (CSB) while increasing transitions are associated with the heating sideband (HSB). In order to see how well the Lamb-Dicke

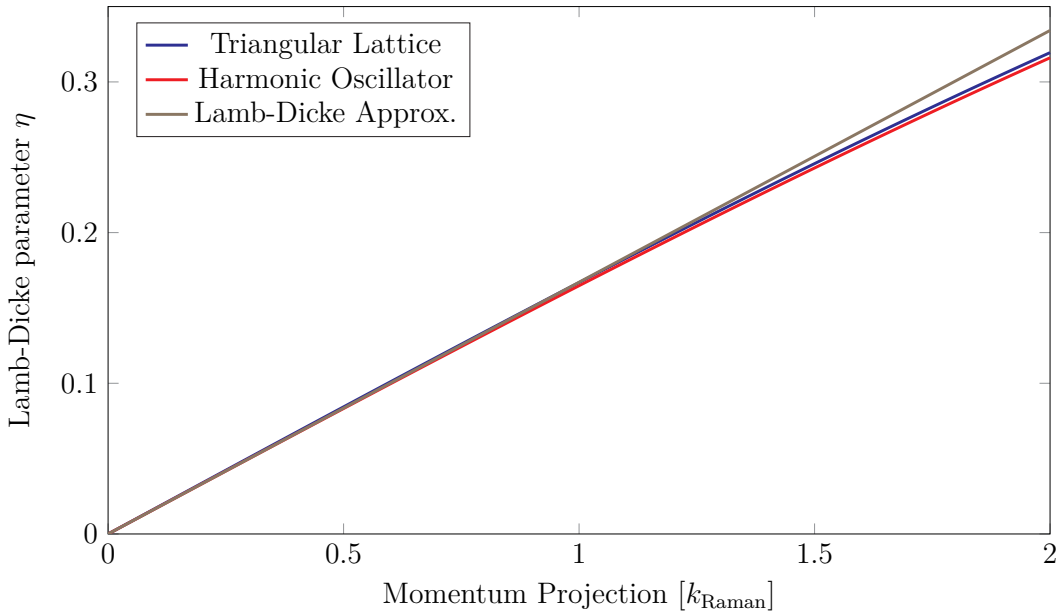


**Fig. 3.4:** Vibrational level coupling. Depicted are the vibrational couplings calculated numerically for the triangular lattice with Wannier functions, also calculated numerically for the harmonic oscillator with the spatial eigenfunctions and estimated by the Lamb-Dicke approximation. As this are the couplings between the ground state and the first excited state, the calculated coupling equals the Lamb-Dicke parameter. The trapping potential used is  $2059E_R$ . As the coupling parameter for the triangular lattice only differs by 1.1% from the harmonic oscillator, they are almost equally good described by the Lamb-Dicke parameter.

approximation works for a deep triangular lattice, the coupling will be calculated numerically by using the Wannier functions for the ground state and the first excited state and it will be compared to the Lamb-Dicke parameter and a numerical calculation for a two dimensional harmonic oscillator. With Eq. 3.11 there is already a relation given for the lattice depth and a harmonic approximation. But looking at

the triangular lattice, it can be seen that the barrier between nearest neighbors does not correspond to the calculated value with Eq. 3.11. Precisely it is given by 8/9 of that value. With a lower trap frequency lower energies are associated, wherefore it might be more reasonable to calculate the harmonic oscillator eigenfunctions for a trap frequency corresponding to 8/9 of the triangular lattice depth. The results for the calculated Lamb-Dicke parameters under these conditions are shown in Fig. 3.4. The coupling for the triangular lattice matches that of the harmonic oscillator very well with a difference of 1.1 % at a trapping potential of  $2059E_R$ . Therefore it is appropriate to estimate the vibrational coupling in a triangular lattice in the Lamb-Dicke regime with the Lamb-Dicke parameter.

### 3.4 Conclusion

By calculating the trapping potential for a planar three beam configuration with  $120^\circ$  between each other and by calculating the harmonic approximation of a potential minimum, a relation between the trap depth and the trap frequency could be derived. This was used to calculate the trap depth of  $2059E_R$  with the trap frequency of 130 kHz obtained by modulation spectroscopy.

With the help of the Bloch theorem it was possible to numerically calculate the band structure of the triangular lattice and to show that for large trap depth the energy spectrum become similar to that of a harmonic oscillator.

Subsequently, the coupling between vibrational states in an harmonic oscillator was approximated for the Lamb-Dicke regime. These coupling terms can be used to calculate the Rabi frequency for sideband transitions. Finally, the coupling approximated by the Lamb-Dicke approximation was compared to the couplings computed numerically for the harmonic oscillator and the triangular lattice to find that both are equally well approximated.



# Chapter 4

## Raman-Sideband Cooling

This chapter focuses on Raman-sideband cooling. Starting at the transition scheme that was developed and the thoughts that lead to this specific scheme it will continue with a simulation of mentioned scheme by numerically calculating the time evolution of the density matrix describing the system by using a quantum master equation. Furthermore, the experimental setup necessary to apply this Raman-sideband cooling scheme will be presented as well as the troubles encountered during the first operations of the setup. Finally the successful application of Raman-sideband cooling will be demonstrated.

### 4.1 Transition Scheme

For a Raman sideband cooling scheme the the most crucial parameters are the Rabi frequency of the Raman transition and the transition amplitude. They are determined by the chosen transition path and the intensities of the lasers driving the Raman transition. The transition path is important insofar it determines the geometrical coupling factors  $|\mathbf{G}_{F1} \cdot \mathbf{G}_{F2}|$ . According to [44], for  $F$  changing transitions these geometrical terms can be expressed as

$$|\mathbf{G}_{F1} \cdot \mathbf{G}_{F2}| = \frac{|A(J')|}{3(2J' + 1)} \sqrt{\left(I + \frac{1}{2}\right)^2 - m_F^2} \quad \text{and} \quad (4.1a)$$

$$|\mathbf{G}_{F1} \cdot \mathbf{G}_{F2}| = \frac{|A(J')|}{3(2J' + 1)} \sqrt{T \left(I + \frac{1}{2} - m_F\right)}, \quad \text{with} \quad (4.1b)$$

$$A(J') = \begin{cases} -2 & \text{for } D_1 \text{ transitions} \\ -1 & \text{for } D_2 \text{ transitions} \end{cases}. \quad (4.1c)$$

$I$  is the nuclear spin and  $T(n)$  is the  $n$ th triangular number. Eq. 4.1a is applied for transitions with  $q_1 = 1$  and  $q_2 = 1$ , whereas Eq. 4.1b applies for transitions with  $q_1 = 0$  and  $q_2 = 1$ . By evaluating these equations, it shows that transitions

coupling the, absolute wise, highest  $m_F$  states are the strongest regarding the geometrical coupling factors. Moreover  $F$  changing transitions are stronger than  $F$  keeping ones. In the case of  $^{87}\text{Rb}$  a Raman coupling between  $|2, \pm 2\rangle$  and  $|1, \pm 1\rangle$  is 1.73 times stronger than between  $|2, \pm 2\rangle$  and  $|2, \pm 1\rangle$ . On the other hand the resonance frequency of the first mentioned transition is three times more sensitive to the magnetic field than the latter one. Even though the  $A(J')$  is twice as large for  $D_1$  transitions with  $^{87}\text{Rb}$ , the overall difference between  $D_1$  and  $D_2$  transitions is not, since the reduced dipole coupling  $\langle \alpha', J' || \mathbf{r} || \alpha, J \rangle$  is different for the two transitions. The ratio of the absolute square of the reduced dipole coupling for the  $D_1$  and  $D_2$  transition is only slightly bigger than 0.5. From the perspective of transition strength it makes no difference whether the  $D_1$  or  $D_2$  transition is taken. However, it is more convenient to take the  $D_1$  transition as the basis for the Raman transition, considering that the Raman light has to have a significantly higher intensity than the pumping light for the fluorescence imaging, which in our case uses the  $D_2$  line and thus is easily separated from the Raman light by a simple filter. To maximize the amplitude of the Raman transition, according to Eq. 2.48, the differential light shift has to be minimized. In order to do this the relative intensity between the two Raman lasers has to be adjusted such that the light shifts get equal. Since only the intensity ratio is important for the amplitude, the intensities can just be scaled to achieve higher Rabi frequency.

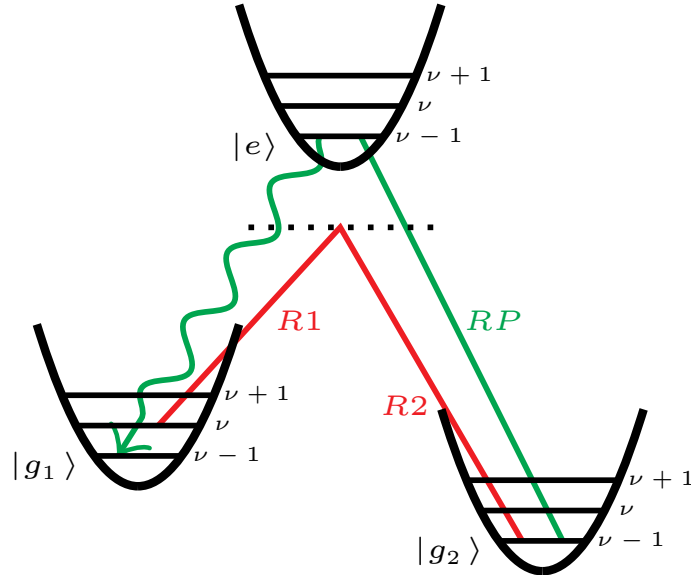


**Fig. 4.1:** Simplified vibrational transition scheme for continuous Raman sideband cooling. The Raman beams, R1 and R2, introduce a coupling between two neighboring vibrational states of different internal states  $|g_1, \nu\rangle$  and  $|g_2, \nu - 1\rangle$ . A resonant laser (RP) excites the atom so that it can decay back into the initial internal state while keeping the lowered vibration state via  $|e, \nu - 1\rangle$ . Even though excitation and spontaneous emission also couples different vibrational states the majority of atoms keeps the vibrational state during these processes.

The Raman transition to be implemented will couple two magnetic hyperfine ground states and simultaneously two neighboring vibrational states. Since the Raman transition is a coherent process, the atoms will just oscillate between these two vibrational levels and no cooling will have taken place. To continuously lower the vibrational state, resonant optical transitions have to be applied, which can also cause a change of the vibrational state by  $\pm 1$  but mainly keeps it constant as does the subsequent spontaneous emission. If this process begins in the state  $|F, m_F, \nu\rangle$ , the Raman coupling transitions the atoms into  $|F', m'_F, \nu - 1\rangle$ , after which the atoms are pumped back into  $|F, m_F, \nu - 1\rangle$ , losing one vibrational quantum. This process is shown in Fig. 4.1.

One scheme that would be well suited for such an cycle, taking the previous considerations into account, is a  $\pi^0 - \sigma^-$  transition between  $5S_{1/2} |2, -2\rangle$  and  $5S_{1/2} |1, -1\rangle$  and subsequent pumping to  $5S_{1/2} |2, -2\rangle$  by  $\sigma^-$  polarized light over  $5P_{3/2} |2, -2\rangle$ . Since the  $5P_{3/2} |2, -2\rangle$  state, besides  $5S_{1/2} |2, -2\rangle$  and  $5S_{1/2} |1, -1\rangle$ , can decay into  $5S_{1/2} |2, -1\rangle$ , a second pumping beam coupling this state to the same excited state is necessary in order to keep all atoms in the cycle. This second pumping beam has to be sufficiently detuned in order to avoid coherent population trapping as shown in 2.3.3. With the prospect of fluorescence imaging, a third beam will be needed, which couples  $5S_{1/2} |2, -2\rangle$  and  $5P_{3/2} |3, -3\rangle$ , which is a closed transition, so that fluorescence light from the vibrational ground state atoms in  $5S_{1/2} |2, -2\rangle$  can be collected, which is a dark state for the previously mentioned cooling cycle.

This scheme would have two requirements for the Raman beams. One would be, that the  $\pi^0$  beam is aligned perpendicular to the quantization axis  $\hat{e}_z$  and the other would be that the  $\sigma^\pm$  beam is aligned along the quantization axis. Those requirements would restrict the range of possible momenta projected onto the atoms. It is even more restricted by the optical access to the atoms in the glass cell. A transition scheme with a  $\pi^0 - \pi^\pm$  coupling has less restrictions since the  $\pi^\pm$  only has to be aligned perpendicular to  $\hat{e}_x$  or  $\hat{e}_y$ . This means that only half of the light in the  $\pi^\pm$  beam would contribute to the desired transition and also that a coupling between  $5S_{1/2} |1, -1\rangle$  and  $5S_{1/2} |2, 0\rangle$  is existent. Anyhow, this new transition causes the differential light shift to become zero and thereby allowing any intensity ratio between the two Raman beams without any negative impact. For Rabi frequencies in the range of about 20 kHz the atomic population taking part in this undesired  $\sigma^+$ -Raman path can be neglected because even for an external magnetic field of 1 G the detuning for this transition is 1.4 MHz and according to Eq. 2.48 the transition amplitude becomes about 0.2‰. Including the vibrational coupling it would be even smaller. A schematic showing which internal states are coupled by which lasers is illustrated in Fig. 4.2. The Raman transition works for the not mentioned ground states as well, but as for the  $\sigma^+$ -Raman path the large detunings compared to the Rabi frequencies only establish weak couplings. Furthermore, all atoms finding their

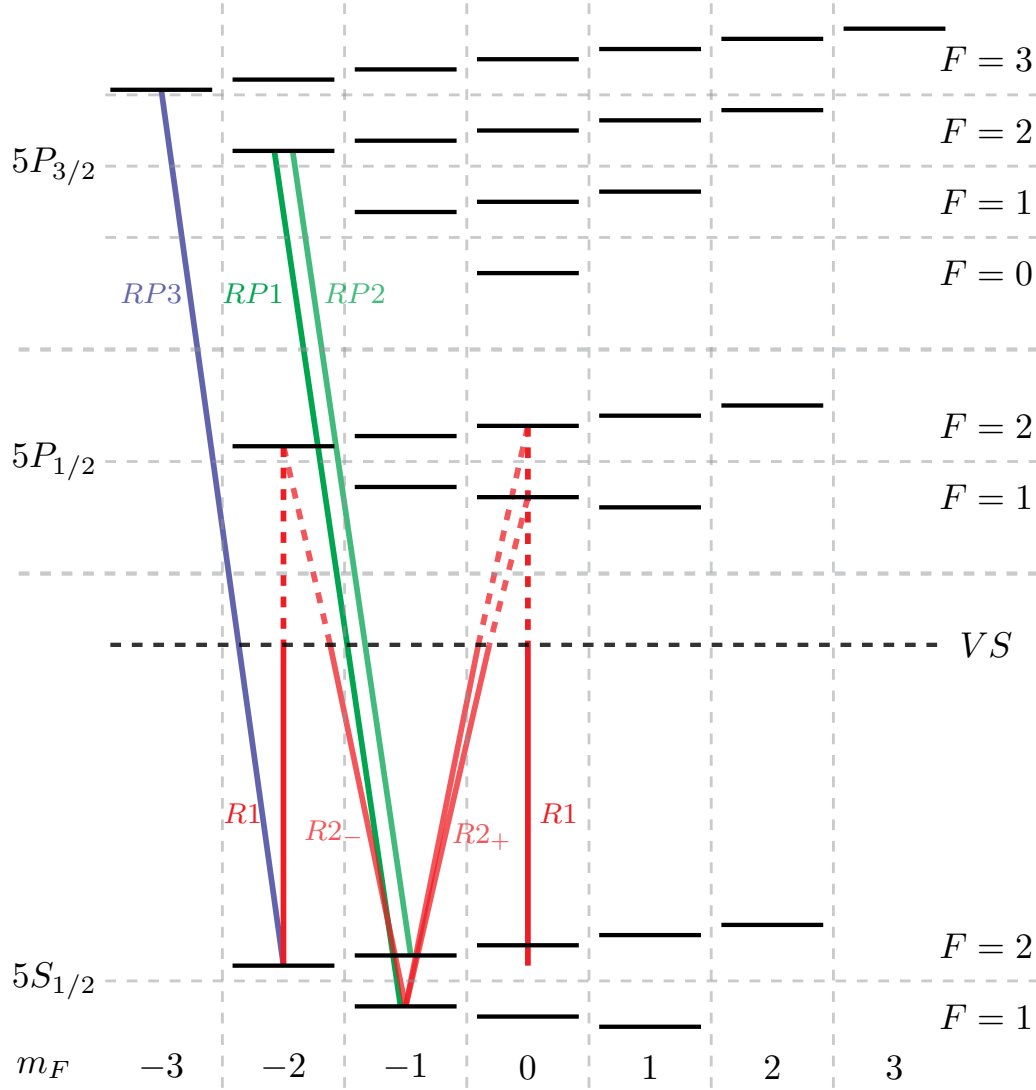


**Fig. 4.2:** Internal transition scheme for continuous Raman sideband cooling. The illustration shows the magnetic hyperfine sublevels of the  $5S_{1/2}$ ,  $5P_{1/2}$  and  $5P_{3/2}$  states of  $^{87}\text{Rb}$  and the transitions supposed to be driven by the lasers between the respective energy levels. It is indicated, that Raman 2, indicated by  $R2_{(\pm)}$ , drives  $\sigma_+$  and  $\sigma_-$  transitions since its polarization is linear but perpendicular with respect to the quantization axis. This leads to the driving of two different Raman transitions with Raman beam 1 (R1) and R2 between  $5S_{1/2}$  states, connecting the  $|F = 1, m_F = -1\rangle$  with  $|F = 2, m_F = -2\rangle$  and  $|F = 2, m_F = 0\rangle$ . The Zeeman shift can be adjusted so that one transition path is resonant and the other, in this case  $|F = 2, m_F = 0\rangle$ , is detuned and thereby suppressed. Due to the decay of the  $5P_{3/2}$  states, the Imaging Repump (RP1) and Raman Repump 2 (RP2) beams pump the atoms back into  $|F = 2, m_F = -2\rangle$  by driving a  $\sigma_-$  transition to  $|F' = 2, m'_F = -2\rangle$ . Raman Repump 3 (RP3) drives a closed transition between the  $5S_{1/2} |F = 2, m_F = -2\rangle$  and  $5P_{3/2} |F' = 3, m'_F = -3\rangle$  states and can be used to induce fluorescence of the atoms in the vibrational ground state. Not to scale.

way out of the relevant ground states for the presented cooling scheme will quickly be pumped back by the pumping beams.

## 4.2 Lindblad Equation

For closed two-level transitions, which do not include spontaneous emission, the evolution of the population can be calculated by finding a solution for the differential equations given by the Schrödinger equation as demonstrated in 2.1.2. Solutions for transitions with more coupled states can be difficult to find and still do not account for spontaneous emissions. Therefore, it may be more practical to evaluate the transition scheme under investigation numerically. This can be done by using a quantum master equation like the Lindblad equation.

Spontaneous decay processes introduce decoherence to the dynamics of the system and thereby cause a potentially pure state to become a state mixture. These mixtures of states can be described by a density matrix which is generally given by

$$\rho(t) = \sum_{i,j} c_i c_j^* |\psi_i\rangle \langle \psi_j|. \quad (4.2)$$

The off-diagonal terms of the density matrix are associated with the coherence between the basis states. For the Raman sideband cooling scheme in 4.1 four internal and  $n$  external, or vibrational, states are considered. Accordingly the density matrix is a  $(4 \times n) \times (4 \times n)$ -matrix.

As for example explained in [39] the equation of motion, or the Liouville–von Neumann equation, for the density matrix of a closed system described by the Hamiltonian  $\mathcal{H}$  can be derived from the Schrödinger equation to be

$$\dot{\rho}(t) = -\frac{i}{\hbar} [\mathcal{H}, \rho]. \quad (4.3)$$

To include spontaneous emission the Liouville–von Neumann equation can be extended to be the Gorini–Kossakowski–Sudarshan–Lindblad equation, or short Lindblad equation, which looks like

$$\dot{\rho}(t) = -\frac{i}{\hbar} [\mathcal{H}, \rho] + \mathcal{L}(\rho). \quad (4.4)$$

The second term is referred to as the Lindblad superoperator. It can be expressed as

$$\mathcal{L}(\rho) = \sum_{i,j} \Gamma_{i,j} \left( L_i \rho L_j^\dagger - \frac{1}{2} \{ L_j^\dagger L_i, \rho \} \right). \quad (4.5)$$

The expression  $\{A, B\}$  describes the anticommutator relation  $\{A, B\} = AB + BA$ . The operators  $L_i$  have the form  $L_i = |F_i, m_{F,i}, \nu_i\rangle \langle F'_i, m'_{F,i}, \nu'_i|$  and  $\Gamma_{i,j}$  is the corresponding decay rate for this path. For the optical transitions that will be addressed later on only the decay rates  $\Gamma_{i,j}$  for transitions from an excited state to a ground state and for  $i = j$  are not zero and contribute. Moreover, in the Lamb-Dicke regime

only those transition paths with  $\nu_i - \nu'_i = 0, \pm 1$  will be considered.

The decay rates for the internal atomic states can be calculated as can be done with Eq. 2.33. The spontaneous emission, besides coupling the internal electronic state of the atom, induces a motional coupling as well. As described in 3.3 in the Lamb-Dicke regime this couples neighboring vibrational levels. For the decay rate is proportional to the square of the coupling matrix element, the decay rates for the same internal transition path are modified by

$$\Gamma_{I,\nu \rightarrow \nu-1} = \Gamma_I \cdot \eta^2 \nu \quad (4.6a)$$

$$\Gamma_{I,\nu \rightarrow \nu} = \Gamma_I \cdot (1 - \eta^2(2\nu + 1)) \quad (4.6b)$$

$$\Gamma_{I,\nu \rightarrow \nu+1} = \Gamma_I \cdot \eta^2(\nu + 1), \quad (4.6c)$$

where  $\Gamma_I$  is the decay rate for the respective internal transition and  $\nu$  is an integer indicating the vibrational state. Here the Lamb-Dicke parameter  $\eta$  technically has to be modified because of its dependence on the momentum transfer from the photon to the atom. Since the spontaneous emission is not directed but isotropic, an average Lamb-Dicke parameter has to be obtained for the spontaneous emission processes by integrating and averaging it over a momentum spheres surface with a radius of the recoil momentum  $k_R$  of the spontaneously emitted photon with

$$\langle \eta \rangle = \frac{1}{4\pi k_R^2} \int_{|\mathbf{k}|=k_R} \langle \nu' | e^{i\mathbf{k}\hat{\mathbf{r}}} | \nu \rangle d\mathbf{k}. \quad (4.7)$$

For practical reasons, simulations featured in this thesis are calculated with the maximal value for  $\eta$ . Considering Eq. 4.6, this favors heating processes due to spontaneous emission and should lead to a worse performance than in the ideal case.

The Hamiltonian for the proposed Raman sideband cooling scheme in 4.1 can be constructed from the time-dependent Hamiltonians for the two level problem and the time-dependent reduced Hamiltonian for the Raman transition. The time-dependence is necessary since the different laser do not necessarily have the same detuning and therefore have different rotating frames. It can be written as

$$\mathcal{H} = \frac{\hbar}{2} \begin{pmatrix} 2\Omega_1^{\text{AC}} \mathcal{C}_{1,n} & 0 & \Omega_R e^{-i\delta_R t} \mathcal{C}_{R,n} & 0 \\ 0 & 0 & 0 & \Omega_{\text{RP1}}^* e^{-i\delta_1 t} \mathcal{C}_{\text{RP1},n} \\ \Omega_R^* e^{i\delta_R t} \mathcal{C}_{R,n}^\dagger & 0 & 2\Omega_2^{\text{AC}} \mathcal{C}_{2,n} & \Omega_{\text{RP2}}^* e^{-i\delta_2 t} \mathcal{C}_{\text{RP2},n} \\ 0 & \Omega_{\text{RP1}}^* e^{i\delta_1 t} \mathcal{C}_{\text{RP1},n}^\dagger & \Omega_{\text{RP2}}^* e^{i\delta_2 t} \mathcal{C}_{\text{RP2},n}^\dagger & 0 \end{pmatrix}. \quad (4.8)$$

$\Omega_{1/2}^{\text{AC}}$  are the effective light shifts of the Raman transition given by Eq. 2.47 and  $\Omega_R$  is the Rabi frequency for this Raman transition given by Eq. 2.46.  $\Omega_{\text{RP1}}$  and  $\Omega_{\text{RP2}}$  are the Rabi frequencies for the RP1 and RP2 beams respectively.  $\delta_R$ ,  $\delta_1$  and  $\delta_2$  are the corresponding detunings for the Raman transition, the RP1 and RP2 beams.

The  $\mathcal{C}_{m,n}$  are  $n \times n$ -matrices providing the coupling between the vibrational states. For the Raman Repumper the  $\mathcal{C}_{\text{RP}1/2,n}$  are filled according to Eq. 3.26.  $\mathcal{C}_{\text{R},n}$  only contains the coupling element to for the resonant vibrational state.  $\mathcal{C}_{1/2,n}$  only have ones on the diagonal except for the first or the last entry respectively, which are zero, since the vibrational ground state of the first Raman coupled internal ground state and the highest vibrational state of the second Raman coupled internal ground state are dark states for the Raman transition.

To include the coupling of RP3 for the fluorescence imaging, this Hamiltonian can be expanded easily to a  $(5 \times n) \times (5 \times n)$ -matrix with a coupling between the additional internal state  $5P_{3/2} |3, -3\rangle$  and the initial ground state  $5S_{1/2} |2, -2\rangle$ .

### 4.3 Simulated Population Evolution

By utilizing an algorithm for numerical calculations of differential equations, it is possible to simulate the time evolution of the density matrix governed by a Hamiltonian similar to the one described in Eq. 4.8 and the Lindblad equation Eq. 4.4. A popular algorithms for this task are the Runge-Kutta algorithm and its variations. Such derivative algorithms are implemented in **MATLAB**, as for example in form of the `ode45` function [57]. The `ode45` function was used for the computation of all time evolution plots presented in this thesis, including the ones already shown.

Depending on the number  $N$  of vibrational levels that are included in the calculation, visualizing all states separately can look confusing, since in the case of the transition scheme for fluorescence imaging shown in Fig. 4.2 there are  $5 \times N$  separate states. So it makes more sense to reduce the number of states in a meaningful way. A practical reduction is to calculate a mean vibrational level. In order to do this the vibrational states of the initial internal state  $5S_{1/2} |2, -2\rangle$  act as a reference. As mentioned before the states  $5S_{1/2} |2, -2, \nu\rangle$  and  $5S_{1/2} |1, -1, \nu - 1\rangle$  are coupled by the coherent Raman transition and thus will be assigned to the same vibrational number  $\nu$ . The vibrational states of the internal states  $5S_{1/2} |2, -1\rangle$ ,  $5P_{3/2} |2, -2\rangle$  and  $5P_{3/2} |3, -3\rangle$  are not reassigned. By weighting the population of each vibrational state with its vibrational number  $\nu$  the mean vibrational number can than be calculated as the sum over the weighted populations. Another crucial information about this process is the total number of photons scattered at a certain point in time, since the purpose of the whole setup is to collect enough photons per atom to determine the population of the occupied lattice sites with high certainty. To calculate the number of photons scattered  $N_{SP}$  between  $t_0$  and  $t_1$  the population probability  $\rho_e$  of the excited states have to be integrated and multiplied with the

decay rate  $\Gamma_e$  of the respective state like

$$N_{SP} = \int_{t_0}^{t_1} (\Gamma_{e1}\rho_{e1}(t) + \Gamma_{e2}\rho_{e2}(t)) dt. \quad (4.9)$$

In order to calculate such kind of model, the number of vibrational levels under consideration has to be limited. For the calculation presented in the following the vibrational levels were truncated to  $10 + 1$ . Ten vibrational levels are incorporated as described in 4.2 and one additional vibrational level is used to estimate the loss of atoms. Atoms can be excited into this eleventh vibrational level but cannot escape it, removing them from further transitions. The population in the eleventh band is neither considered for calculating the mean vibrational level, nor do they scatter any photons. The number of ten main vibrational levels was chosen as a compromise between comprehensiveness and computational time. The computational model works with an harmonic approximation, meaning the energy levels of neighboring vibrational levels are assumed to be equidistant, even though for a deep triangular lattice the energy gaps become slightly narrower for increasing band numbers.

Using the harmonic approximation and the measured trap frequency of 130 kHz from 3.1, the vibrational ground state and the first excited state differ by about  $64.2E_R$ . As mentioned this is equivalent to a trap depth of  $1830E_R$ . For a triangular lattice with this trap depth the gap from the eighth to the ninth excited state amounts to  $59.4E_R$ , which correspond to a difference of 9.8 kHz compared to the separation of the ground state to the first excited state. According to Eq. 2.49 a detuning of 9.8 kHz from resonance at a bare Rabi frequency of  $\Omega_R = 54$  kHz would lead to an effective Rabi frequency of  $\tilde{\Omega}_R = 54.9$  kHz. This change of the Rabi frequency of about 1.6 % and the accompanying transition amplitude change of about 3.2 % will be neglected.

The parameters chosen for the computation are summarized in Tab. 4.1. The parameters  $\Delta$  and  $\delta_R$  are the detunings of the Raman transition as introduced in 2.3.2.  $\delta_{1,2,3}$  are the detunings of the respective pumping beams. Only the repumper 2 has a detuning different from zero to avoid coherent population trapping as explained in 4.1. The  $\Omega_{R,1,2,3}$  are the respective bare Rabi frequencies of the Raman transition and the repumpers. Similar the  $\eta_{R,1,2,3,Spon}$  are the estimated Lamb-Dicke parameters for the Raman transition, the repumpers and the spontaneous emission.

The computation result is shown in Fig. 2.2. Due to the detuning of the repumper

Parameter	Value
$\Delta$	100 GHz
$\delta_R$	0 Hz
$\delta_{1,3}$	0 Hz
$\delta_2$	2 MHz
$\Omega_R$	54 kHz
$\Omega_1$	149 kHz
$\Omega_2$	86 kHz
$\Omega_3$	47 kHz
$\eta_R$	0.21
$\eta_{1,2,3,Spon}$	0.17

**Tab. 4.1:** Simulated population evolution parameters.



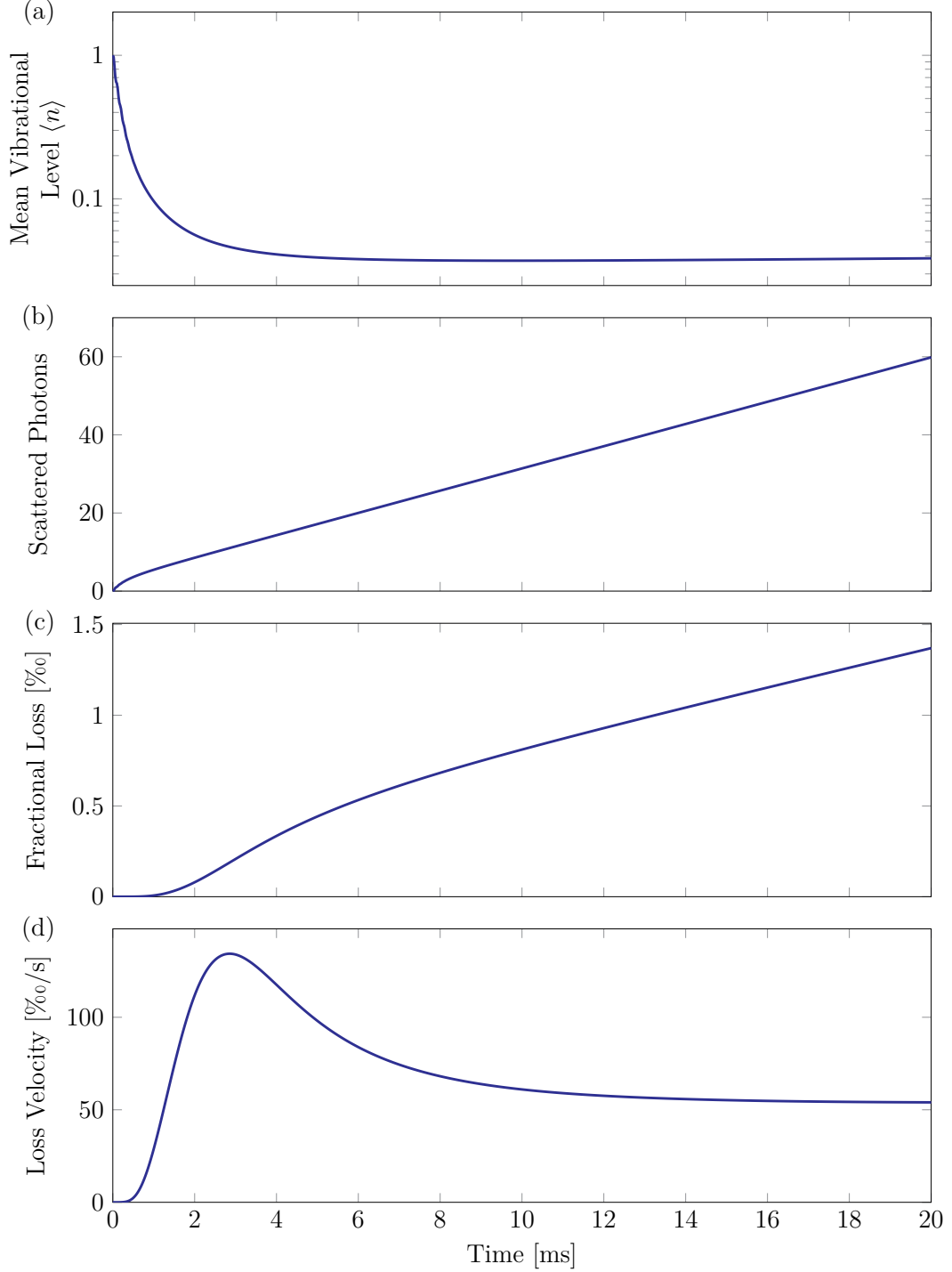


**Fig. 4.3:** Transition scheme time evolution. The plots show the evolution of the mean vibrational level (a), the mean number of scattered photons (b), the loss permille (c) and the loss velocity permille using the computational model and parameters described in 4.3. The mean vibrational number after 20 ms is 0.04. Judging from the asymptotic like behavior of the mean vibrational level and the loss velocity, the system went into relatively slow changing state, with almost constant mean vibrational level, photon scattering and atom loss. Therefore and due to the high calculation time of this model, the scattered photons and the loss for longer periods will be estimated by assuming a linear growth after the computed 20 ms. After 600 ms accordingly an average of 1738 photons per atom are scattered and 3.3% of the atoms are lost.

2 the calculated values become complex and to account for the fast changes caused by the high detuning the time steps for the computation have to be chosen smaller to avoid too strong deviation. These two reasons make this model difficult to simulate and the calculation of time scales of interest can take several hours. The particular simulation shown in Fig. 2.2 took twenty hours of calculation time. As this might change in the future due to more computational power or by using computing clusters, in the scope of this work it is unpractical to calculate longer time scales. However, for the parameters presented here, the simulation goes into a relatively slow changing state. Therefore, in order to estimate the in average scattered photons per atoms and the atom loss, the photon scattering and the atom loss are assumed to be constant. Under this assumption after a period of 600 ms an average of 1738 photons will be scattered per atom and 3.3 % of the atoms will be lost from the lattice. With an estimated total collection efficiency of 7 % for the quantum gas microscope imaging system this would correspond to 122 collected photons per atom. This number of photons is assumed to be sufficient for single site resolved imaging. For the total collection efficiency the solid angle covered by the objective, losses at optical components and the detection efficiency of the detector were taken into account. By fitting an exponential function to the mean vibrational level evolution a time constant of  $266 \mu\text{s}^{-1}$  is obtained. It should be mentioned that the simulation parameters were not optimized due to the high time consumption of one calculation. A suitable range of parameters was estimated by using models with less vibrational levels and shorter time periods. It is likely that the results can be improved by systematically optimizing the simulation parameters.

## 4.4 Experimental Setup

This section will present the optical setups and the electronics build and used during the period of this work. This includes the optical setup of the Raman laser system on the laser table, the offset lock system used to establish a stable frequency relation between the Raman lasers and the optical setup on the experiment table. Furthermore in a short experiment it is investigated if the experimental setup is suitable to drive Raman transitions.

### 4.4.1 Laser Setup

The Raman laser setup is installed on the laser table of the experiment and consists of two **Toptica DL Pro 780** diode lasers, the Raman 1 and Raman 2 lasers, operating with a relative frequency of about 6.8 GHz with respect to each other at a wavelength corresponding to the  $^{87}\text{Rb}$  D<sub>1</sub>-line of about 795 nm. Both lasers are controlled by the same **Toptica DLC pro** digital laser controller. By using a half-wave plate (HWP)

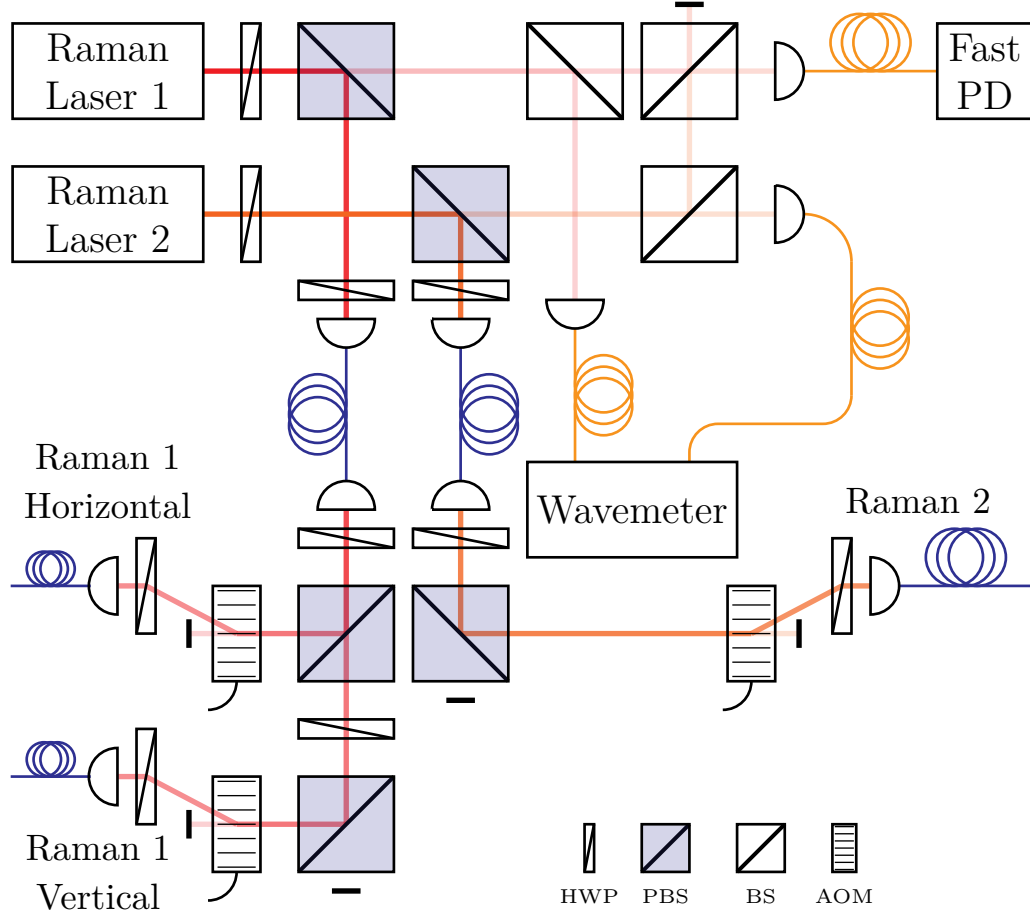


**Fig. 4.4:** Simplified Raman laser setup scheme. Two lasers, Raman Laser 1 and 2, are used as a source for the Raman beams. The Raman laser 1 is branched into two beams labeled Raman 1 Horizontal and Vertical as their wave vectors are either aligned in the horizontal triangular lattice plane or have a vertical component. Fractions of both Raman lasers 1 and 2 are divided into equal parts by 50:50-beamsplitters (BS). One splitted beam of each laser is interfered at a fast photo diode (PD) to pick up a beat signal, whose oscillation frequency corresponds to the frequency difference between the two lasers. Polarization-maintaining fibers are shown in blue. Yellow fibers are not polarization-maintaining. Mirrors and mechanical shutters are omitted.

and a polarizing beamsplitter (PBS) for each laser the polarization of the laser light can be cleaned and branched into two beams. The branching ration can be controlled by adjusting the angle of the HWP. A fraction of the laser light is used to monitor the wavelength at a wavemeter. Another fraction of both beams is interfered at a fiber coupled fast photo-diode. The used photo-diode is a **Electro-Optics Technology GaAs Pin Detector ET-4000F**. With a bandwidth of more than 12.5 GHz it is able to pick up the fast interference beat signal of about 6.8 GHz for the use of a offset lock system to precisely control the frequency difference between the two lasers. The main branch of each laser is routed through a HWP and a fiber coupler with an attached polarization maintaining fiber onto a neighboring area on the laser table. The polarization maintaining fiber maintains the polarization of the laser beam, as the name suggests. For this to work the orientation of the beam polarization has to be aligned correctly. This can be done by shining the output side of the fiber

onto a HWP and subsequent PBS and monitoring the change in power for one path after the PBS. If the polarization is not aligned correctly, heating or shaking the fiber should cause power fluctuations. For the correct alignment the HWP before the fiber has to be adjusted until no power fluctuation can be observed.

In the neighboring area the beams can again be branched into two by using a HWP and PBS, which is done for the Raman 1 laser. These two branches are called Raman 1 Horizontal and Raman 1 Vertical as the wave vector of the respective beams will either lie in the horizontal triangular lattice plane or it will also have a component in the vertical direction. After each of these PBS a Gooch & Housego AOM 3080-125 acousto-optic modulator (AOM) is installed and adjusted such that the power of the first diffraction order is maximized at a operation frequency of 80 MHz.

In the first diffraction order the laser frequency is given by the initial laser frequency plus the operation frequency of the AOM. With rise times in the order of 200 ns they can be used for the fast control of the frequency in a range of  $\pm 1$  MHz and fast on and off switching of the beam. The diffraction angle depends on both, the operation frequency of the AOM and the temperature of the crystal inside the AOM. While there is a radio frequency (RF) signal applied to the piezoelectric transducer in the AOM to generate sound waves inside the crystal, the crystal is heated up and thereby the diffraction angle changes until a thermal equilibrium is reached.

When the RF signal to the AOM is cut off for a longer period, the crystal cools down and the diffraction angle will be changed as soon as the RF signal comes back. This makes an AOM suboptimal as a switch for longer off-states. For this purpose fast mechanical shutters are installed after the AOMs. After this shutters there are another HWP and fiber coupler, which couples to an polarization maintaining fiber that guides the beams to the experiment table.

The laser setup is shown in Fig. 4.4 in a simplified form, where mirrors and the shutters are omitted.

#### 4.4.2 Offset-Lock

For the Raman coupling to work, it is crucial to maintain a stable frequency difference between the two Raman beams. Depending on the laser setup different methods can be applied to generate two beams with a stable frequency relation. Since in the laser setup introduced in the previous subsection 4.4.1 two different lasers are used as a source for the two Raman beam, some kind of offset-lock system has to be used to maintain a stable frequency relation. For such a purpose a device like the Toptica mFALC 110 can be used [58]. It is a modified version of the Toptica FALC 110 with a beforehand analog mixer installed. The mixer generates a beat signal between the interference beat signal and a sinusoidal signal generated with a local oscillator (LO). The function generator used as the LO is an Stanford Research

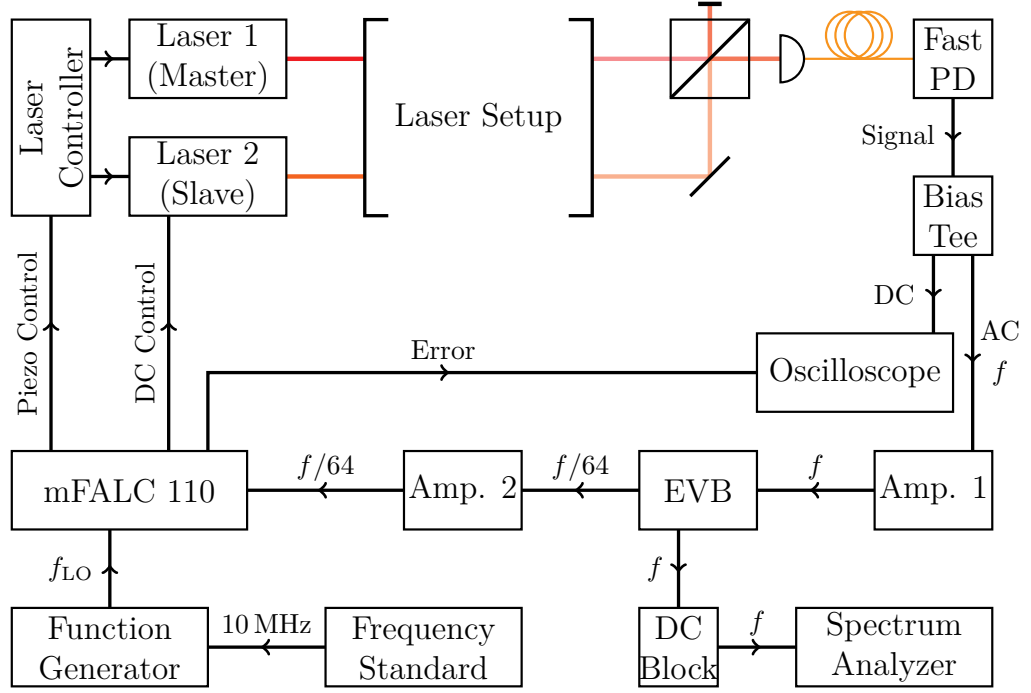


**Fig. 4.5:** Offset-lock setup scheme. A fast PD picks up the interference beat signal of the lasers and the electric signal is separated into DC and AC components by a bias-tee. The AC part with frequency  $f$  is amplified and fed into an evaluation board (EVB), which outputs a frequency divided signal  $f/64$ . The divided signal is amplified and used by the mFALC 110 together with a LO signal from a frequency generator to stabilize the frequency difference between the two lasers by controlling the piezo voltage and the laser current of the slave laser. The amplified AC part is also monitored at a spectrum analyzer and an oscilloscope monitors the DC signal and the error signal of the mFALC 110. An additional frequency standard can be used to trigger the function generator for a more stable operation.

Systems SG390 signal generator. The beat signal works as an error signal for the Toptica FALC 110, which it tries to minimize. In order to do this the mFALC 110 has two output ports of which one delivers a control signal for the piezo actuator for precise control of the grating for wavelength adjustment and the other delivers a signal for laser current control. The piezo control signal is fed into the laser controller, a Toptica DLC pro digital laser controller, and is used to compensate slow but comparably large drifts, while the current control signal is directly fed into the laser head to counteract fast but comparably small changes. The mFALC 110 can handle input signals with frequencies from 10 MHz up to 200 MHz and the optimum input voltage range lies between 10 mVpp and 700 mVpp.

However, the beat signal for the Raman transition will be in the order of 6.8 GHz. For scaling the beat signal to a usable range a Analog-Devices EVAL-ADF4007EBZ1 evaluation board is used. At the *MUXOUT* output of this evaluation board the input frequency is divided by 64, which gives a frequency of about 106.8 MHz and is thus usable with the mFALC 110. Unfortunately the frequency divided signal is an TTL signal with about 3 Vpp and the *MUXOUT* output has a 10 k $\Omega$  output impedance. With a connected SMA-type coaxial cable, acting as a capacitor, the

output impedance and the cable make a low pass filter. For a 1 m cable with an capacitance of 100 pF/m the output signal decreases to 5 mVpp, which makes an amplifier necessary. For this purpose a Mini-Circuits ZX60-3018G-S+ amplifier is used.

The signal put into the evaluation board is the amplified AC part of the interference beat signal. The amplifier used for this is a Mini-Circuit ZX60-83LN12+ low noise amplifier and the bias-tee used to separate the AC from the DC part is a Mini-Circuit ZX85-12G-S+. The DC output of the bias-tee, as well as the error monitoring output of the mFALC 110 are connected to an oscilloscope for monitoring. The amplified AC signal can be picked up at the *RFOUT* output of the evaluation board to monitor it with a spectrum analyzer.

The function generator was also supposed to be triggered externally by an Stanford Research Systems FS725 Rubidium Frequency Standard for extra stability, since due to the frequency division a deviation of 1 Hz at the function generator would correspond to 64 Hz deviation of the frequency difference between the two lasers. However, the frequency standard was out of order during the period of this work.

The offset lock system is illustrated in Fig. 4.5.

The locking procedure works as follows:

1. The fast PD, the evaluation board, the amplifiers, the spectrum analyzer and the function generator are turned on. The center frequency of the spectrum analyzer is set to the desired frequency separation and the frequency span is set to 1 GHz. The frequency of the LO is set to the desired frequency separation divided by 64 and an amplitude of  $-4$  dBm and the output is enabled.
2. The frequency difference is tuned to the desired separation  $\pm 0.5$  GHz by using the measured frequencies at the wavemeter and tuning the piezo voltage or the laser current at the laser controller.
3. The frequency difference is tuned to the desired separation  $\pm 30$  MHz by using the measured beat signal at the spectrum analyzer and tuning the piezo voltage at the laser controller.
4. The mFALC 110 is turned on and the amplification is ramped up until the frequency lock is applied, which is indicated by a jump of the carrier peak on the spectrum analyzer. When the lock is applied small deliberate changes of the piezo voltage should not effect the spectrum measured with the spectrum analyzer. Also the amplification should not be ramped up too high, such that higher sidebands become visible. The sidebands of first order are usually visible when the lock is applied but the power difference between them and the carrier should be kept over 30 dB. Typical spectra are shown in Fig. 4.6.

5. The unlimited integrator on the mFALC 110 is turned on for longer-term stability.

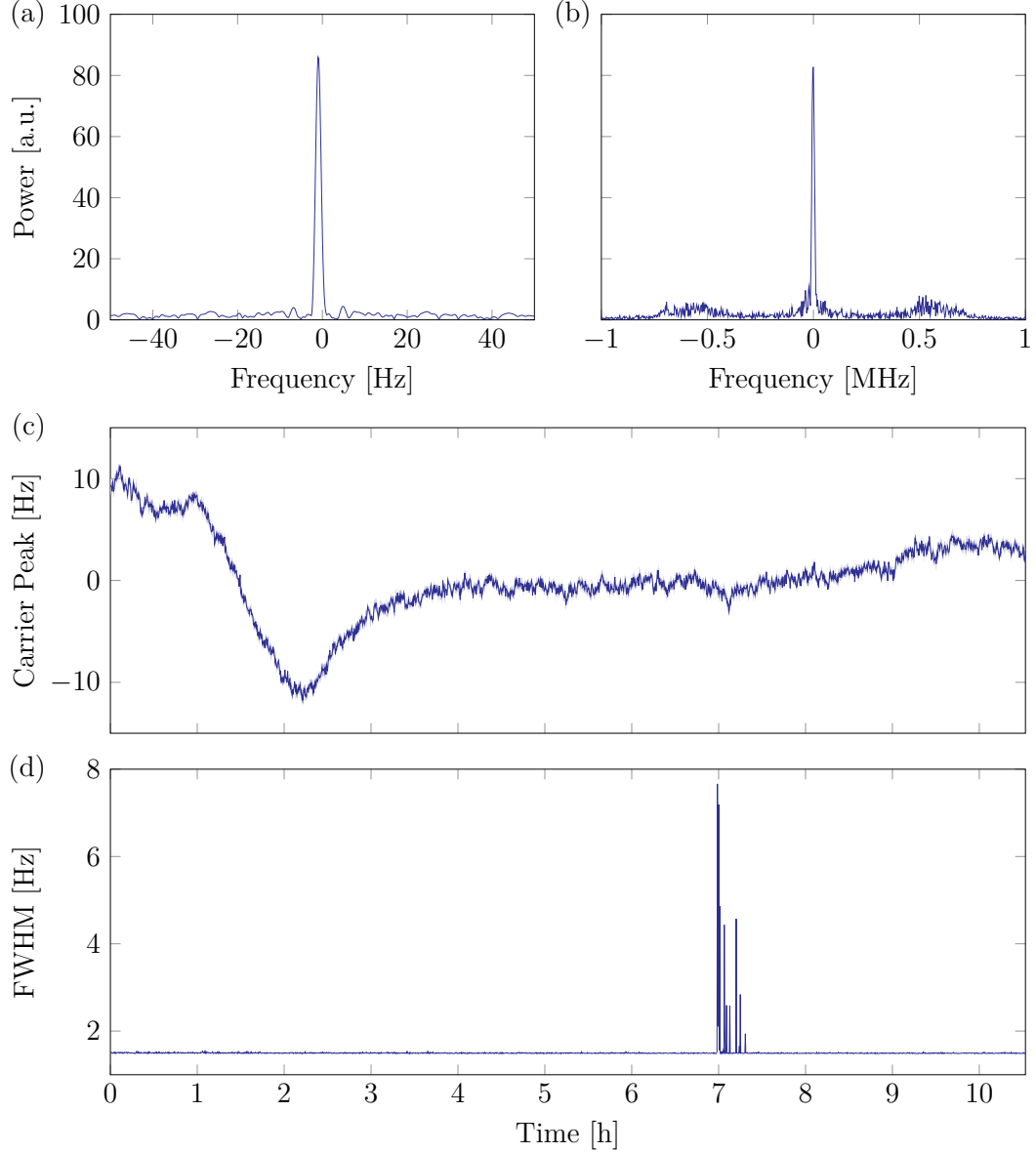


**Fig. 4.6:** Offset-lock spectrum and long time stability. (a) shows a typical spectrum with a span of 100 Hz relative to the center frequency and a bandwidth of 1 Hz. (b) shows a typical spectrum with a span of 2 MHz and a bandwidth of 10 kHz. The sidebands of first order are visible. The power is shown in a linear scale. In (c) the peak frequency of the carrier of the interference beat signal spectrum is shown with respect to the set center frequency, measured over a time span of 10.5 h. (d) shows the measured FWHM of the carrier peak over the same time period. (c) and (d) are averaged over 10 consecutive data points. The standard deviation is shown in (c) as the light blue area enclosing the data points connected by a blue line. The standard deviation for (d) is not shown as it is almost not visible with a mean value of 16.4 mHz for almost the entire time span except for the turbulent 20 minutes after 7 hours of measurement. For the highest peak there the standard deviation is 15.1 Hz.

To evaluate the performance of the offset lock system, the measured spectrum at the spectrum analyzer was measured over a period of 10.5 h with a span of 100 Hz

and a bandwidth of 1 Hz. The center frequency was set to the hyperfine frequency separation of the  $^{87}\text{Rb}$   $5S_{1/2}$  state of 6 834 682 610 Hz. The frequency of the LO was set to the same value divided by 64. As can be seen in Fig. 4.6, the carrier peak position varied by 22.9 Hz over the measurement period. The comparably large change occurs only during a period of two hours, while the rest of the measurement the change is quite slow and small. The beginning of the large and fast change coincides with the time the last person left the laboratory. A possible explanation for the coinciding change could be a change of the LO frequency due to temperature change in the room that effected the frequency generator. As mentioned before the LO was free running. Considering the frequency division this would correspond to a LO frequency change of 0.36 Hz. For a Rabi frequency of 10 kHz of a Raman transition, this deviation would cause a change of the Rabi frequency of 26.2 mHz. Therefore, the offset lock is stable enough and this issue was not addressed. Furthermore there seems to be some kind of turbulence of the full width at half maximum (FWHM), which was at 1.5 Hz for almost the entire time, except for seemingly random data points during a 20 minute period after seven hours of measurement. The reason for the disturbance is unknown, but such a behavior was never encountered again, which is why this issue was also not further addressed. The FWHM might even be smaller than 1.5 Hz since the measurement bandwidth was at the minimum of 1 Hz.

### 4.4.3 Raman Transition Experiment

As the lattice beams were not installed yet and in order to check if the laser and offset lock system are suitable, the Raman 1 and 2 beams were installed preliminary on the experimental table. They were aligned copropagating and their polarizations were set perpendicular to each other. The copropagation is necessary to avoid the

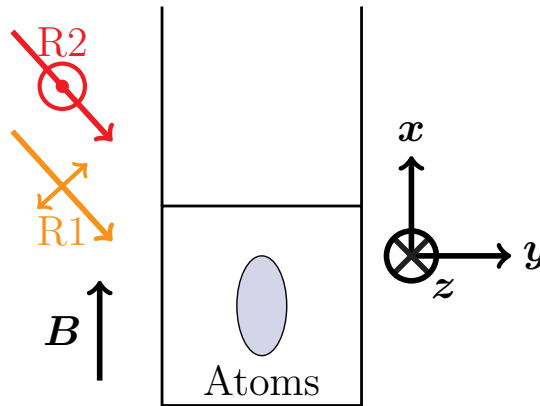


**Fig. 4.7:** Beam alignment for Raman transition. The Raman 1 (R1) and 2 (R2) beams are overlapped and have perpendicular linear polarization with respect to each other. They lie in the  $x$ - $y$ -plane. The magnetic field is showing along the  $x$ -axis. Since the polarization of R2 is completely and of R1 to large parts perpendicular to the magnetic field the Raman transition driven is of the  $\pi^\pm - \pi^\mp$  type.



transition to become velocity selective. Additionally a magnetic field of 1 G was applied along the  $\mathbf{x}$ -axis. The setup is illustrated in Fig. 4.7. The magnetic field sets the quantization axis of the atoms and also lifts the degeneracy of the magnetic states, such that by choosing the right frequency difference for the Raman process only one transition between two magnetic states is resonant. The transition chosen for this experiment was a  $\pi^\pm - \pi^\mp$  type Raman transition between the states  $|1,0\rangle$  and  $|2,0\rangle$ . Transitions between these two states are called clock transitions as their energetic separation is not effected by small magnetic fields and thereby they are insensitive to magnetic field fluctuations. This makes them ideal candidates for conventional atomic clocks. For the same reason they are best suited to directly observe Rabi oscillations. For this transition both beams should be polarized linear

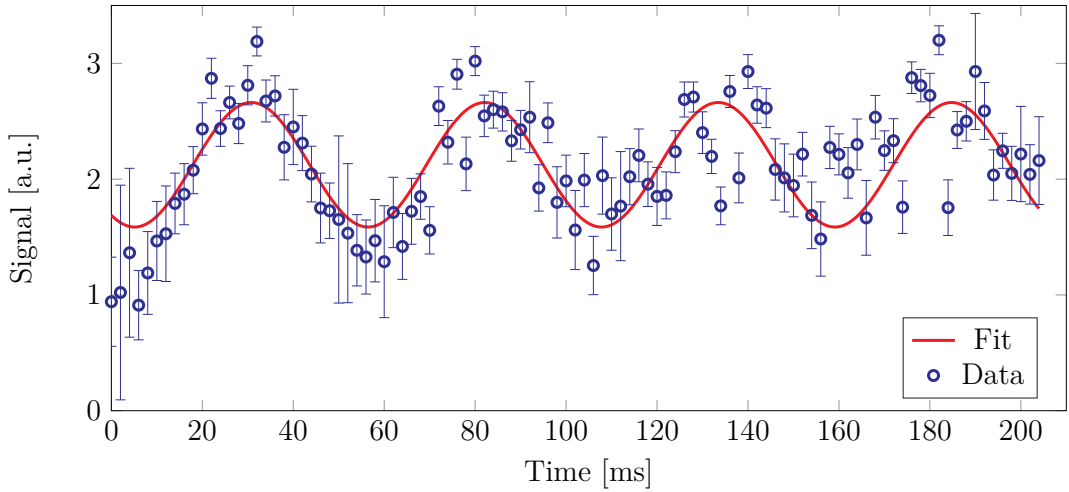


**Fig. 4.8:** Observed Rabi oscillation by a Raman transition. In a copropagating alignment R1 and R2 drive  $\pi^\pm - \pi^\mp$  type Raman transitions on the clock transition between  $5S_{1/2} |2,0\rangle$  and  $5S_{1/2} |1,0\rangle$ . The oscillation can clearly be observed, even though for longer time periods decoherence washes it out. By fitting a sinusoidal function to the data a Rabi frequency of  $(19.5 \pm 0.5)$  kHz is obtained. The expected value by a calculation with the experimental parameters is 19.4 kHz.

but perpendicular to each other and also perpendicular to the quantization axis. But as the beams are aligned with an angle of  $60^\circ$  with respect to the quantization axis in the  $\mathbf{x} - \mathbf{y}$ -plane one of the beams will only contribute with  $\sqrt{3}/2$  parts of the electric field amplitude or  $3/4$  parts of its power to the transition.

To measure the oscillation first the atoms in the  $5S_{1/2} |F=2\rangle$  state are blasted out by using the imaging beam, which drives transitions between  $5S_{1/2} |F=2\rangle$  and  $5P_{3/2} |F=3\rangle$ . Afterwards the Raman beams are applied to transfer atoms from  $F=1$  to  $F=2$ . The transferred atoms can than be imaged by the imaging beam. The atoms were trapped in a far-off-resonance optical trap for the measurement. With estimated powers of 32 mW for R2 and 25 mW for R1 at the atom position and measured beam waists of 1.9 mm and 0.8 mm respectively a Rabi frequency of 19.4 kHz is expected.

The fit in Fig. 4.8 gives a Rabi frequency of  $(19.5 \pm 0.5)$  kHz. The signal is propor-

tional to the fluorescence counts of the used detector. The maximum signal obtained for the transitioned population corresponds to a fraction of 0.27 of the total population signal. As the population should be distributed equally over the the magnetic sublevels, it is expected that a fraction of 0.33 of the population takes part in the transition.

It can be seen that with longer transition periods the signal gets washed out. This decoherence is most likely due to the Gaussian intensity profile and the consequential position dependent Rabi frequency.

#### 4.4.4 Repump lasers

In addition to the Raman laser setup to prepare the Raman beams, a laser system preparing the Raman repumpers (RP) is necessary. The required frequency for the RP1 beam matches the frequency of the imaging repumper already installed at the experiment. Its primary purpose is to pump the atoms from the  $5S_{1/2} |F = 1\rangle$  states into the  $5S_{1/2} |F = 2\rangle$  state since the imaging system is configured to image atoms in the latter state. Previously there were no beams matching the requirements for RP2 and RP3. However, the laser for the three dimensional magneto optical trap (3D-MOT) of the experiment has a similar frequency. It is detuned 106.65 MHz from RP2 and  $-160$  MHz from RP3. To create the necessary beams some of the 3D-MOT beam will be branched off and is subsequently adjusted to the correct frequencies by using AOMs. For RP3 a AOM modulating with a frequency of 80 MHz is used in a double pass configuration. A double pass configuration uses a PBS before and a quarter wave plate (QWP), a lens and a retroreflecting mirror after the lens such that the beam after passing the AOM and being modulated with 80 MHz follows the initial path back through the AOM, being modulated with 80 MHz a second time, but with  $90^\circ$  turned polarization until it arrives at the PBS where it is separated from the incoming beam. RP2 uses a single pass AOM configuration, directly modulating 106.65 MHz. The used AOMs are of the same type as in the Raman laser setup.

The cooling scheme presented in 4.1 requires that the repumpers drive  $\sigma^-$  transitions. This means that they have to be aligned along the quantization axis with circular polarization. As shown in Fig. 4.7 the quantization axis coincides with the spatial axis declared as the  $\mathbf{x}$ -axis.

Furthermore, the experiment first captures atoms in a low-vacuum chamber with a 2D-MOT from where they are pushed through a narrow tube into a high-vacuum chamber where they are captured in the 3D-MOT. This pushing process works through the radiation pressure of a pushing beam which is as well aligned along the  $\mathbf{x}$ -axis but propagates in the negative direction. Also the position of the triangular lattice, which is the sample position for the planned quantum gas microscope (QGM), is not at the 3D-MOT position but is also connected to it through the

$x$ -axis. In order to bring the atoms from the 3D-MOT position to the QGM position an optical tweezer is used which is once again aligned along the  $x$ -axis but propagating in positive direction. Since both directions along the  $x$ -axis were already occupied, one of the existing beam paths had to be rebuilt. As the optical tweezer setup is much more extensive and additionally the unoccupied space on that side of the experimental table is less, it was decided to rebuild the pushing beam setup. A

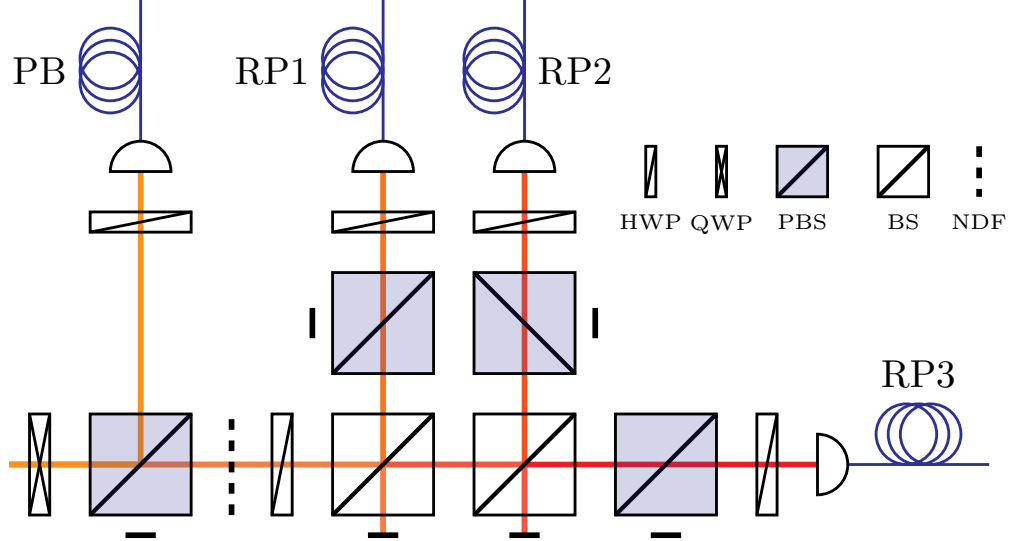


**Fig. 4.9:** Raman repumper output setup. Eventhough, the repumpers are guided through polarization maintaining fibers they are polarization cleaned by using HWP and PBS<sup>1</sup>. They are overlapped by using 50:50-BS. This makes only half of the power of RP1 and only a fourth of the power of RP2 and RP3 usable. Another HWP is used to adjust their collective polarization. With a neutral density filter (NDF) that is installed on a flippable mount, the applied power can be dynamically switched between two ranges. The neutral density amounts to 2.5. A subsequent PBS is used to combine the pushing beam with the repumpers. A quarter wave plate (QWP) is used to set the circular polarization necessary for driving  $\sigma^-$  transitions. Mirrors, beam samplers and PDs for power measurement are omitted.

schematic depicting the setup which couples the beam paths of the pushing beam and the three repumper beams is given in Fig. 4.9. The combined repumper beams and the pushing beam are overlapped by using perpendicular linear polarizations and a PBS. The repumpers are combined beforehand by using simple BSs. Due to the BSs one of the repumpers, RP1, can only apply half of the beam power after the transporting fiber while the other two repumpers can only apply a fourth of their power after the fiber. For all current scenarios all repumpers still have enough power. Recalling the Raman cooling scheme and the necessary Rabi frequencies for the repumpers, during cooling powers of only a few tens to a few hundred nanowatt are required. This necessitates neutral density filters (NDF). Such NDF are installed before combining the repumpers with the pushing beam. They are mounted on a flippable stage, making it possible to remove them from the beam path by using a

TTL signal.

The circular polarization is set by a QWP after combining all four beams. It can be adjusted by using a retroreflecting silver mirror after the QWP and setting the angle of the QWP such that the power reflected into the pushing beam path is maximized. To check if the right circular polarization was adjusted a microwave spectrum can be taken after applying RP1 and RP2. If the right polarization was chosen, there should only be a resonance at the frequency separating  $5S_{1/2} |2, -2\rangle$  and  $5S_{1/2} |1, -1\rangle$ .

The spatial alignment for the pushing beam can be adjusted by maximizing the atoms collected in the 3D-MOT. RP3 was aligned by applying and adjusting it to minimize the measured atoms in the  $5S_{1/2} |F = 2\rangle$  ground state. For RP2 a similar procedure was applied. Though RP2 ideally would only pump the atoms into  $5S_{1/2} |2, -2\rangle$ , imperfections of the polarization or scattering over  $5P_{3/2} |3, -3\rangle$  in combination with a high intensity does still lead to a significant loss of atoms. RP1 was aligned by maximizing the observed atoms. This works because the imaging system can only image atoms in  $5S_{1/2} |F = 2\rangle$  and RP1 can pump atoms from  $|F = 1\rangle$  into  $|F = 2\rangle$  and thereby increase the number of observable atoms. In order to only measure the atoms in  $|F = 1\rangle$ , the  $|F = 2\rangle$  atoms have first to be blasted away by using the imaging beam or RP3.

#### 4.4.5 Quantum Gas Microscope Setup

As mentioned in 3.3 the controlled coupling of neighboring sidebands via Raman transitions requires that the rotational symmetry of the system under investigation is at least discretized. Here this is done by the triangular lattice. This discretization sets specific angles with respect to the lattice vectors that are best suited to couple all possible eigenstates of the lattice to neighboring ones. The Raman 1 beam is already fixed in its alignment perpendicular to the quantization axis in order to drive  $\pi^0$  transitions and the optical axis limits the angle between Raman 1 and the horizontal plane to a maximum of  $24^\circ$ . The Raman 1 Vertical (R1V) was installed with this angle of  $24^\circ$  to the horizontal plane. With respect to the ideal angles for the projected momentum only a few positions for Raman 2 (R2) are suitable. The actual possible alignments however are even less as the optical access does only allow for two directions to be implemented without changing already existing installments. As it was the option with the higher effective momentum R2 was set

---

<sup>1</sup>This step is redundant and should have been omitted as the PBSs are not necessarily oriented exact the same way and thereby the polarization of the repumpers will be minimally tilted to each other without using additional HWPs after the PBSs. This would cause a loss at the last PBS combining the pushing beam and the repumpers. The combining PBS alone would be sufficient for cleaning the polarization of the repumpers and ideally would not cause any additional loss as the polarization of each repumper could be adjusted individually with respect to the orientation of the combining PBS. In practice the loss is minimal but it is still a redundant use of PBS.

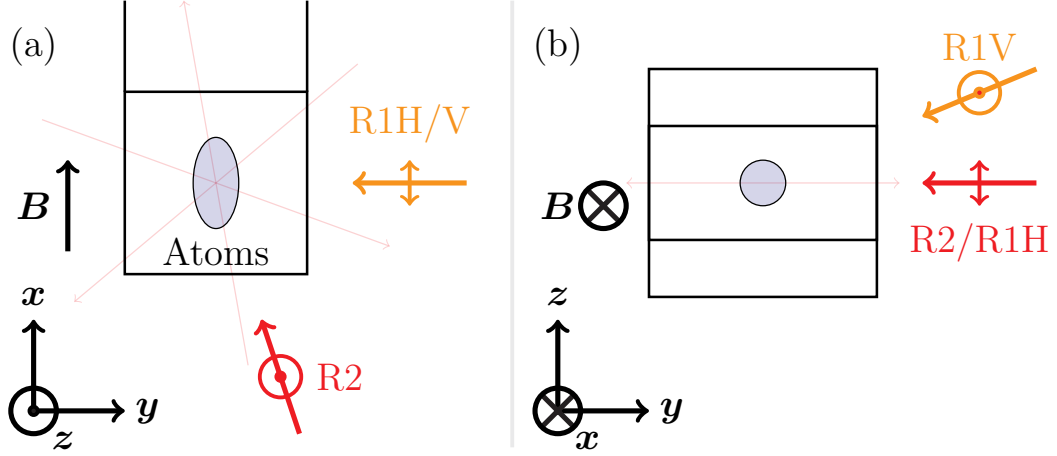


**Fig. 4.10:** Beam alignment for Raman sideband coupling. The Raman 1 (R1) and 2 (R2) beams are overlapped and have perpendicular linear polarization with respect to each other. They lie in the  $x$ - $y$ -plane. The magnetic field is showing along the  $x$ -axis. Since the polarization of R2 is completely and of R1 to large parts perpendicular to the magnetic field the Raman transition driven is of the  $\pi^\pm - \pi^\mp$  type. (a) shows the alignment in the  $x-y$ -plane. In (b) the  $z-y$ -plane is presented. The lattice beam alignment is visualized by the thin light red arrows. Angles are not to scale.

with an angle of about  $70^\circ$  with respect to the horizontal projection of R1. The alignment of the Raman and the lattice beams at the QGM position is illustrated in Fig. 4.10. Considering that the wave vectors of the lattice beams have an angle of  $120^\circ$  to each other and that one of the lattice beams has an angle of  $9.2^\circ$  to the  $x$ -axis it can be calculated that the effective momentum has an angle of  $16.7^\circ$  to one of the lattice beams, which is near the ideal angle of  $15^\circ$ . With this configuration the maximum possible Lamb-Dicke parameter in the triangular lattice plane amounts to 0.23 according to the numerical calculation based on the triangular lattice Wannier functions. This setup of R2 and R1V was first used to spectroscopically the sidebands. The steps for taking a spectrum are:

1. Pumping all atoms in the  $5S_{1/2} |2, -2\rangle$  state by applying RP1 and RP2.
2. Applying the Raman beams.
3. Blast away the atoms in the  $5S_{1/2} |F = 2\rangle$  state by using the imaging/probe beam.
4. Image the atoms in the  $5S_{1/2} |1, -1\rangle$  state by using the RP1/imaging repump beam.

The detuning of the Raman beams from the  $D_1$  line was 100 GHz. However, when the triangular lattice and the vertical lattice were both applied, the spectrum, as seen in Fig. 4.11, looked disturbed. One broad resonance is observable between 0 and 30 kHz, which is associated with the carrier transition. A clear sideband can be seen at about 50 kHz. This blue detuned sideband could be the cooling sideband

of the vertical lattice as the value for the trap frequency of the vertical lattice was measured by modulation spectroscopy to be 35 kHz. The sidebands of the triangular

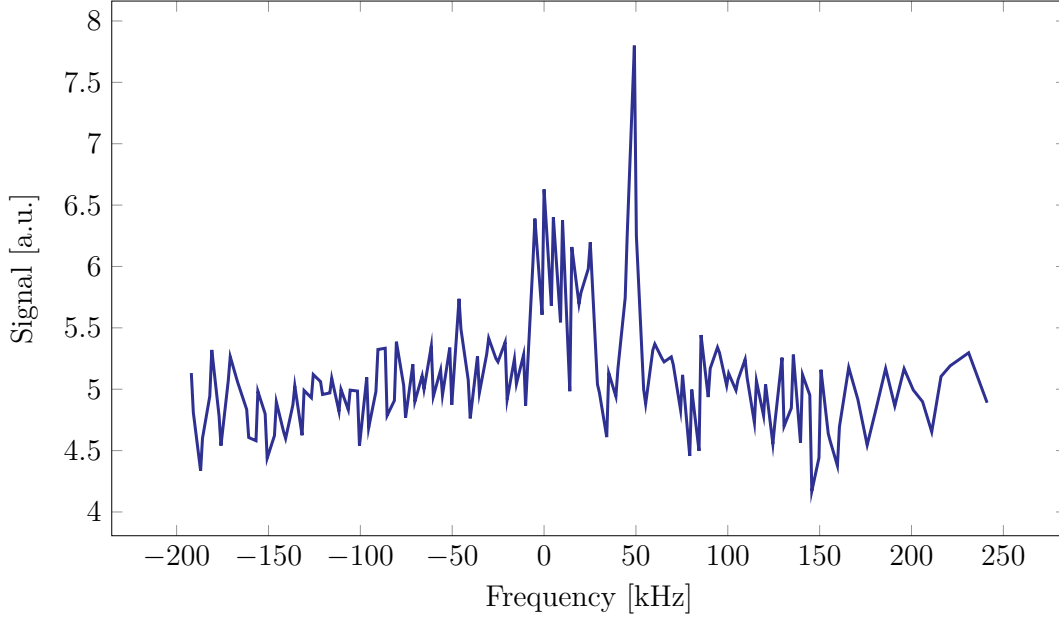


**Fig. 4.11:** Sideband spectrum in the 3D lattice using Raman 1 Vertical. The carrier can be seen as a broad resonance between 0 and 30 kHz. One sideband can be observed at 50 kHz, which may correspond to the cooling sideband of the vertical lattice. Neither the heating sideband of the vertical lattice nor the sidebands of the triangular lattice are clearly observable. No errorbars are shown as each datapoint was only taken once.

lattice are not observable at all. If higher Raman beam powers are used in order to increase the coupling the spectrum becomes even more disturbed as shown in Fig. 4.12. Only a very broad resonance is observable. While searching for reasons for these strange spectra, one explanation that came up was that of a magnetic state dependent vertical lattice. As explained in more detail in [59, 60] state dependent lattices are shifted relatively to each other depending on the internal state of the atom. The underlying effect is a spin and polarization dependent light shift as further explained in [45]. It becomes significant if the detuning of the trapping light is not much larger than the hyperfine splitting between the  $5P_{1/2}$  and  $5P_{3/2}$  states. Here the vertical lattice has a wavelength of 810 nm and is thereby in the same order as mentioned hyperfine splitting. If beams of the same wavelength and linear but relatively to each other tilted polarization are interfered a standing wave forms that has local pools where the electromagnetic field is elliptical or even circular polarized. The same effect can be used for polarization gradient cooling. As the different magnetic states are spatially shifted to each other the parity is broken through the lattice geometry and a coupling between neighboring vibrational levels should even occur without a momentum projection. This means that the sidebands of the vertical lattice should in principle as well be observable with microwave transitions. A spectrum taken the same way as the Raman spectra but with a microwave

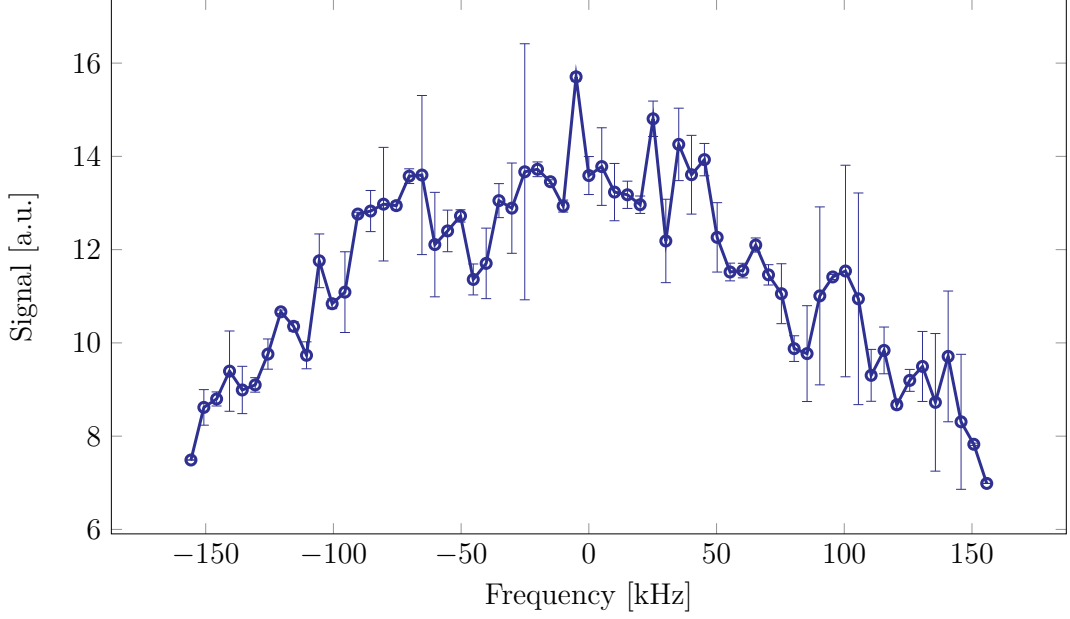


**Fig. 4.12:** Sideband spectrum in the 3D lattice using Raman 1 Vertical and high Raman powers. The usage of high Raman powers in combination with the 3D lattice caused that no sidebands can be located. The spectrum just shows a very broad resonance.

transition instead of a Raman transition is shown in Fig. 4.13. And indeed next

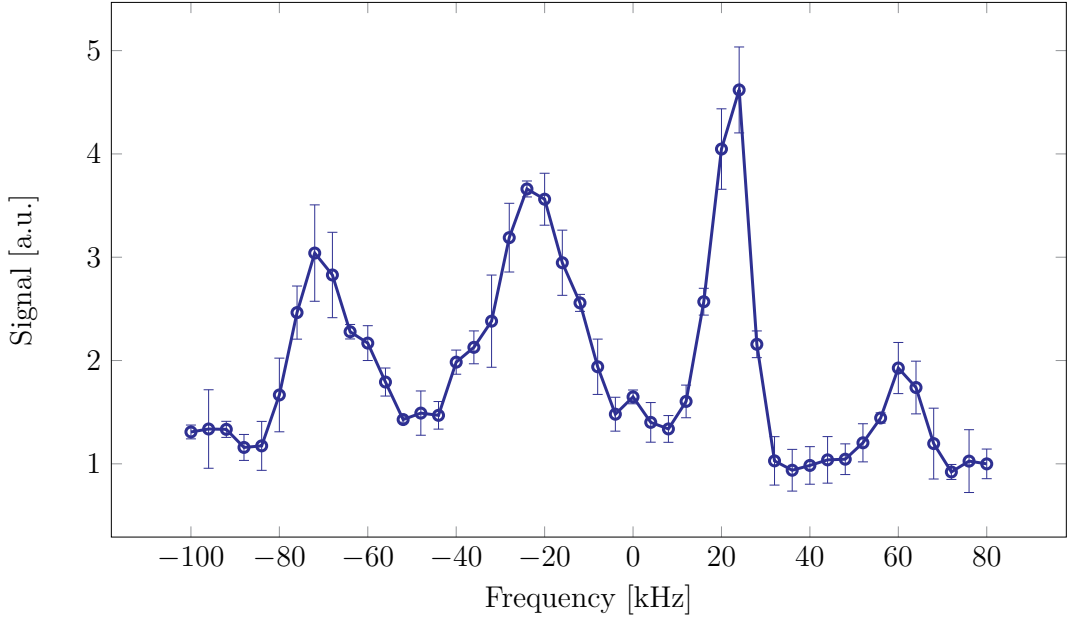


**Fig. 4.13:** Sideband spectrum using a microwave transition. The state dependent lattice makes it possible to couple neighboring vibrational levels even with very small momentum projection since the displacement of the magnetic states already breaks the parity of the lattice eigenfunctions.

to the carrier the sidebands were observable. Such microwave sideband transitions could in principle be used for cooling purposes as done in [60] but since they require a state dependent lattice they might be unpractical for the further course of the experiment as such state dependencies might influence the model Hamiltoni-

ans to be simulated. By adjusting the polarization alignment of the vertical lattice beams the vertical lattice sidebands observable with the microwave transition could be minimized. But still spectra taken with the Raman transition were disturbed. To evade the effects of the vertical lattice for the time being further spectroscopy was done without the vertical lattice. As shown in Fig. 4.14 without the vertical

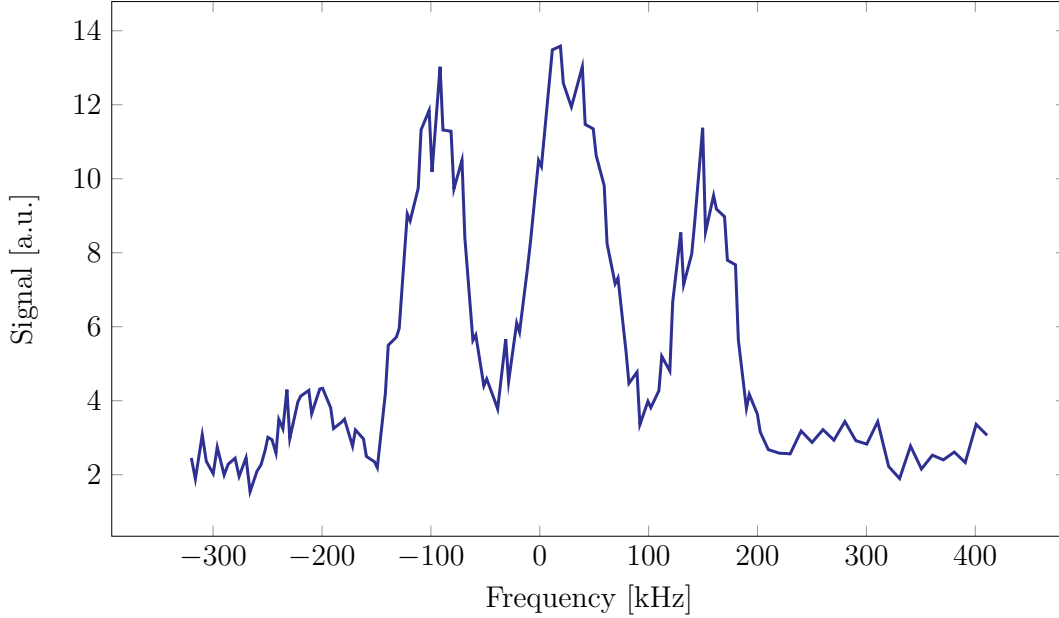


**Fig. 4.14:** Sideband spectrum using Raman 1 Vertical without the vertical lattice. Without the vertical lattice the sidebands of the triangular lattice can be observed with frequency separations of 130 kHz. But the sidebands and the carrier seem too broad. Possibly due to doppler broadening. No errorbars are shown as each datapoint was only taken once.

lattice next to the carrier clearly two sidebands are visible even though they seem quite broad. With a separation of about 130 kHz from the carrier resonance they match the trap frequency of 130 kHz measured by modulation spectroscopy. The broad appearance is suspected to originate from doppler broadening. Without the vertical lattice the atoms are only weakly trapped in the  $z$ -axis direction and R1V applies a momentum along the same axis. In order to avoid doppler broadening, the Raman 1 Horizontal (R1H) beam was installed. R1H is coupled in the same path of an already existing beam used for absorption imaging at a PBS. Unfortunately this beam path contains a QWP in the further route and thereby changes the polarization from linear to circular. This effects the Raman transition mainly in the aspect of the power that is applied onto the atoms by R1H for the  $\pi^0$  transition. As the wavevector is perpendicular to the quantization axis, only half of the light will contribute to the  $\pi^0$  coupling. The other half will contribute to  $\sigma^-$  and  $\sigma^+$  couplings equally. These  $\sigma^\pm$  transitions create additional Raman paths. One of the three kinds of new paths are couplings with  $\Delta F = 0, \pm 1$  and  $\Delta m_F = \pm 2$ . As these are strongly suppressed for far detuned Raman, transitions such as applied here, these can be neglected. The other kind are  $\sigma^\pm - \sigma^\pm$  transitions with  $\Delta F = \pm 1$



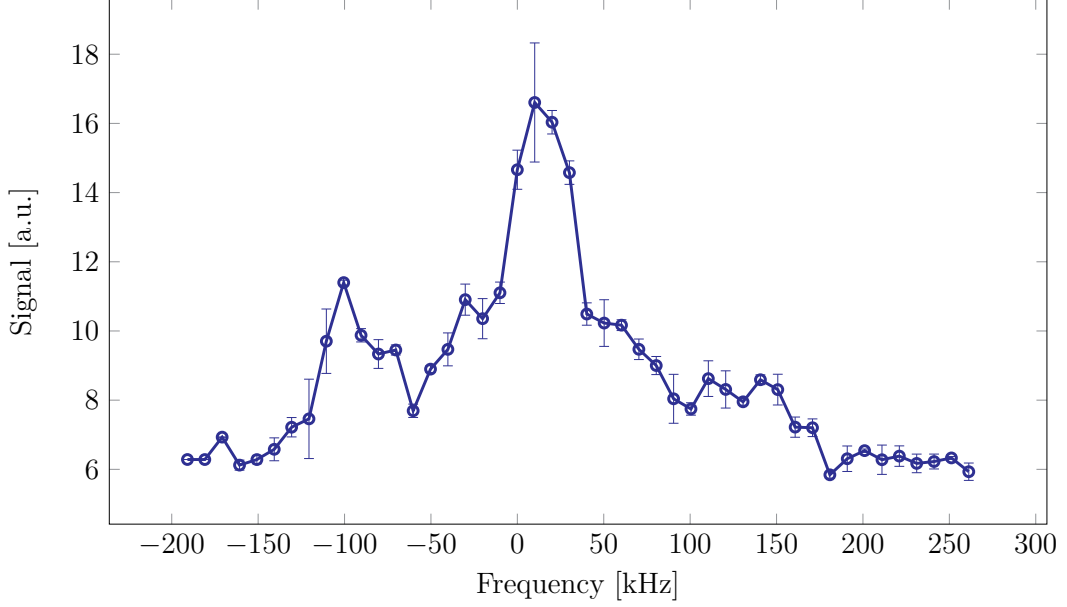


**Fig. 4.15:** Sideband spectrum using Raman 1 Horizontal in the 3D lattice. The heating sideband of the triangular lattice can be observed and it can be guessed where the cooling sideband lies. Compared to the previous spectrum in Fig. 4.14 the signal decreased.

and  $\Delta m_F = 0$ . Considering the detuning due to the magnetic field of 1 G the one transition of these  $\sigma^\pm - \sigma^\pm$  transitions with the lowest detuning  $\delta$  is the one between  $5S_{1/2} |2, -1\rangle$  and  $5S_{1/2} |1, -1\rangle$ , with  $\delta = 700$  kHz. Even if only these two states are considered with a bare Rabi frequency of 54 kHz, according to Eq. 2.48 and Eq. 2.13 only 5.9‰ of the population will take part in the transition and are thereby negligible. For the other two coupled states by this transition type the detunings are 2.1 MHz and 3.5 MHz. The third kind of newly appearing transitions are  $\pi^0 - \sigma^\pm$  transitions with  $\Delta F = 0$  and  $\Delta m_F = \pm 1$ . These are detuned  $\delta = 700$  kHz as well and the same discussion as the previous one can be applied. For a more accurate estimation the Rabi frequencies for the specific transitions need to be calculated but as the transition between  $5S_{1/2} |2, \pm 2\rangle$  and  $5S_{1/2} |1, \pm 1\rangle$  are the strongest possible while maintaining the applied intensity, the estimations made here are upper limits. Based on the trigonometrical calculated momentum projection and the numerically calculated Lamb-Dicke parameter for the triangular lattice Wannier functions the maximum possible Lamb-Dicke parameter for the R2-R1H configuration amounts to 0.24. As shown in Fig. 4.15 using R1H with the vertical lattice also gives a disturbed spectrum. A spectrum taken with R2 and R1H with only the triangular lattice is shown in Fig. 4.16.

## 4.5 Sideband cooling and Rabi Frequency Measurement

This section will focus on the successful application of the developed continuous Raman sideband cooling scheme and explain the unusual spectrum shape of the sidebands. Moreover, the Rabi frequency of the Raman transition in dependence of the applied power is investigated.

### 4.5.1 Application of continuous Raman Sideband cooling

With the setup consisting of Raman 2, Raman 1 Horizontal, the Raman repumpers 1 and 2 and the triangular lattice Raman sideband cooling should be observed. The detuning of the Raman beams was set to 200 GHz from the  $D_1$  line. Before the Raman sideband cooling could be applied it was necessary to determine which frequency to set for the cooling process. For this purpose a spectrum was taken again as shown in Fig. 4.16. The peak of the cooling sideband appeared to be at 128 kHz with respect to the carrier transition. R2 was applied with a power of 33 mW and R1H with 22 mW with estimated beam waists of 1.25 mm. The repumpers were applied with powers of 1  $\mu$ W with similar beam waists. The actual intensities cannot be certainly calculated as neither the power loss at the glass cell nor the beam waist at the atom position are known. The steps for the Raman sideband cooling are:

1. Pumping all atoms in the  $5S_{1/2} |2, -2\rangle$  state by applying RP1 and RP2.
2. Applying the Raman beams and the repumpers simultaneously.
3. Turn off the Raman beams after 300 ms illumination.
4. Keep the repumpers on for additional 15 ms to pump all atoms back into  $5S_{1/2} |2, -2\rangle$ .

These steps are combined with a subsequent spectroscopy measurement to observe how the Raman sideband cooling influenced the spectrum. It can be directly seen in Fig. 4.16 that the Raman sideband cooling procedure had some influence. The signal of the cooling sideband decreased. This can intuitively explained by the ground state occupation. Since the vibrational ground state in  $5S_{1/2} |2, -2\rangle$  is a dark state for the Raman sideband transition, they will not take part in the transition. As the cooling transfers more atoms into the vibrational ground state, more atoms become dark for the transition at the cooling sideband and therefore the signal decreases. According to [60] this phenomena can be used to estimate the mean vibrational occupation  $\langle n \rangle$  by

$$\langle n \rangle = R - 1 = \frac{P_{HSB}}{P_{CSB}} - 1. \quad (4.10)$$

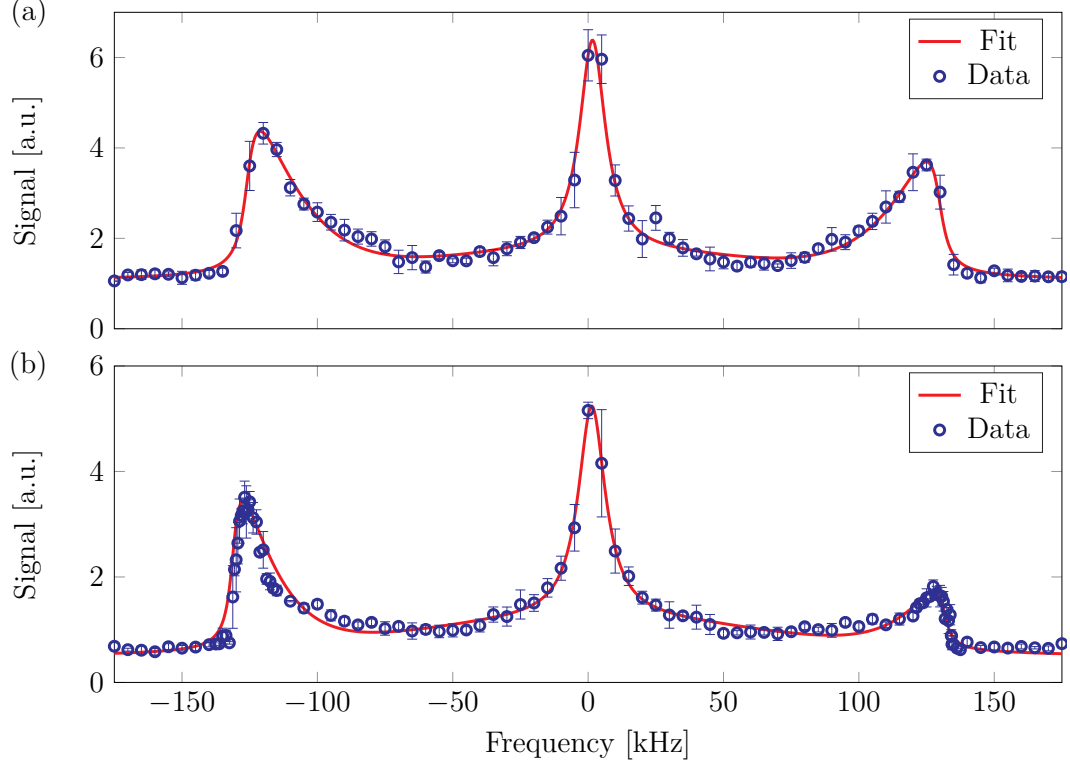


**Fig. 4.16:** Sideband spectrum after Raman sideband cooling. (a) shows the sideband spectrum without any Raman sideband cooling applied. In (b) the spectrum after 300 ms of cooling is shown. It can clearly be observed that the signal from the CSB decreases after cooling. As more atoms are transferred into the vibrational ground state less atoms can take part in the transition on the CSB as the vibrational ground state is a dark state for this transition. From the population ratio of the sidebands the mean vibrational level can be estimated. Before cooling it is  $1.11 \pm 0.08$ . By cooling it decreases to  $0.28 \pm 0.02$ .

$P_{HSB/CSB}$  are the transferred population on the heating sideband (HSB) or the cooling sideband (CSB) respectively which is proportional to the respective obtained signal and  $R$  is the ratio of the CSB to the HSB population. Using this relation the mean vibrational level before cooling is found to be  $1.11 \pm 0.08$ . After cooling it is  $0.28 \pm 0.02$ .

### 4.5.2 Unsymmetric Sidebands

The unsymmetric shape of the sidebands comes from using only a two dimensional lattice. The beams creating the triangular lattice have a transversal two dimensional Gaussian intensity distribution. This means that the triangular trap frequency varies with the displacement along the  $z$ -axis. The trap frequency can be described as

$$\omega_{Tri}(z) = \omega_{Tri}^{max} \exp\left(-\frac{z^2}{w_0^2}\right). \quad (4.11)$$

$\omega_{Tri}^{max}$  is the maximum trap frequency for the triangular lattice and  $w_0$  is the beam waist of the lattice beams. Additionally, as the atoms are only weakly confined along

the  $z$ -axis, the distribution along the  $z$ -axis can be described by the Boltzmann distribution with

$$\mathcal{P}(z) = \frac{1}{\mathcal{Z}} \exp\left(\frac{E_z}{k_B T_z}\right) = \frac{1}{\mathcal{Z}} \exp\left(-\frac{m\omega_z^2 z^2}{2k_B T_z}\right), \quad (4.12)$$

with the partition function  $\mathcal{Z}$ . If now Eq. 4.11 is solved for

$$z^2 = -w_0 \ln\left(\frac{\omega_{Tri}}{\omega_{Tri}^{max}}\right), \quad \omega_{Tri} \in [0, \omega_{Tri}^{max}], \quad (4.13)$$

the distribution can be expressed as

$$\mathcal{P}(\omega_{Tri}) = \frac{1}{\mathcal{Z}} \left(\frac{\omega_{Tri}}{\omega_{Tri}^{max}}\right)^\alpha, \quad \text{with} \quad (4.14a)$$

$$\alpha = \frac{m\omega_z^2 w_0^2}{2k_B T_z}. \quad (4.14b)$$

The spectrum for one sideband  $\mathcal{F}_{SB}$  can now be calculated as the convolution of the distribution function and the uninfluenced spectrum  $\mathcal{F}$  as

$$\mathcal{F}_{SB}(\omega) = \int_0^{\omega_{Tri}^{max}} \mathcal{F}(\omega - \omega') \mathcal{P}(\omega') d\omega'. \quad (4.15)$$

According to Eq. 2.48 and Eq. 2.13 the ideal uninfluenced spectrum should be given by a Lorentz function. Examples of the Lorentz function, the distribution function and the convolution of both are shown in Fig. 4.17. A value proportional to the respective transferred population over the HSB can be calculated by integrating over the HSB spectrum

$$P_{HSB} \propto \int \mathcal{F}_{HSB}(\omega) d\omega = A_{HSB} \int \mathcal{F}_{SB}(\omega) d\omega, \quad (4.16)$$

where  $A_{HSB}$  is a scaling factor proportional to the transferred population but also proportional to the maximum of the sideband. The same relation holds for the CSB. Therefore the ratio  $R$  is given by

$$R = \frac{P_{HSB}}{P_{CSB}} = \frac{A_{HSB}}{A_{CSB}} \quad (4.17)$$

and can be determined by calculating the ratio of the respective sideband maxima.

### 4.5.3 Raman Rabi Frequency Measurement

Currently it is not possible to directly measure the Rabi oscillations caused by the Raman transition for the coupling between  $5S_{1/2} |2, -2\rangle$  and  $5S_{1/2} |1, -1\rangle$ . The origin

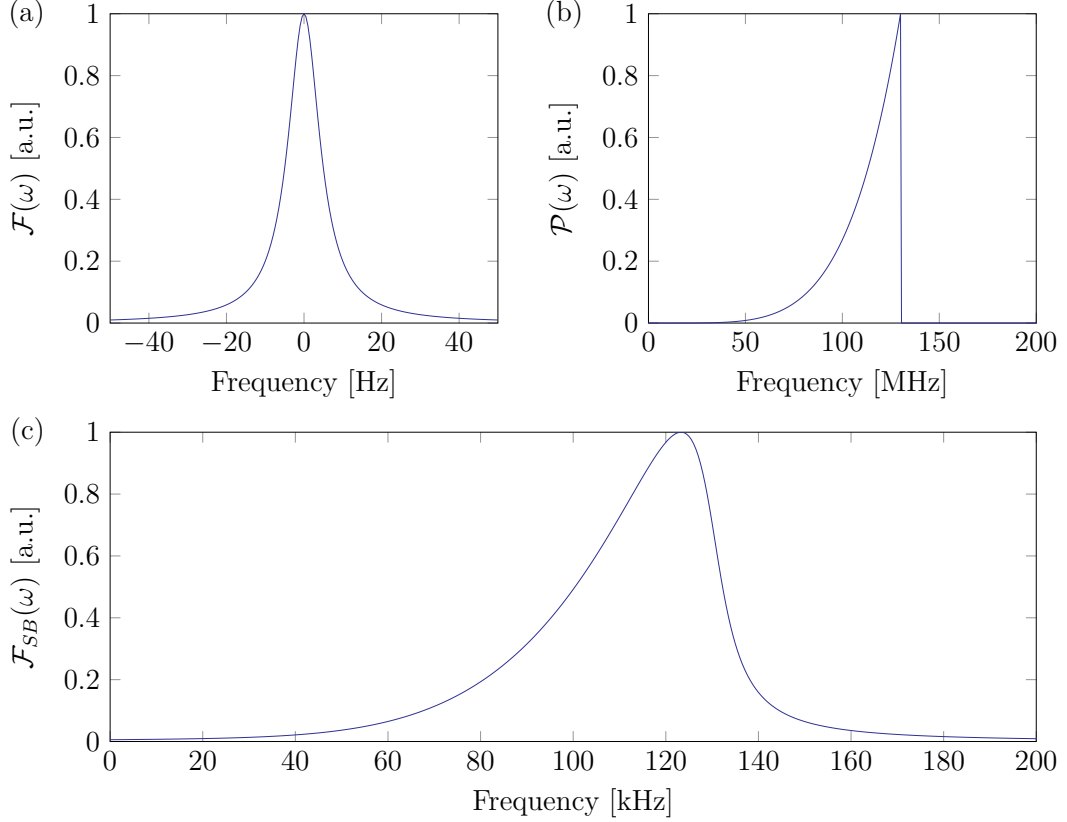


**Fig. 4.17:** Example for a unsymmetric sideband. In (a) a normalized Lorentzian function is shown as an exaple for the expected uninfluenced spectrum of the a Raman sideband transition. (b) shows the normalized distribution over the frequency due to the spatial dependence of the 2D triangular lattice trap frequency in the vertical direction. (c) shows the normalized convolution of (a) and (b), which is the expected shape of the sidebands. This convolution function was used to fit the spectra shown in Fig. 4.16.

of the effect hindering the observation is not certainly determined but it is suspected to be magnetic field fluctuations from the passive magnetic field compensation coils, which also set the quantization axis. However, the Rabi frequency can still be measured indirectly. This can be done by using the Raman beams to sweep over the resonance of the transition that is under investigation. As well explained in [61] the transition probability for such a transition scheme in dependence of the sweep time can be described by the Landau-Zener formula. In a scheme with a linear frequency sweep the relative transferred population is given by

$$P_e(t) = 1 - \exp\left(-\frac{\pi\Omega^2}{2\Delta}t\right). \quad (4.18)$$

The Rabi frequency  $\Omega$  and the sweep range  $\Delta$  are both given in angular frequencies. In Fig. 4.18 a data set with a Landau-zener function fit is shown to determine the Rabi frequency of the transition with  $(23.1 \pm 4.2)$  kHz. It is also shown that the Rabi frequencies for different R1H powers resemble the square root shape as expected from Eq. 2.46 and Eq. 2.7 as the beam power is proportional to the square

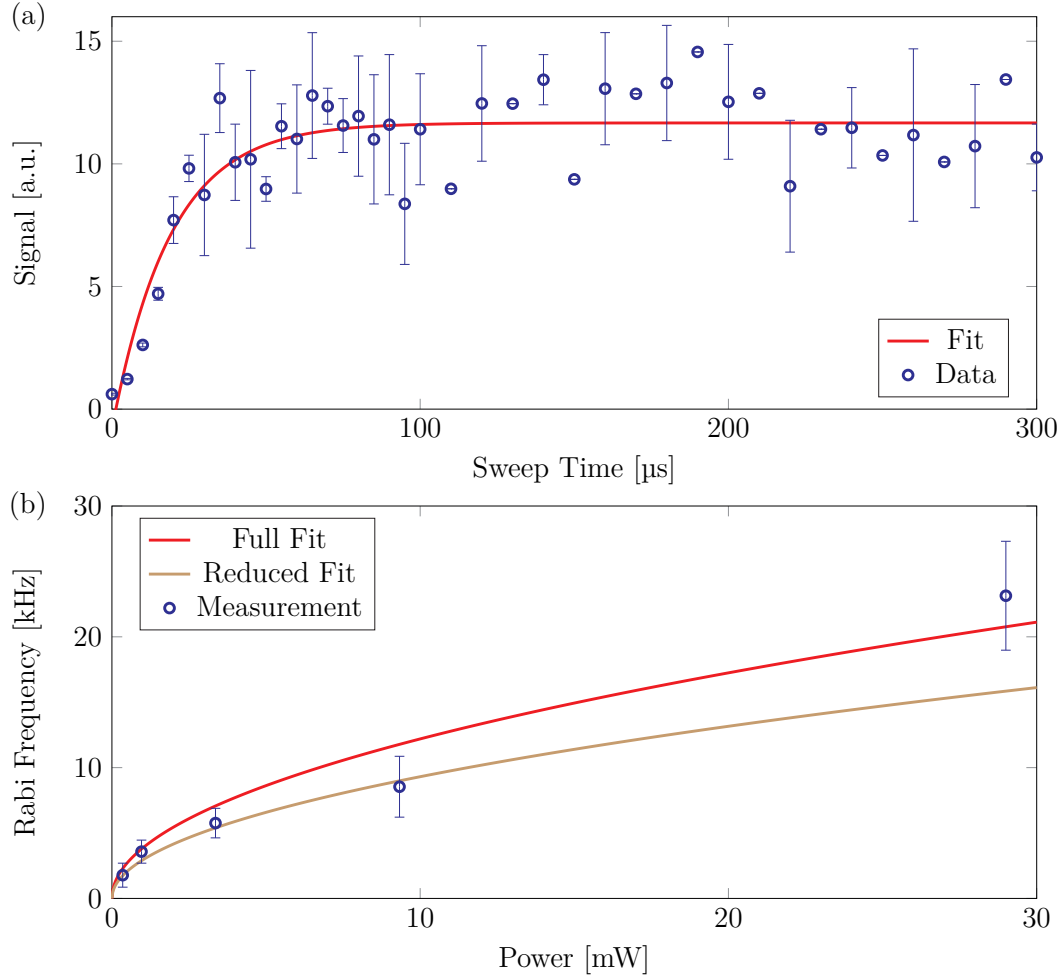


**Fig. 4.18:** Raman Rabi frequency measurement. (a) shows a fit of a Landau-Zener formula as shown in Eq. 4.18. The only free fit parameters are the amplitude, a constant offset and the Rabi frequency. The powers applied are 29 mW for R2 and R1H and the sweep range was 100 kHz. The obtained Rabi frequency is  $(23.1 \pm 4.2)$  kHz. As isolated data points were only taken once they do not have errorbars. (b) shows the obtained Rabi frequencies in dependence of the applied R1H power. R2 was constantly at 29 mW and the sweep range amounted 100 kHz. It can be seen that a square root function fits the obtained data well. In contrast to the "Full Fit" the "Reduced Fit" did not take the data point at 29 mW into account.

of the electric field amplitude. The only free parameter in the square root fit is the product of the beam waists of R2 and R1H as it is antiproportional to the electric field amplitude. The evaluated beam waist for the reduced fit is  $(1.14 \pm 0.09)$  mm, which is not much bigger than the specification for the used fiber collimators with 1 mm at the output side of the fibers.

This measurement was also used to determine the Rabi frequency of a sideband transition in Fig. 4.19. The single parameter that was changed in both measurements is the center frequency of the sweep to select the desired transition. The powers applied were 33 mW for R2 and 32 mW for R1H. The sweep range used was 50 kHz. For the carrier transition a Rabi frequency of  $(15.9 \pm 2.6)$  kHz was determined. The Rabi frequency for the HSB was measured to be  $(8.0 \pm 1.1)$  kHz. While the carrier

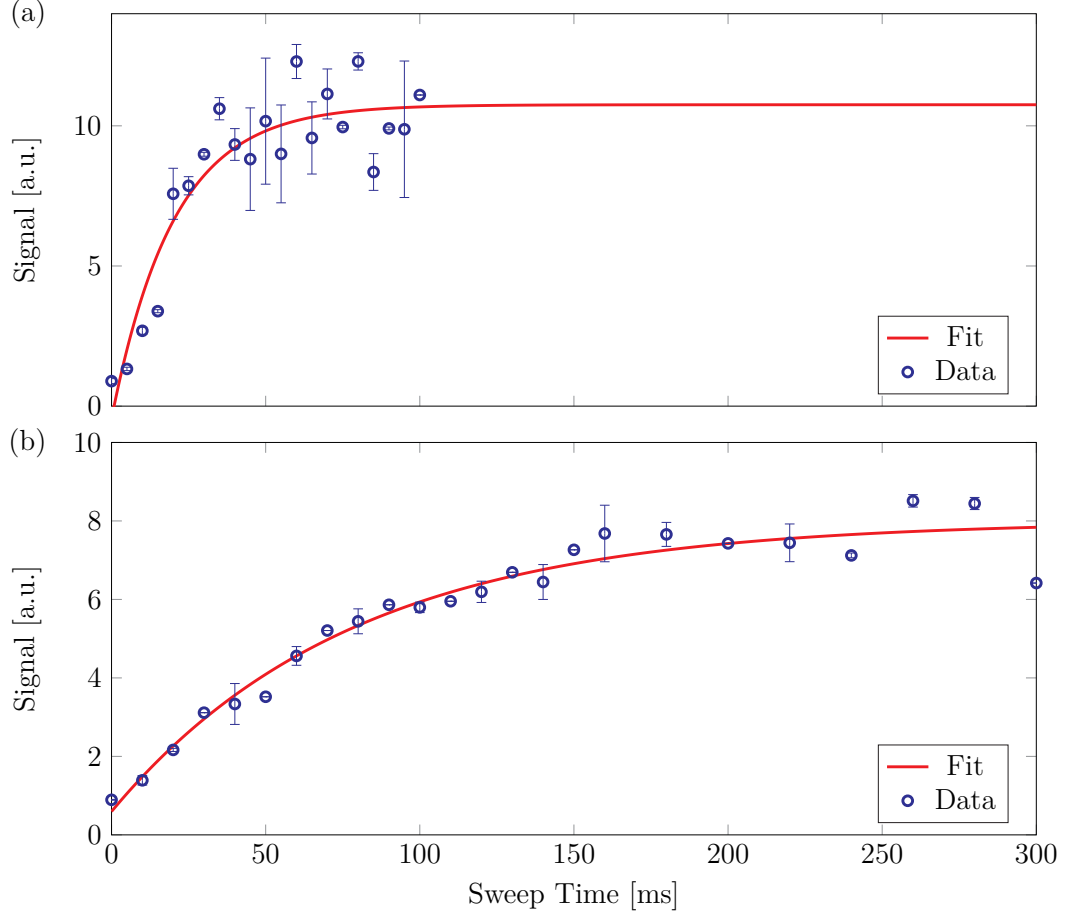


**Fig. 4.19:** Raman Rabi frequency measurement for a carrier and a sideband transition. (a) shows the data points for the carrier transition while in (b) the data points for the HSB can be seen. The carrier Rabi frequency is calculated to be  $(15.9 \pm 2.6)$  kHz and the sideband Rabi frequency is  $(8.0 \pm 1.1)$  kHz. With a ratio of  $1/2$  it is about 1.5 times as large as expected

Rabi Frequency matches the reduced fit from Fig. 4.18, the Rabi frequency for the HSB seems off. As the Rabi frequency for the HSB is given by  $\eta\sqrt{n+1}\Omega_C$  and the maximal Lamb-Dicke parameter is 0.23 this would correspond to a mean vibrational number of  $3.7 \pm 1.3$ . But this value is not in accordance with the calculated mean vibrational level of 1.11 from the spectrum in Fig. 4.16. For a mean vibrational level of 1.11 a Rabi frequency of 5.3 kHz would be expected.

#### 4.5.4 Raman Sideband Cooling Time Constant

In order to estimate a time constant for the Raman sideband cooling process three spectra with different cooling times were taken. The lack of time did not allow for further spectra but for a rough first estimation with an exponential fit this should be enough. This data cannot directly be compared to the ones in Fig. 4.16, as here the time frame reserved for Raman sideband cooling was constantly 200 ms. The value that changed for each datapoint, is the moment  $t_0$  when the shutters for the Raman sideband cooling were opened. The cooling time is thereby given by  $200 - t_0$ .

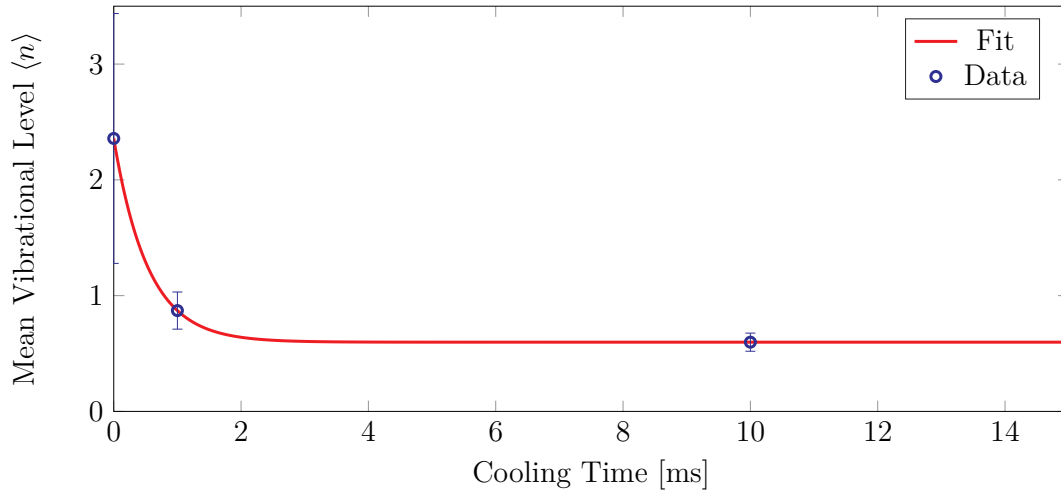


**Fig. 4.20:** Raman sideband cooling time constant measurement. The vibrational level was estimated in the same manner as described in 4.5.1. The cooling was preceded by a waiting time, such that together the waiting time and cooling time give 200 ms. Therefore, these values cannot be directly compared to the one determined in Fig. 4.16.

During the initial part of this time frame heating without any suppressing cooling occurs, as can be told by comparing the data points for 0 s cooling from Fig. 4.16 and Fig. 4.20. During the 200 ms time frame without cooling, the atoms gain 1.4 vibrational quanta. The fit in Fig. 4.20 has a time constant of 537  $\mu$ s.

## 4.6 Conclusion

A possible scheme for a continuous Raman sideband cooling application was presented which can be used as the basis for fluorescence imaging in a quantum gas microscope. Furthermore, with the Lindblad equation a method was introduced to calculate the density matrix evolution in systems governed by an Hamiltonian  $H$  and spontaneous processes. This method was used in combination with a numerical algorithm for solving differential equations in order to simulate the population evolution under the proposed cooling scheme. The evaluated decrease of the mean vibrational level is governed by a time constant of 266  $\mu$ s. Under the ideal conditions assumed for the simulation a illumination duration of 600 ms is sufficient for single site resolved imaging in the planned quantum gas microscope experiment. A upper limit for the loss of 3.3 % is obtained. However, the experimental parameters used for the simulations were not systematically optimized and thus may hold the potential for improvements.

In addition the constructed optical setups and the stable offset lock system were presented. By using the offset lock system the beat signal of the two Raman lasers only varied by 22.9 Hz over a time span of 10 hours and has a linewidth of only 1.5 Hz, though this may be seen as a upper limit as the minimum measurement



bandwidth was 1 Hz.

Due to thus far unresolved issues, currently the cooling experiments were only conducted in the 2D triangular lattice. In this lattice it was possible to successfully lower the mean vibrational level from  $1.11 \pm 0.08$  to  $0.28 \pm 0.02$ . By measuring the vibrational level for different cooling durations a time constant of 537 ms was determined. Moreover, by measuring the Rabi frequency indirectly by applying the Raman beams while sweeping once linearly over the resonance frequency the expected square root proportionality for the single Raman beam power was obtained. However, a discrepancy between the expected sideband transition Rabi frequency and the carrier transition Rabi frequency was found.



# Chapter 5

## Conclusion and Outlook

This thesis gives a brief introduction into optical transitions with atoms in order to understand the required mechanisms for the Raman-sideband cooling which are the optical transitions between magnetic hyperfine levels and Raman transitions.

Furthermore, the triangular lattice was discussed and the exact potential given by the three beam interference was presented. This was used to approximate the potential harmonically in order to establish a connection between the trap depth and the trap frequency. A trap frequency obtained by modulation spectroscopy was used in this relation to estimate the trap depth of  $2059E_R$ . Additionally, the Lamb-Dicke approximation was introduced for estimating the coupling between vibrational levels in a deep potential. By comparing the numerical calculated coupling of the triangular lattice, for which Wannier functions were used, to the Lamb-Dicke approximation and the explicit numerical calculation for the harmonic oscillator, it was found that the coupling in a deep triangular lattice only differs by 1.1 % from the harmonic oscillator. Therefore, they are almost equally well approximated by the Lamb-Dicke approximation.

Continuing with the development of a well suited fluorescence imaging scheme and brief introduction of the Lindblad equation for computing the time evolution of the density matrix in a system governed by a Hamiltonian  $\mathcal{H}$  and additional spontaneous processes, the imaging scheme was simulated for reasonable, but not optimized experimental parameters. From the simulation data the required imaging time of 600 ms was estimated in which an average of 1738 photons will be scattered per atom, while 3.3 % of the atoms will be lost from the trap. The mean vibrational level evolution can be described with a time constant of 266  $\mu$ s and the mean vibrational level decreases down to 0.04. Moreover, the experimental laser setup was presented, consisting of two offset-locked lasers. The offset-lock uses the interference beat signal between the two lasers as the input signal. Over a measurement time of 10 hours the maximum frequency change of the carrier peak amounted 22.9 Hz and the FWHM was 1.5 Hz, possibly limited by the measurement bandwidth of 1 Hz. The laser setup

could successfully be used to drive Rabi oscillations on the clock transition between the hyperfine ground states. The obtained frequency of  $(19.5 \pm 0.5)$  kHz matches the calculation of 19.4 kHz. With the initial beam alignment setup some difficulties were encountered during spectroscopy experiments which led to a preliminary alternative setup that only couples vibrational levels of the triangular lattice. Additionally, further experiments were continued only in the two dimensional triangular lattice to avoid disturbances. When the vertical lattice was applied, the spectra became broadened. Furthermore, if the vertical lattice was applied, the vertical lattice sidebands could even be resolved by microwave spectroscopy suggesting that the vertical lattice exhibits a local spin-dependency. In the two dimensional lattice, the triangular lattice sidebands were successfully resolved, and Raman-sideband cooling was applied. The vibrational level was lowered from  $1.11 \pm 0.08$  to  $0.28 \pm 0.02$ . A time constant characterizing the cooling of 537 ms was obtained which is in the same order as the numerical evaluated one. Even though decoherence, possibly caused by magnetic field fluctuations, prohibits the observation of Rabi oscillations, the Rabi frequency can indirectly be measured by driving the laser frequency linearly from red detuning over the resonance to blue detuning for different velocities. Such a time dependent system can be described by the Landau-Zener formula. Therefore, the Rabi frequency can be obtained by a fit. The Rabi frequencies for the carrier transition resemble the expected square root proportionality for the single Raman beam power. By comparing the sideband transition Rabi frequency to the carrier transition Rabi frequency a discrepancy was found as the Rabi frequency for the sideband transition was  $8/5$  of the expected value.

It was shown that in principle the built experimental setup can be used to drive Raman sideband transitions, and thereby is suitable for Raman sideband cooling. The achieved mean vibrational levels are not quite at the numerically estimated minimum being 7 time larger. Therefore, there might be still room for improvements only by systematically optimizing the experimental parameters, as this has not done yet. The Raman transition might also be improvable by reducing the detuning from the  $D_1$  transition or by decreasing the beam waists of the Raman beams in order to increase the Rabi frequency. Another issue is that the spectroscopy and cooling so far could only be done in the two dimensional triangular lattice. As mentioned, the occurred problems with the vertical lattice might be due to a local spin-dependency caused by misaligned polarization. Further investigations should clarify if this is the reason for the disturbed spectra. Moreover, currently there is no BEC as the number of atoms arriving at the far-off-resonance optical dipole trap does not allow for evaporative cooling into the degenerate state. As recently demonstrated, Raman cooling was used to achieve quantum degeneracy without the need for evaporative cooling [34]. A secondary application of the Raman setup for this purpose might

---

come into question.



# Appendix A

## An Atom in an Electromagnetic Field

For the sake of completeness this chapter will show a semi classical derivation of the Hamiltonian describing the interaction between an atom and an electromagnetic field beginning from the Lorentz force. The following will be a recapitulation of the corresponding chapters of [62–64].

### A.1 Classical Lorentz-Force Hamiltonian

Starting from the Lorentz force

$$\begin{aligned}\mathbf{F}_L &= q(\mathbf{E} + \mathbf{v} \times \mathbf{B}) \\ &= -q(\nabla\phi + \partial_t\mathbf{A} + (\mathbf{v} \cdot \nabla)\mathbf{A} - \nabla(\mathbf{v} \cdot \mathbf{A})),\end{aligned}\tag{A.1}$$

where  $q$  is the considered charge,  $\mathbf{v}$  the velocity of the charge and  $\mathbf{E}$  and  $\mathbf{B}$  the electric field and the magnetic flux density respectively, writing the E- and B-field in terms of the vector potential  $\mathbf{A}$  and the scalar field  $\phi$ , with

$$\mathbf{E} = -\nabla\phi - \partial_t\mathbf{A}\tag{A.2a}$$

$$\mathbf{B} = \nabla \times \mathbf{A},\tag{A.2b}$$

using the identity

$$\mathbf{v} \times (\nabla \times \mathbf{A}) = \nabla(\mathbf{v} \cdot \mathbf{A}) - (\mathbf{v} \cdot \nabla)\mathbf{A}\tag{A.3}$$

and utilizing the total time derivative of the vector potential

$$\frac{d}{dt}\mathbf{A} = \partial_t\mathbf{A} + \frac{\partial A}{\partial x_\alpha} \frac{\partial x_\alpha}{\partial t} = \partial_t\mathbf{A} + (\mathbf{v} \cdot \nabla)\mathbf{A},\tag{A.4}$$

the equation of motion

$$m\ddot{\mathbf{r}} = -q\frac{d}{dt}\mathbf{A} - q\nabla(\phi - \mathbf{v} \cdot \mathbf{A}) \quad (\text{A.5})$$

for a charged particle in an electromagnetic field can be derived. Written like

$$\frac{d}{dt}(m\dot{\mathbf{r}} + q\mathbf{A}) = -q\nabla(\phi - \dot{\mathbf{r}} \cdot \mathbf{A}) \quad (\text{A.6})$$

and compared to the Euler-Lagrange equation

$$\frac{d}{dt}\frac{\partial}{\partial\dot{\mathbf{r}}}L = \frac{\partial}{\partial\mathbf{r}}L, \quad (\text{A.7})$$

it can be seen that the generalized momentum equals

$$\mathbf{p} = \frac{\partial}{\partial\dot{\mathbf{r}}}L = m\dot{\mathbf{r}} + q\mathbf{A} \quad (\text{A.8})$$

and that the Lagrangian can be given by

$$L = \frac{1}{2}m\dot{\mathbf{r}}^2 + q\dot{\mathbf{r}}\mathbf{A} - q\phi. \quad (\text{A.9})$$

By using the Legendre transform, the Hamiltonian can be derived and results in

$$\begin{aligned} H &= \mathbf{p} \cdot \dot{\mathbf{r}} - L \\ &= \frac{\mathbf{p}}{m}(\mathbf{p} - q\mathbf{A}) - \frac{1}{2m}(\mathbf{p} - q\mathbf{A})^2 - \frac{q}{m}(\mathbf{p} - q\mathbf{A})\mathbf{A} + q\phi \\ &= \frac{(\mathbf{p} - q\mathbf{A})^2}{2m} + q\phi. \end{aligned} \quad (\text{A.10})$$

## A.2 The free Hydrogen Atom

By applying the canonical quantization to Eq. A.10, by

$$\mathbf{x} \rightarrow \hat{\mathbf{x}} \quad (\text{A.11a})$$

$$\mathbf{p} \rightarrow \hat{\mathbf{p}} = -i\hbar\nabla, \quad (\text{A.11b})$$

the semiclassical Lorentz force Hamiltonian is found to be

$$\begin{aligned} \mathcal{H} &= \frac{(\hat{\mathbf{p}} - q\mathbf{A}(\hat{\mathbf{x}}, t))^2}{2m} + q\phi(\hat{\mathbf{x}}, t) \\ &= \frac{(-i\hbar\nabla - q\mathbf{A}(\hat{\mathbf{x}}, t))^2}{2m} + q\phi(\hat{\mathbf{x}}, t). \end{aligned} \quad (\text{A.12})$$



For the simplified case of the Hydrogen atom, two oppositely charged point charges, in the Coulomb gauge,

$$\nabla \mathbf{A}(\hat{\mathbf{x}}, t) = 0, \quad (\text{A.13})$$

with no additional charges or currents and with coordinates relative to one of the charges, the scalar potential becomes

$$q\phi(\hat{\mathbf{x}}, t) = -q \frac{1}{4\pi\epsilon_0} \int \frac{\rho(\mathbf{x}', t)}{|\hat{\mathbf{x}} - \mathbf{x}'|} d^3x' = \frac{1}{4\pi\epsilon_0} \frac{qQ}{|\hat{\mathbf{x}}_e - \hat{\mathbf{x}}_p|} = -\frac{1}{4\pi\epsilon_0} \frac{e^2}{|\hat{\mathbf{x}}_e - \hat{\mathbf{x}}_p|}. \quad (\text{A.14})$$

In this case the Hamiltonian for the Hydrogen atom reads

$$\begin{aligned} \mathcal{H} &= \frac{(\hat{\mathbf{p}}_p - e\mathbf{A}(\hat{\mathbf{x}}_p, t))^2}{2m_p} + \frac{(\hat{\mathbf{p}}_e + e\mathbf{A}(\hat{\mathbf{x}}_e, t))^2}{2m_e} - \frac{1}{4\pi\epsilon_0} \frac{e^2}{|\hat{\mathbf{x}}_e - \hat{\mathbf{x}}_p|} \\ &= \frac{\hat{\mathbf{p}}_p^2}{2m_p} - \frac{e}{m_p} \hat{\mathbf{A}}_p \cdot \hat{\mathbf{p}}_p + \frac{e^2}{2m_p} \hat{\mathbf{A}}_p^2 \\ &\quad + \frac{\hat{\mathbf{p}}_e^2}{2m_e} + \frac{e}{m_e} \hat{\mathbf{A}}_e \cdot \hat{\mathbf{p}}_e + \frac{e^2}{2m_e} \hat{\mathbf{A}}_e^2 \\ &\quad - \frac{1}{4\pi\epsilon_0} \frac{e^2}{|\hat{\mathbf{x}}_e - \hat{\mathbf{x}}_p|}, \end{aligned} \quad (\text{A.15})$$

where the relation

$$\hat{\mathbf{p}} \cdot (\hat{\mathbf{A}} \cdot \psi) = -i\hbar \nabla (\hat{\mathbf{A}} \cdot \psi) = -i\hbar ((\nabla \hat{\mathbf{A}}) \cdot \psi + \hat{\mathbf{A}} \cdot \nabla \psi) = \hat{\mathbf{A}} \cdot \hat{\mathbf{p}} \cdot \psi, \quad (\text{A.16})$$

due to the Coulomb gauge in Eq. A.13, was used.

## A.3 Center-of-Mass System

The center of mass is given by

$$\hat{\mathbf{R}} \stackrel{\text{def}}{=} \frac{m_p}{M} \hat{\mathbf{x}}_p + \frac{m_e}{M} \hat{\mathbf{x}}_e, \text{ with} \quad (\text{A.17a})$$

$$M \stackrel{\text{def}}{=} m_p + m_e, \quad (\text{A.17b})$$

and the relative coordinate between electron and proton by

$$\hat{\mathbf{r}} \stackrel{\text{def}}{=} \hat{\mathbf{x}}_e - \hat{\mathbf{x}}_p. \quad (\text{A.18})$$

Since the proton is about 1836 times heavier than the electron, their positions can be approximated by

$$\hat{\mathbf{x}}_p = \hat{\mathbf{R}} - \frac{m_e}{M} \hat{\mathbf{r}} \approx \hat{\mathbf{R}} - \frac{m_e}{m_p} \hat{\mathbf{r}} \quad \text{and} \quad (\text{A.19a})$$

$$\hat{\mathbf{x}}_e = \hat{\mathbf{R}} + \frac{m_p}{M} \hat{\mathbf{r}} \approx \hat{\mathbf{R}} + \left(1 - \frac{m_e}{m_p}\right) \hat{\mathbf{r}}. \quad (\text{A.19b})$$

Furthermore, the relations

$$\hat{\mathbf{P}} \stackrel{\text{def}}{=} \hat{\mathbf{p}}_p + \hat{\mathbf{p}}_e, \quad (\text{A.20a})$$

$$\hat{\mathbf{p}} \stackrel{\text{def}}{=} \frac{m_e}{M} \hat{\mathbf{p}}_p - \frac{m_p}{M} \hat{\mathbf{p}}_e \quad \text{and} \quad (\text{A.20b})$$

$$\mu \stackrel{\text{def}}{=} \frac{m_p m_e}{m_p + m_e}, \quad (\text{A.20c})$$

describing the momentum of the center of mass, the relative momentum of the reduced mass and the reduced mass respectively, are used to rewrite the proton and electron momenta as

$$\hat{\mathbf{p}}_p = \frac{m_p}{M} \hat{\mathbf{P}} + \hat{\mathbf{p}} \quad \text{and} \quad (\text{A.21a})$$

$$\hat{\mathbf{p}}_e = \frac{m_e}{M} \hat{\mathbf{P}} - \hat{\mathbf{p}}. \quad (\text{A.21b})$$

Using the center of mass and relative coordinates, momenta and masses, the Hamiltonian Eq. A.15 becomes

$$\begin{aligned} \mathcal{H} = & \frac{\hat{\mathbf{P}}^2}{2M} + \frac{\hat{\mathbf{p}}^2}{2\mu} - \frac{1}{4\pi\epsilon_0} \frac{e^2}{|\hat{\mathbf{r}}|} \\ & - \frac{e}{M} \left( \hat{\mathbf{A}}_p - \hat{\mathbf{A}}_e \right) \hat{\mathbf{P}} \\ & - \frac{e}{\mu} \left( \frac{\mu}{m_p} \hat{\mathbf{A}}_p + \frac{\mu}{m_e} \hat{\mathbf{A}}_e \right) \hat{\mathbf{p}} \\ & + \frac{e^2}{2m_p} \hat{\mathbf{A}}_p^2 + \frac{e^2}{2m_e} \hat{\mathbf{A}}_e^2. \end{aligned} \quad (\text{A.22})$$

## A.4 Dipole Approximation

Within the Coulomb gauge, the vector potential  $\hat{\mathbf{A}}$  is connected to the electric field of the present electromagnetic field by

$$\frac{\partial}{\partial t} \hat{\mathbf{A}} = -\hat{\mathbf{E}}_{EM} \quad (\text{A.23})$$

and therefore has the same wavelength  $\lambda$  as such. If this wavelength is large compared to the size of the atom,

$$\frac{d_A}{\lambda} \ll 1, \quad (\text{A.24})$$

with  $d_A$  the atom diameter, the vector potential can be approximated to be constant over the extend of the atom. Considering the van der Waals radius of Caesium in [65] and the lower end of the visible spectrum, the ratio becomes

$$\frac{d_A}{\lambda} = \frac{6.86 \text{ \AA}}{3800 \text{ \AA}} \approx 0.002 \ll 1$$

and therefore justifying what is called the dipole approximation for at least all stable atomic species for the visible spectrum. By applying the dipole approximation on Eq. A.22 the Hamiltonian simplifies to

$$\begin{aligned} \mathcal{H} &= \frac{\hat{\mathbf{P}}^2}{2M} + \frac{\hat{\mathbf{p}}^2}{2\mu} - \frac{e}{\mu} \hat{\mathbf{A}}_0 \hat{\mathbf{p}} + \frac{e^2}{2\mu} \hat{\mathbf{A}}_0^2 - \frac{1}{4\pi\epsilon_0} \frac{e^2}{|\hat{\mathbf{r}}|} \\ &= \frac{\hat{\mathbf{P}}^2}{2M} + \frac{1}{2\mu} \left( \hat{\mathbf{p}} - e \hat{\mathbf{A}}_0 \right)^2 - \frac{1}{4\pi\epsilon_0} \frac{e^2}{|\hat{\mathbf{r}}|}. \end{aligned} \quad (\text{A.25})$$

Since the first term in Eq. A.25 is only depends on the center of mass motion, it can be disregarded concerning the internal state of the atom. The Hamiltonian describing the electronic structure of the hydrogen atom is then

$$\begin{aligned} \mathcal{H} &= \frac{\hat{\mathbf{p}}^2}{2\mu} - \frac{e}{\mu} \hat{\mathbf{A}}_0 \hat{\mathbf{p}} + \frac{e^2}{2\mu} \hat{\mathbf{A}}_0^2 - \frac{1}{4\pi\epsilon_0} \frac{e^2}{|\hat{\mathbf{r}}|} \\ &= \frac{1}{2\mu} \left( \hat{\mathbf{p}} - e \hat{\mathbf{A}}_0 \right)^2 - \frac{1}{4\pi\epsilon_0} \frac{e^2}{|\hat{\mathbf{r}}|}. \end{aligned} \quad (\text{A.26})$$

## A.5 Local Transformation

For a unitary local transformation of the form

$$\psi(\mathbf{r}, t) \rightarrow \hat{T}(\hat{\mathbf{r}}, t) \psi(\mathbf{r}, t) \quad (\text{A.27})$$

$$\tilde{\mathcal{H}} \rightarrow \hat{T} \mathcal{H} \hat{T}^\dagger, \text{ with} \quad (\text{A.28})$$

$$\hat{T}(\hat{\mathbf{x}}, t) = e^{-\frac{i}{\hbar} e \hat{\mathbf{r}} \hat{\mathbf{A}}_0}, \quad (\text{A.29})$$

the Hamiltonian becomes

$$\begin{aligned} \mathcal{H} &= \frac{\hat{\mathbf{p}}^2}{2\mu} - \frac{1}{4\pi\epsilon_0} \frac{e^2}{|\hat{\mathbf{r}}|} + e \hat{\mathbf{r}} \frac{\partial}{\partial t} \hat{\mathbf{A}}_0 \\ &= \frac{\hat{\mathbf{p}}^2}{2\mu} - \frac{1}{4\pi\epsilon_0} \frac{e^2}{|\hat{\mathbf{r}}|} - e \hat{\mathbf{r}} \hat{\mathbf{E}}_{EM}. \end{aligned} \quad (\text{A.30})$$

For Eq. A.30

$$e^{\hat{A}} \hat{B} e^{-\hat{A}} = \hat{B} + [\hat{A}, \hat{B}] + \frac{1}{2!} [\hat{A}, [\hat{A}, \hat{B}]] + \dots, \quad (\text{A.31})$$

Eq. A.16 and Eq. A.23 were used, the first two giving

$$\hat{T} \hat{\mathbf{p}} \hat{T}^\dagger = \hat{\mathbf{p}} + \left[ -\frac{i}{\hbar} e \hat{\mathbf{r}} \hat{\mathbf{A}}_0, \hat{\mathbf{p}} \right] = \hat{\mathbf{p}} + \left[ -\frac{i}{\hbar} e \hat{\mathbf{r}} \hat{\mathbf{A}}_0, \frac{\hbar}{i} \nabla \right] = \hat{\mathbf{p}} + e \hat{\mathbf{A}}, \quad (\text{A.32})$$

and

$$\begin{aligned} \hat{T} \hat{\mathbf{p}}^2 \hat{T}^\dagger &= \hat{\mathbf{p}}^2 + \left[ -\frac{i}{\hbar} e \hat{\mathbf{r}} \hat{\mathbf{A}}_0, \hat{\mathbf{p}}^2 \right] + \frac{1}{2} \left[ -\frac{i}{\hbar} e \hat{\mathbf{r}} \hat{\mathbf{A}}_0, \left[ -\frac{i}{\hbar} e \hat{\mathbf{r}} \hat{\mathbf{A}}_0, \hat{\mathbf{p}}^2 \right] \right] \\ &= \hat{\mathbf{p}}^2 + \left[ -\frac{i}{\hbar} e \hat{\mathbf{r}} \hat{\mathbf{A}}_0, \hat{\mathbf{p}} \right] \hat{\mathbf{p}} + \hat{\mathbf{p}} \left[ -\frac{i}{\hbar} e \hat{\mathbf{r}} \hat{\mathbf{A}}_0, \hat{\mathbf{p}} \right] \\ &\quad + \frac{1}{2} \left[ -\frac{i}{\hbar} e \hat{\mathbf{r}} \hat{\mathbf{A}}_0, \left[ -\frac{i}{\hbar} e \hat{\mathbf{r}} \hat{\mathbf{A}}_0, \hat{\mathbf{p}} \right] \hat{\mathbf{p}} + \hat{\mathbf{p}} \left[ -\frac{i}{\hbar} e \hat{\mathbf{r}} \hat{\mathbf{A}}_0, \hat{\mathbf{p}} \right] \right] \\ &= \hat{\mathbf{p}}^2 + 2e \hat{\mathbf{A}}_0 \hat{\mathbf{p}} + \frac{1}{2} \left[ -\frac{i}{\hbar} e \hat{\mathbf{r}} \hat{\mathbf{A}}_0, 2e \hat{\mathbf{A}}_0 \hat{\mathbf{p}} \right] \\ &= \hat{\mathbf{p}}^2 + 2e \hat{\mathbf{A}}_0 \hat{\mathbf{p}} + e^2 \hat{\mathbf{A}}_0^2. \end{aligned} \quad (\text{A.33})$$

The term with the partial time derivative in Eq. A.30 is necessary to satisfy the Schrödinger equation, since

$$i\hbar \hat{T} \frac{\partial}{\partial t} \hat{T}^\dagger = i\hbar \frac{\partial}{\partial t} - e \hat{\mathbf{r}} \frac{\partial}{\partial t} \hat{\mathbf{A}}_0. \quad (\text{A.34})$$

Now the Hamiltonian can be written as

$$\mathcal{H} = \mathcal{H}_0 + \mathcal{H}', \text{ with} \quad (\text{A.35a})$$

$$\mathcal{H}_0 = \frac{\hat{\mathbf{p}}^2}{2\mu} - \frac{1}{4\pi\epsilon_0} \frac{e^2}{|\hat{\mathbf{r}}|} \quad \text{and} \quad (\text{A.35b})$$

$$\mathcal{H}' = -e \hat{\mathbf{r}} \hat{\mathbf{E}}_{EM}(t). \quad (\text{A.35c})$$

$\mathcal{H}_0$  describes the interaction between the electron and the nucleus, having the well known hydrogen electron orbitals as solutions.  $\mathcal{H}'$  describes the coupling between the Hydrogen atom and the electromagnetic field.

# Appendix B

## $^{87}\text{Rb}$ Hyperfine Energy Scheme

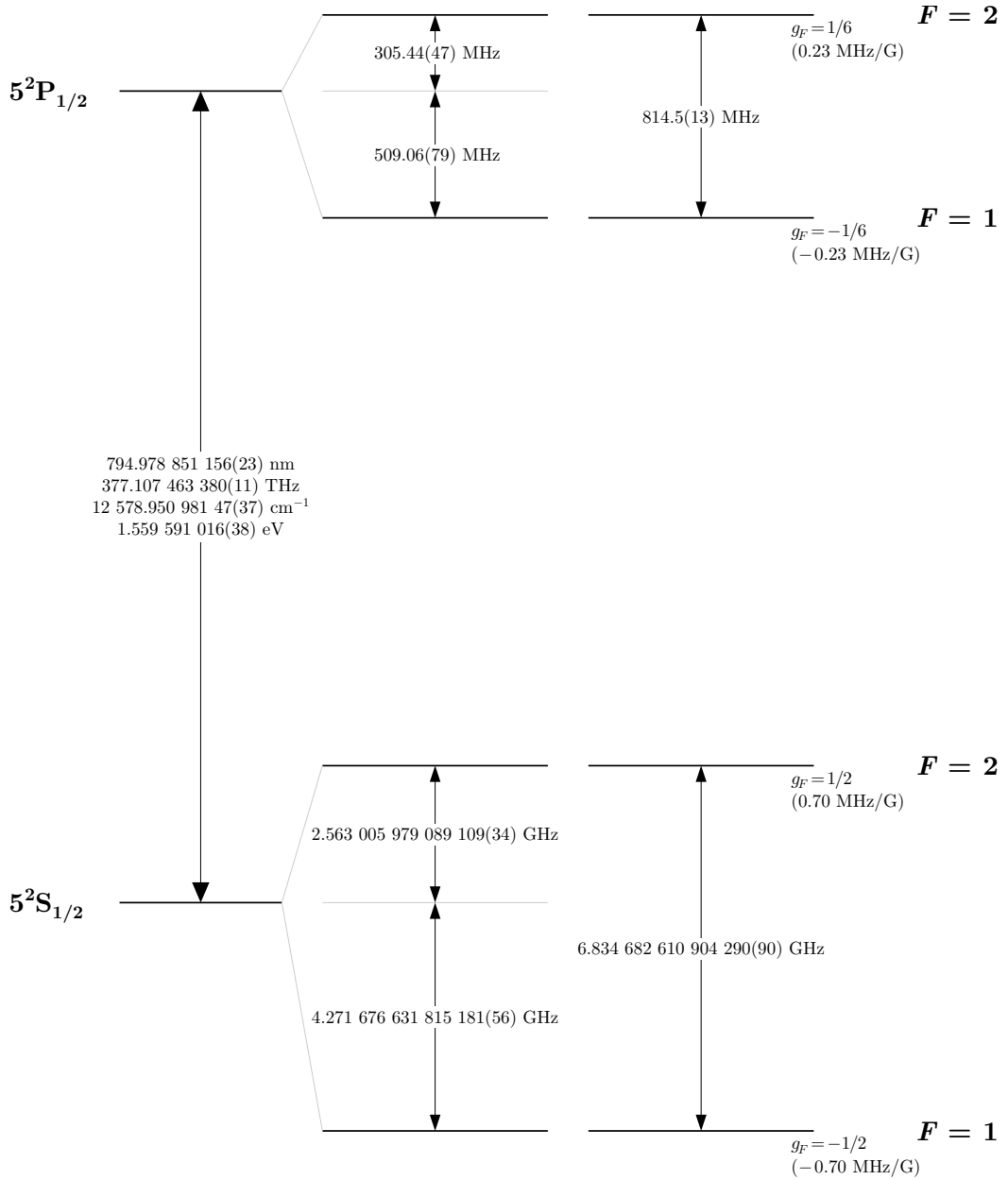


**Fig. B.1:** Hyperfine Energy Scheme of  $^{87}\text{Rb}$  for the  $D_1$  transition. From [40].

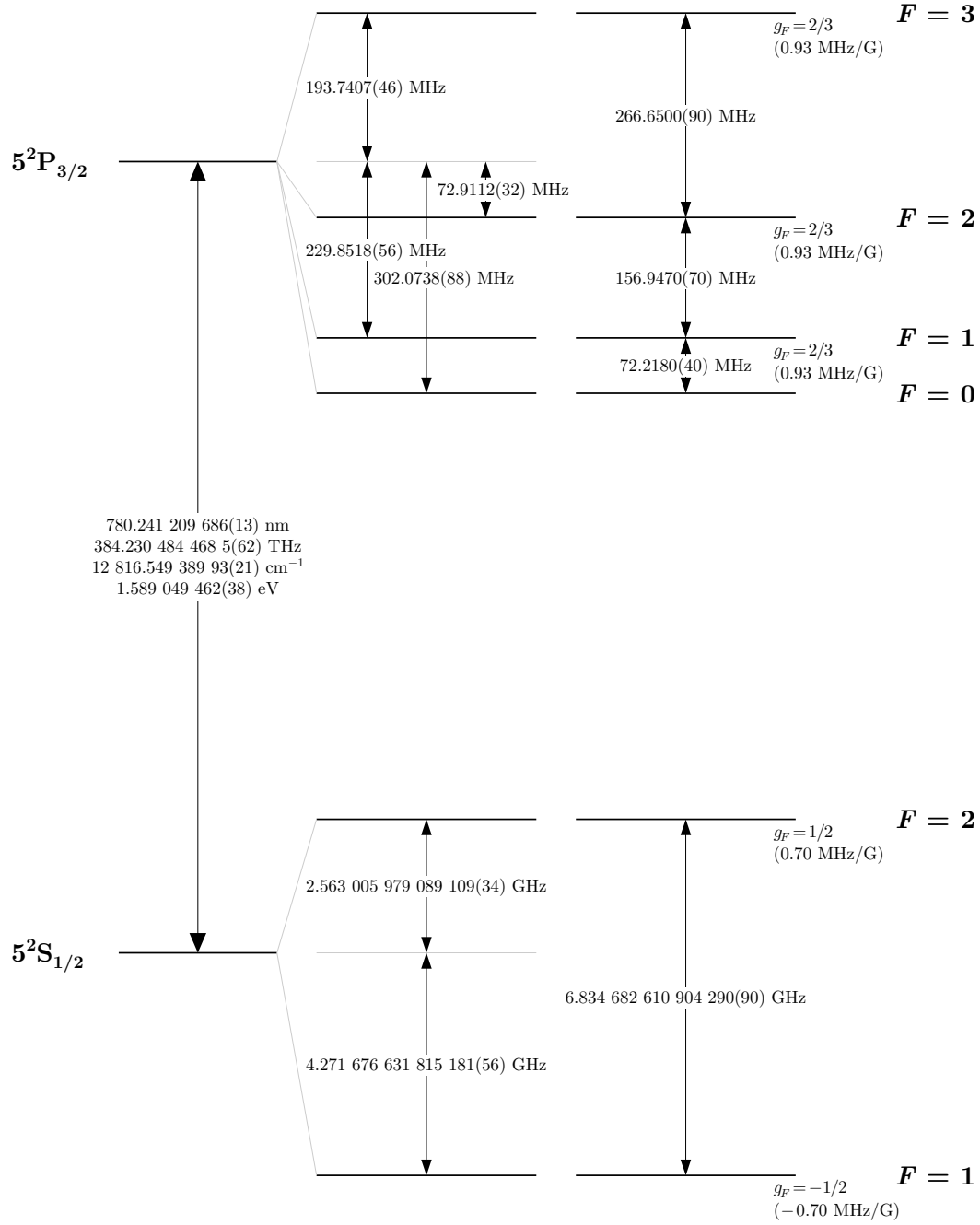


**Fig. B.2:** Hyperfine Energy Scheme of  $^{87}\text{Rb}$  for the  $D_2$  transition. From [40].

# Acknowledgments

My gratitude and appreciation goes to the people who helped me bring this thesis into reality. I would like to thank my first thesis advisor Prof. Klaus Sengstock who kindly supported me. Especially I am thankful for him being so willing to take on this burden of being my advisor and his effort to make this thesis possible.

I am grateful to my second thesis advisor Dr. Takeshi Fukuhara at the RIKEN Center for Emergent Matter Science in Wako, Japan for giving me the opportunity to conduct my research in his lab. I value his expertise, constant guidance and constructive critiquing that steered me in the right direction and that enabled me to write this thesis. I also would like to thank the other members of the Quantum Many-Body-Dynamics Research Unit.

To Dr. Ryuta Yamamoto who worked very determined and was always willing to explain anything I bugged him with and seemed to have an answer to almost any of my questions.

To Dr. Hideki Ozawa who I spent some time with in the cold lab and was always very patient when we misaligned any optical parts by accident during adjustments and was always willing to help me with the many experimental setups.

To Dr. Ippei Nakamura who is not part of the group anymore, but shared lot of his expertise regarding electronics and the offset-lock system.

To Dr. Jie Wang who I did not work with, but from whom I could learn a little bit about Rydberg atoms.

For all their endless patience, motivation, enthusiasm and ample time spent that led to the accomplishment of this research.

I also want to thank Dr. Yago del Valle Inclan Redondo from the Quantum Functional System Research Group for occasional help with questions I had regarding Wannier states.

Furthermore, I would like to thank my family for their support and for the chance to fulfill my dream.

Thank you.

ありがとうございました。





# Bibliography

- [1] Richard P. Feynman. Simulating physics with computers. *Int. J. Theor. Phys.*, 21(6):467–488, 1982.
- [2] Satyendra Nath Bose. Plancks gesetz und lichtquantenhypothese. *Z. Phys.*, 26(1):178–181, 1924.
- [3] Albert Einstein. Quantentheorie des idealen einatomigen gases ii. *Sitzber. Kgl. Preuss. Akad. Wiss., Phys. Math. Kl. Bericht*, 3:18, 1925.
- [4] EL Raab, M Prentiss, Alex Cable, Steven Chu, and David E Pritchard. Trapping of neutral sodium atoms with radiation pressure. *Physical Review Letters*, 59(23):2631, 1987.
- [5] Paul D Lett, Richard N Watts, Christoph I Westbrook, William D Phillips, Phillip L Gould, and Harold J Metcalf. Observation of atoms laser cooled below the doppler limit. *Physical review letters*, 61(2):169, 1988.
- [6] Jean Dalibard and Claude Cohen-Tannoudji. Laser cooling below the doppler limit by polarization gradients: simple theoretical models. *JOSA B*, 6(11):2023–2045, 1989.
- [7] Harald F Hess. Evaporative cooling of magnetically trapped and compressed spin-polarized hydrogen. *Physical Review B*, 34(5):3476, 1986.
- [8] Naoto Masuhara, John M Doyle, Jon C Sandberg, Daniel Kleppner, Thomas J Greytak, Harald F Hess, and Greg P Kochanski. Evaporative cooling of spin-polarized atomic hydrogen. *Physical Review Letters*, 61(8):935, 1988.
- [9] Mike H. Anderson, Jason R. Ensher, Michael R. Matthews, Carl E. Wieman, and Eric A. Cornell. Observation of bose-einstein condensation in a dilute atomic vapor. *Science*, 269(5221):198–201, 1995.
- [10] Kendall B. Davis, M.-O. Mewes, Michael R. Andrews, Nicolaas J. van Druten, Dallin S. Durfee, D. M. Kurn, and Wolfgang Ketterle. Bose-einstein condensation in a gas of sodium atoms. *Phys. Rev. Lett.*, 75(22):3969, 1995.

- [11] D. S. Jin, J. R. Ensher, M. R. Matthews, C. E. Wieman, and Eric A. Cornell. Collective excitations of a bose-einstein condensate in a dilute gas. *Phys. Rev. Lett.*, 77(3):420, 1996.
- [12] M.-O. Mewes, M. R. Andrews, N. J. Van Druten, D. M. Kurn, D. S. Durfee, C. G. Townsend, and W. Ketterle. Collective excitations of a bose-einstein condensate in a magnetic trap. *Phys. Rev. Lett.*, 77(6):988, 1996.
- [13] M. R. Andrews, C. G. Townsend, H.-J. Miesner, D. S. Durfee, D. M. Kurn, and W. Ketterle. Observation of interference between two bose condensates. *Science*, 275(5300):637–641, 1997.
- [14] Michael Robin Matthews, Brian P. Anderson, P. C. Haljan, D. S. Hall, C. E. Wieman, and Eric A. Cornell. Vortices in a bose-einstein condensate. *Phys. Rev. Lett.*, 83(13):2498, 1999.
- [15] Stefan Burger, Kai Bongs, Stefanie Dettmer, Wolfgang Ertmer, Klaus Sengstock, Anna Sanpera, Gora V. Shlyapnikov, and Maciej Lewenstein. Dark solitons in bose-einstein condensates. *Phys. Rev. Lett.*, 83(25):5198, 1999.
- [16] Dieter Jaksch, Christoph Bruder, Juan Ignacio Cirac, Crispin W Gardiner, and Peter Zoller. Cold bosonic atoms in optical lattices. *Physical Review Letters*, 81(15):3108, 1998.
- [17] Immanuel Bloch, Jean Dalibard, and Wilhelm Zwerger. Many-body physics with ultracold gases. *Rev. Mod. Phys.*, 80(3):885, 2008.
- [18] Immanuel Bloch, Jean Dalibard, and Sylvain Nascimbène. Quantum simulations with ultracold quantum gases. *Nature Physics*, 8(4):267–276, apr 2012.
- [19] Markus Greiner, Olaf Mandel, Tilman Esslinger, Theodor W Hänsch, and Immanuel Bloch. Quantum phase transition from a superfluid to a mott insulator in a gas of ultracold atoms. *Nature*, 415(6867):39, 2002.
- [20] Brian DeMarco and Deborah S Jin. Onset of fermi degeneracy in a trapped atomic gas. *science*, 285(5434):1703–1706, 1999.
- [21] Michael Köhl, Henning Moritz, Thilo Stöferle, Kenneth Günter, and Tilman Esslinger. Fermionic atoms in a three dimensional optical lattice: Observing fermi surfaces, dynamics, and interactions. *Physical Review Letters*, 94(8), mar 2005.
- [22] Robert Jördens, Niels Strohmaier, Kenneth Günter, Henning Moritz, and Tilman Esslinger. A mott insulator of fermionic atoms in an optical lattice. *Nature*, 455(7210):204–207, sep 2008.

- 
- [23] Julian Struck, Christoph Ölschläger, R Le Targat, Parvis Soltan-Panahi, André Eckardt, Maciej Lewenstein, Patrick Windpassinger, and Klaus Sengstock. Quantum simulation of frustrated classical magnetism in triangular optical lattices. *Science*, 333(6045):996–999, 2011.
- [24] C Becker, P Soltan-Panahi, J Kronjäger, S Dörscher, K Bongs, and K Sengstock. Ultracold quantum gases in triangular optical lattices. *New J. Phys.*, 12(6):065025, 2010.
- [25] Lucile Savary and Leon Balents. Quantum spin liquids: a review. *Reports on Progress in Physics*, 80(1):016502, 2016.
- [26] Waseem S. Bakr, Jonathon I. Gillen, Amy Peng, Simon Fölling, and Markus Greiner. A quantum gas microscope for detecting single atoms in a hubbard-regime optical lattice. *Nature*, 462(7269):74–77, nov 2009.
- [27] Jacob F. Sherson, Christof Weitenberg, Manuel Endres, Marc Cheneau, Immanuel Bloch, and Stefan Kuhr. Single-atom-resolved fluorescence imaging of an atomic mott insulator. *Nature*, 467(7311):68–72, aug 2010.
- [28] Elmar Haller, James Hudson, Andrew Kelly, Dylan A. Cotta, Bruno Peaudecerf, Graham D. Bruce, and Stefan Kuhr. Single-atom imaging of fermions in a quantum-gas microscope. *Nature Physics*, 11(9):738–742, jul 2015.
- [29] G. J. A. Edge, R. Anderson, D. Jervis, D. C. McKay, R. Day, S. Trotzky, and J. H. Thywissen. Imaging and addressing of individual fermionic atoms in an optical lattice. *Physical Review A*, 92(6), dec 2015.
- [30] Ryuta Yamamoto, Jun Kobayashi, Takuma Kuno, Kohei Kato, and Yoshiro Takahashi. An ytterbium quantum gas microscope with narrow-line laser cooling. *New Journal of Physics*, 18(2):023016, 2016.
- [31] Y. S. Patil, S. Chakram, L. M. Aycok, and M. Vengalattore. Nondestructive imaging of an ultracold lattice gas. *Phys. Rev. A*, 90(3), sep 2014.
- [32] Lawrence W. Cheuk, Matthew A. Nichols, Melih Okan, Thomas Gersdorf, Vinay V. Ramasesh, Waseem S. Bakr, Thomas Lompe, and Martin W. Zwierlein. Quantum-gas microscope for fermionic atoms. *Phys. Rev. Lett.*, 114(19), may 2015.
- [33] Jiazhong Hu, Alban Urvoy, Zachary Vendeiro, Valentin Crépel, Wenlan Chen, and Vladan Vuletić. Creation of a bose-condensed gas of rubidium 87 by laser cooling. *arXiv preprint arXiv:1705.03421*, 2017.

- [34] Alban Urvoy, Zachary Vendeiro, Joshua Ramette, Albert Adiyatullin, and Vladan Vuletić. Direct laser cooling to bose-einstein condensation in a dipole trap. *Physical review letters*, 122(20):203202, 2019.
- [35] Harold J. Metcalf and Peter van der Straten. *Laser Cooling and Trapping*. Springer, 1999.
- [36] Peter van der Straten and Harold J. Metcalf. *Atoms and Molecules Interacting with Light*. Cambridge University Press, 2016.
- [37] Christopher J. Foot. *Atomic physics*. Oxford University Press, 2005.
- [38] Jun John Sakurai and Jim Napolitano. *Modern Quantum Mechanics*. Addison-Wesley, second edition, 2011.
- [39] Franz Schwabl. *Quantenmechanik*. Springer, 2007.
- [40] Daniel Adam Steck. Rubidium 87 d line data, January 2015. revision 2.1.5.
- [41] Alexander J. Dunning. *Coherent Atomic Manipulation and Cooling*. PhD thesis, University of Southampton, 2015.
- [42] K-J Boller, A Imamoglu, and Stephen E Harris. Observation of electromagnetically induced transparency. *Physical Review Letters*, 66(20):2593, 1991.
- [43] P Marte, P Zoller, and John L Hall. Coherent atomic mirrors and beam splitters by adiabatic passage in multilevel systems. *Physical Review A*, 44(7):R4118, 1991.
- [44] James Bateman, André Xuereb, and Tim Freegarde. Stimulated raman transitions via multiple atomic levels. *Phys. Rev. A*, 81(4), apr 2010.
- [45] Rudolf Grimm, Matthias Weidemüller, and Yurii B Ovchinnikov. Optical dipole traps for neutral atoms. In *Advances in atomic, molecular, and optical physics*, volume 42, pages 95–170. Elsevier, 2000.
- [46] Rudolf Gross and Achim Marx. *Festkörperphysik*. Walter de Gruyter GmbH & Co KG, 2018.
- [47] C Kittel. Einführung in die festkörperphysik, vol. 14. *Oldenburg Wissenschaftsverlag*, pages 568–577, 2006.
- [48] Christoph Becker. *Multi component Bose-Einstein condensates - From mean field physics to strong correlations*. PhD thesis, Universität Hamburg, 2009.
- [49] Walter Kohn. Analytic properties of bloch waves and wannier functions. *Physical Review*, 115(4):809, 1959.

- 
- [50] Nicola Marzari and David Vanderbilt. Maximally localized generalized wannier functions for composite energy bands. *Phys. Rev. B*, 56(20):12847, 1997.
- [51] Nicola Marzari, Ivo Souza, and David Vanderbilt. An introduction to maximally-localized wannier functions. *Psi-K newsletter*, 57:129, 2003.
- [52] Nicola Marzari, Arash A Mostofi, Jonathan R Yates, Ivo Souza, and David Vanderbilt. Maximally localized wannier functions: Theory and applications. *Rev. Mod. Phys.*, 84(4):1419, 2012.
- [53] Arash A Mostofi, Jonathan R Yates, Young-Su Lee, Ivo Souza, David Vanderbilt, and Nicola Marzari. wannier90: A tool for obtaining maximally-localised wannier functions. *Comput. Phys. Commun.*, 178(9):685–699, 2008.
- [54] R Walters, G Cotugno, TH Johnson, SR Clark, and D Jaksch. Ab initio derivation of hubbard models for cold atoms in optical lattices. *Phys. Rev. A*, 87(4):043613, 2013.
- [55] David J Wineland and Wayne M Itano. Laser cooling of atoms. *Physical Review A*, 20(4):1521, 1979.
- [56] David J Wineland, C Monroe, Wayne M Itano, Dietrich Leibfried, Brian E King, and Dawn M Meekhof. Experimental issues in coherent quantum-state manipulation of trapped atomic ions. *J. Res. Nat. Inst. Stand. Technol.*, 103(3):259, 1998.
- [57] Lawrence F. Shampine and Mark W. Reichelt. The matlab ode suite. *SIAM J. Sci. Comput.*, 18(1):1–22, 1997.
- [58] Fabian Friederich, Gunter Schuricht, Anselm Deninger, Frank Lison, Gunnar Spickermann, Peter Haring Bolívar, and Hartmut G Roskos. Phase-locking of the beat signal of two distributed-feedback diode lasers to oscillators working in the mhz to thz range. *Opt. Express*, 18(8):8621–8629, 2010.
- [59] Andrew James Kerman. *Raman sideband cooling and cold atomic collisions in optical lattices*. PhD thesis, Stanford University, 2002.
- [60] Noomen Belmechri, Leonid Förster, Wolfgang Alt, Artur Widera, Dieter Meschede, and Andrea Alberti. Microwave control of atomic motional states in a spin-dependent optical lattice. *Journal of Physics B: Atomic, Molecular and Optical Physics*, 46(10):104006, may 2013.
- [61] Amar C Vutha. A simple approach to the landau–zener formula. *European Journal of Physics*, 31(2):389, 2010.

- [62] Wolfgang P. Schleich. *Quantum Optics in Phase Space*. Wiley-VCH, 2001.
- [63] Daniel Adam Steck. Quantum and atom optics. Lecture, January 2019. revision 0.12.5.
- [64] Eric Akkermans. Atom-photon interactions. Lecture, 2017.
- [65] Manjeera Mantina, Adam C. Chamberlin, Rosendo Valero, Christopher J. Cramer, and Donald G. Truhlar. Consistent van der waals radii for the whole main group. *J. Phys. Chem. A*, 113(19):5806–5812, 2009.